Development of a thermal model for SPS modified for the production of bioimplants

Politecnico di Torino
Corso di Dottorato in Metrologia: Scienza e Tecnica delle Misure
XXVIII ciclo

Development of a thermal model for SPS modified for the production of bioimplants

Daniele Fulginiti

tutore: prof. Sabrina Grassini
co-tutore: prof. Marco Parvis

Index

1. Introduction

1.1. Bioabsorbable magnesium implants

Bioabsorbable materials can be used to produce bioimplants designed to remain in the host body only for the required time and then to get gradually dissolved in the body fluids without harmful effects. Although polymeric implants, made in poly-lactic and poly-glycolic acid, are already in use, they have a quite poor mechanical performance and can be used only when the load is expected to be very small. [Hofmann, 1995]

Magnesium is a promising alternative to polymeric bioabsorbable materials because it has much better mechanical properties and it is an essential element for the human metabolism. It can get dissolved into the blood flow without any poisoning effect. However the corrosion of magnesium must be slow enough to avoid the accumulation of hydrogen in the body, that may cause necrosis and a fatal blockage of blood flow. [Witte, 2015]

Recently, producing effective magnesium bioimplants became possible since high purity magnesium alloys are available that contain only elements which are biocompatible and not detrimental to the corrosion resistance. [Song, 2007]

Magnesium is suitable for producing bioabsorbable orthopaedic implants because it has a low specific weight and a stiffness comparable to that of bones, thus permitting an even distribution of load between the tissue and the implant and a normal bone growth. [Grassini, 2014]

The properties of bone tissues and magnesium are compared in Table 1, that shows how the density and stiffness of bones may vary, but magnesium is however more rigid than bones. Therefore the properties of magnesium can be further improved and customized to the specific implantation site by synthesizing a porous material with a controlled micromorphology.

	density	Young's modulus
	$g \cdot cm^{-3}$	GPa
bones	1 ÷ 2	0.01 ÷ 23
magnesium	1.741	45

Table 1. Properties of bones and magnesium.

1.2. Sintering process

In order to synthesize magnesium with a controlled porosity, a recently developed process called Spark Plasma Sintering (SPS) was considered [Freni, 2014]. This is a powder sintering process, based on the simultaneous compression and heating of the powder, where the heating is provided by an electrical current. The essential scheme of SPS is shown in Figure 1.

A current of several hundred Ampere runs through the sintering die containing the powder in order to reach the sintering temperature (600 °C for magnesium) and to convert the powder to a continuous material. The die is made of graphite because it conducts heat and current, resists to very high temperatures and lubricates the die. The internal temperature of the die is measured by a steel sheathed thermocouple inserted into its graphite components.

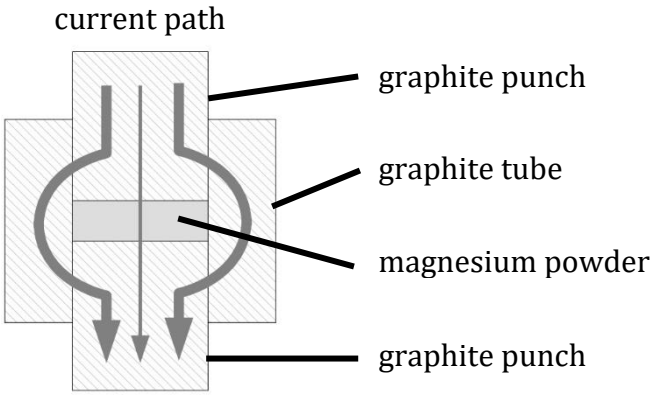

Figure 1. Distribution of current in the sintering die of SPS.

The major feature of the SPS process, that is inducing the sintering by electrical means, offers the opportunity to synthesize porous magnesium with a controlled micromorphology and predictable macroscopic properties, because the electrical current may be used not only to make the sintering proceed, but also to monitor the sintering progress in-line.

However the ordinary configuration of the process causes the major part of the current to heat the material only indirectly and the current and temperature distribution within the die is not easily predicted, as the electrical resistance of the parts may vary. Moreover, only a proximity measurement of temperature is possible, since the thermocouple can not be in direct contact with the sintered magnesium in order to avoid their soldering and the contamination of the biomaterial. Therefore the knowledge of the temperature profile is necessarily poor due to the restraints of the system.

1.3. Novel process solution

In this work an alternative configuration is proposed, the one shown in Figure 2, where an alumina tube contains the magnesium powder, thereby forcing all the injected current to run through the processed material. This way the current distribution and the temperature profile within the powder are potentially predictable, although this approach can be applied on electrically conductive materials only.

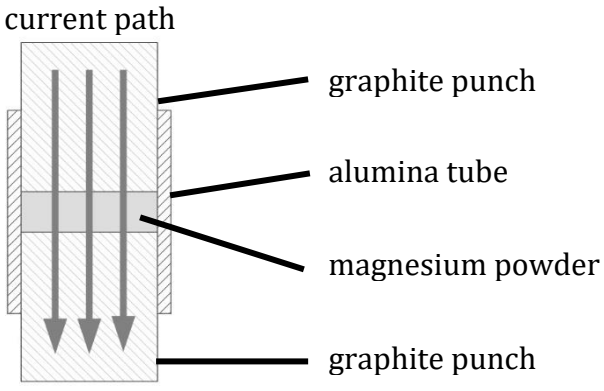

Figure 2. Distribution of current in a sintering die made of alumina.

Moreover an indirect heating of the powder extends the required sintering time, thus making the empty spaces within the powder collapse and producing a nearly bulk material. The proposed configuration instead gives the opportunity to preferentially heat the contact points between the powder particles by injecting short current pulses, so that the powder particles will join together while preserving the required porosity. The use of the alumina tube also reduces the thermal capacity of the die and the dispersion of heat, thus the required power.

Since the magnesium particles are initially covered by a film of insulating oxide, it is necessary an external filament to provide a preliminary heating to break this layer, before the actual sintering can be performed. Therefore the composite die shown in Figure 3 was designed and built to provide internal and external heating independently.

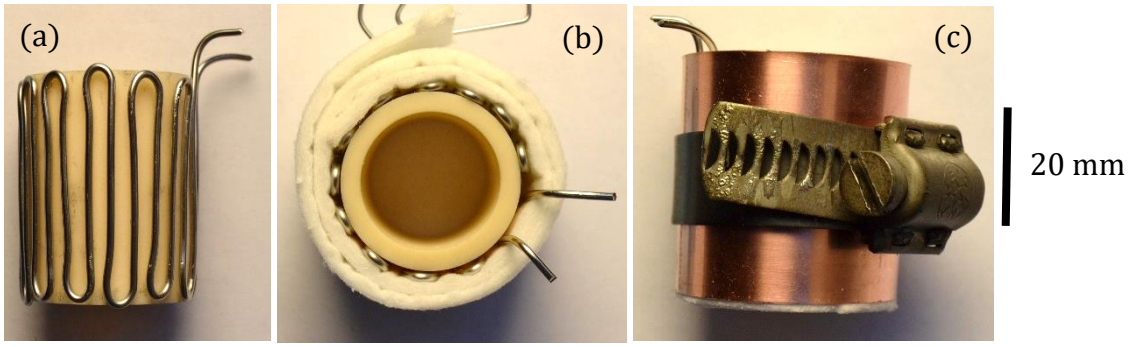

Figure 3. Design of the sintering die: alumina tube with filament (a), thermal insulating sheet (b) and copper foil with fastener (c).

The filament is wrapped in a thermal insulating sheet to reduce the heat dispersion by irradiation. A copper foil tightened by a fastener gives the whole the required stiffness. As shown in Figure 4, the die is completed by two graphite punches to compress the powder in between and by two thermal insulators used to reduce the heat dispersion by conduction.

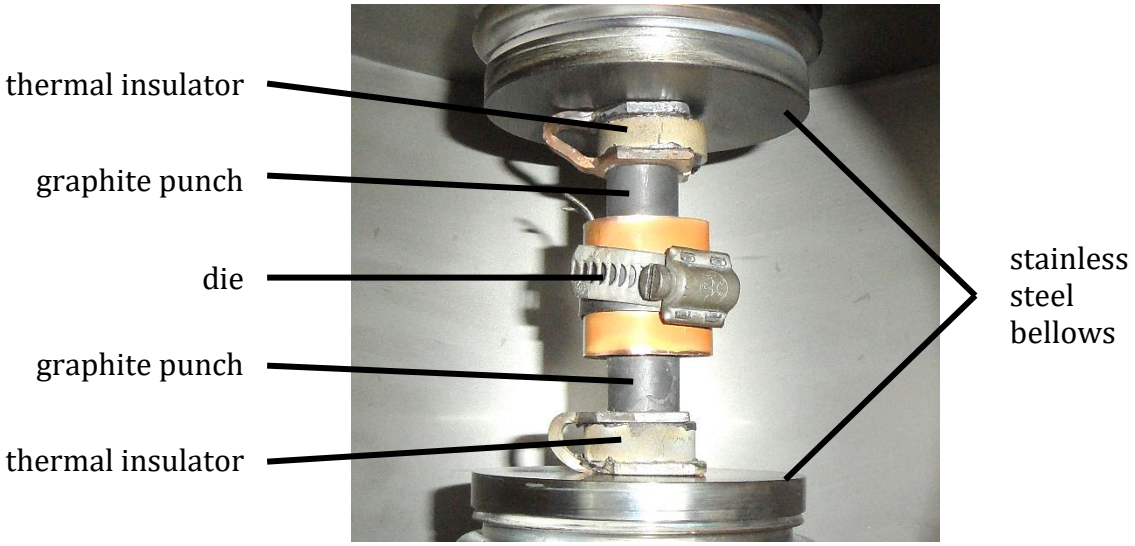

Figure 4. Full sintering set-up in the process chamber.

This novel solution is designed to control the process in the most predictable way, but its increased complexity requires a comprehensive study of the thermal distribution within the die as a function of internal and external heating powers. To this purpose a thermal model

of the sintering set-up was developed by the finite element analysis and was then validated by means of an experimental SPS apparatus.

Measurements of thermal conductivity were previously carried out on the major components of the system in order to correctly set the model parameters. The sintering apparatus was also improved by completing its monitoring system with a displacement sensor that was calibrated by the author. All these contents are found in Part I of this thesis.

1.4. Further information and experimental results

Part II of this thesis gives theoretical information about the mechanical properties of magnesium and its alloys and their corrosion behaviour in aqueous environment, as well as fundamental information about the electrochemical characterization of materials in simulated physiological environment.

Finally, Part III gives information about the sintering apparatus and the research activities performed to produce and characterize magnesium specimens with varying porosity. Both the ordinary and the developed die configurations were used to sinter magnesium powders optionally mixed with urea. This organic compound was used as a spacer powder that will decompose during the sintering process, producing only gaseous substances, thereby increasing the final porosity in a predictable manner. 7

Several density measurements were carried out to compute the open and close porosity of the produced specimens. These were also analysed by high resolution scanning electron microscopy to investigate their micromorphology, as well as by electrochemical measurements that tested their corrosion behaviour in a simulated body fluid.

Part I

Metrological results

2. Measurements of thermal conductivity

2.1. Measurements in the stationary state

The thermal conductivity of materials with a regular geometry was calculated by measuring temperature gradients in a stationary state, as shown in Figure 5. This method was applied to the graphite and alumina components of the sintering die.

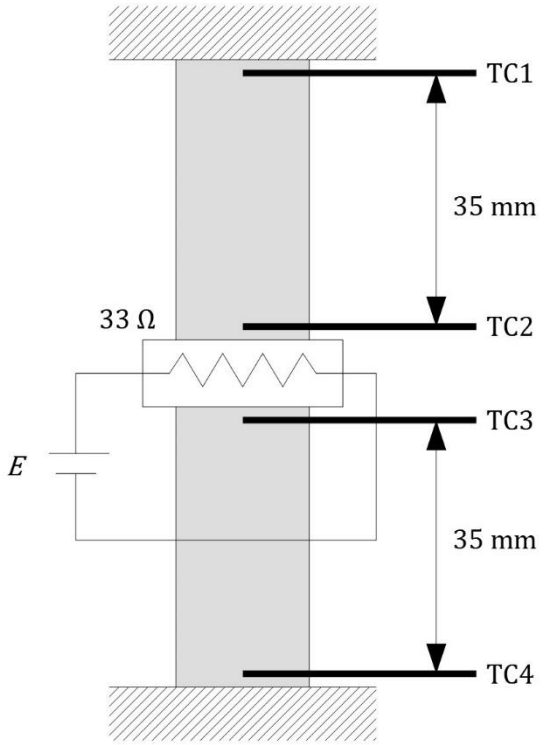

Figure 5. Measurement of thermal conductivity in the stationary state.

The heater was made of three electrical resistors with a resistance of 100 Ω and a nominal power of 5 W. The resistors were connected in parallel and inserted into an isothermal block that was an aluminium parallelepiped having dimensions 30 × 28 × 10 mm. The shape of the materials was cylindrical or tubular with a uniform cross section. Two identical components were put on the two sides of the heater in a symmetrical set-up.

The whole was mounted inside the press of the sintering apparatus to ensure an efficient thermal transfer. Moreover the chamber was evacuated during the measurement in order to avoid the heat dispersion by air convection. The heater was powered by a 20 V / 50 A generator that is part of the sintering apparatus. This is a model 6032A instrument provided by HP Inc.

A set of type K thermocouples was used to measure the temperature on both sides of the set-up, until the stationary state was reached. The thermocouples had a stainless steel sheath and were inserted into 1 mm wide holes produced in the components of the set-up. Although the set-up was symmetrical, the two halves of the apparatus did not have the same thermal resistance, therefore the two temperature gradients were different.

The thermal conductivity, k_c, was calculated by the following formula, where P denotes the heating power, d the spatial extent of the thermal gradients and A the cross sectional area, while ΔT_1 and ΔT_2 denote the temperature differentials.

$$k_c = \frac{P \cdot d}{A \cdot (\Delta T_1 + \Delta T_2)}$$

The uncertainty is estimated by the formula below. Because the heating current was as low as 0.6 A, the uncertainty in the calculation of power would have been as large as 7%. For this reason a calibration of the generator was performed as reported in a subsequent section and the power uncertainty was reduced to 0.3%.

$$u_r^2(k_c) = u_r^2(P) + u_r^2(d) + u_r^2(A) + u_r^2(\Delta T_1 + \Delta T_2)$$

A major source of uncertainty is the temperature differentials, therefore a linear correction of the thermocouple outputs was implemented by measuring the output voltages of four thermocouples at 20 °C and at 40 °C. The maximum offset correction was 6 μV and the maximum gain correction was 1.8%. This way the uncertainty of the temperature differentials was reduced to less then 0.6 °C.

2.1.1. Thermal conductivity of graphite

The thermal conductivity of graphite was measured on two cylinders having a diameter of 20 mm and a length of 42 mm. The set-up is shown in Figure 6. For each cylinder, two thermocouples were inserted into 1 mm wide holes and their measuring junction was placed on the axis of symmetry, at a distance of 35 mm from each other.

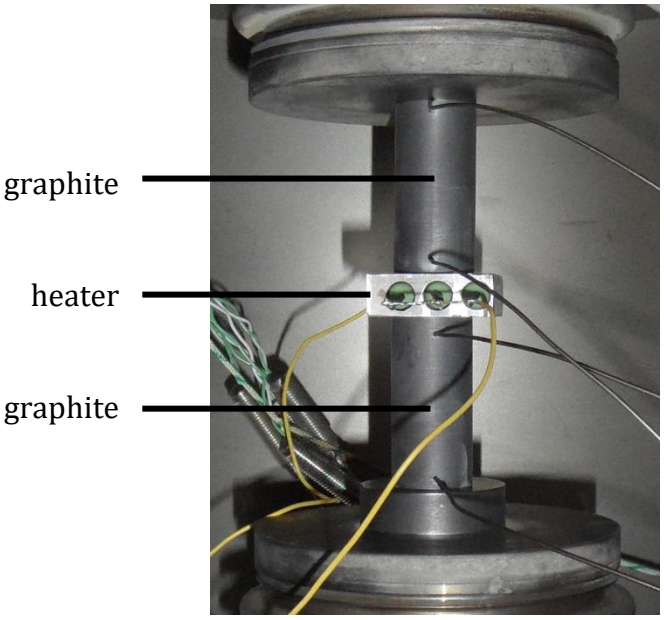

Figure 6. Measurement of the thermal conductivity of graphite.

The heater was powered with 11.68 W and heated up to 40 °C. As shown in Figure 8, the measured temperature differentials on the two sides of the set up were 5.3 °C (b – d in the figure) and 6.3 °C (c – e in the figure).

The cross sectional area of the graphite cylinders can be calculated with an uncertainty of 0.5%, while the distance between the thermocouples can be measured with an uncertainty of 0.3%. The temperature differentials were the dominant source of error and were calculated with an uncertainty of 4.7%.

Therefore the overall uncertainty is estimated as 4.7%. The thermal conductivity of graphite at 30 ÷ 40 °C equals (111 $\pm$ 5) W · m^{-1} · K^{-1}. This result is consistent with what expected for an isostatically moulded graphite at low temperature, as discussed in a subsequent section.

2.1.2. Thermal conductivity of alumina

The thermal conductivity of alumina was measured on two tubes having an internal diameter of 20 mm, an external diameter of 26 mm and a length of 35 mm. The set-up is shown in Figure 7. Although it was not possible to make holes in the alumina tubes, their conductivity was the smallest in the set-up, thus the thermocouples can be put in proximity of the tubes with a small error.

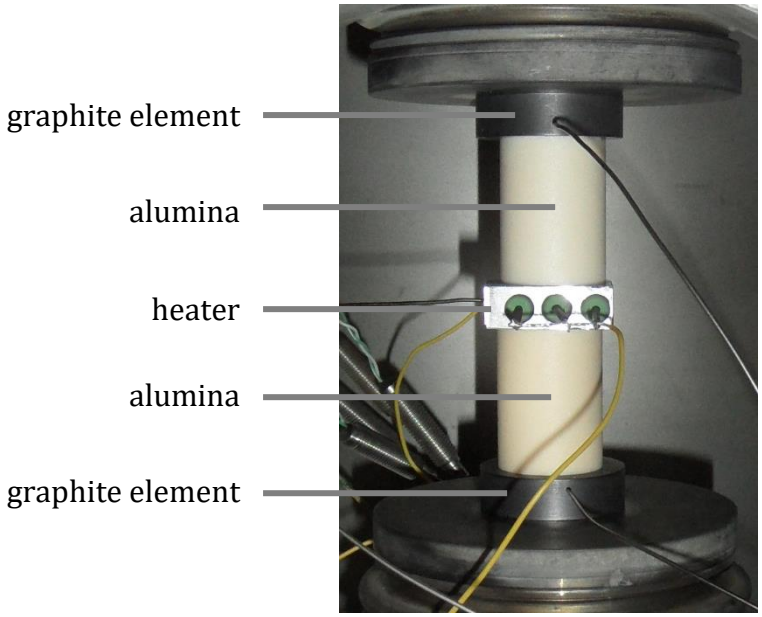

Figure 7: Measurement of the thermal conductivity of alumina.

Therefore one thermocouple was used to measure the temperature of the heater, while for each tube the lower temperature was measured by inserting a thermocouple into a graphite element, at a distance of 2 mm from the edge of the tube. This graphite element was cylindrical, with a diameter of 36 mm and a height of 10 mm. The spatial extent of the thermal gradients can be equated with the full length of the tubes, increased by 0.5 mm.

The heater was powered with 11.68 W and heated up to 64 °C. As shown in Figure 9, the measured temperature differentials on the two sides of the set-up were 31.9 °C (b – c in the figure) and 33.6 °C (b – d in the figure).

The cross sectional area of the alumina tubes can be calculated with an uncertainty of 1.7%, while the length of the tubes can be measured with an uncertainty of 0.1%. The temperature differentials were calculated with an uncertainty of 0.5%.

Therefore the overall uncertainty is estimated as 1.8%. The thermal conductivity of alumina at 30 ÷ 65 °C equals (29.4 $\pm$ 0.5) W · m^{-1} · K^{-1}. This result is consistent with what expected for this material at low temperature, as discussed in a subsequent section.

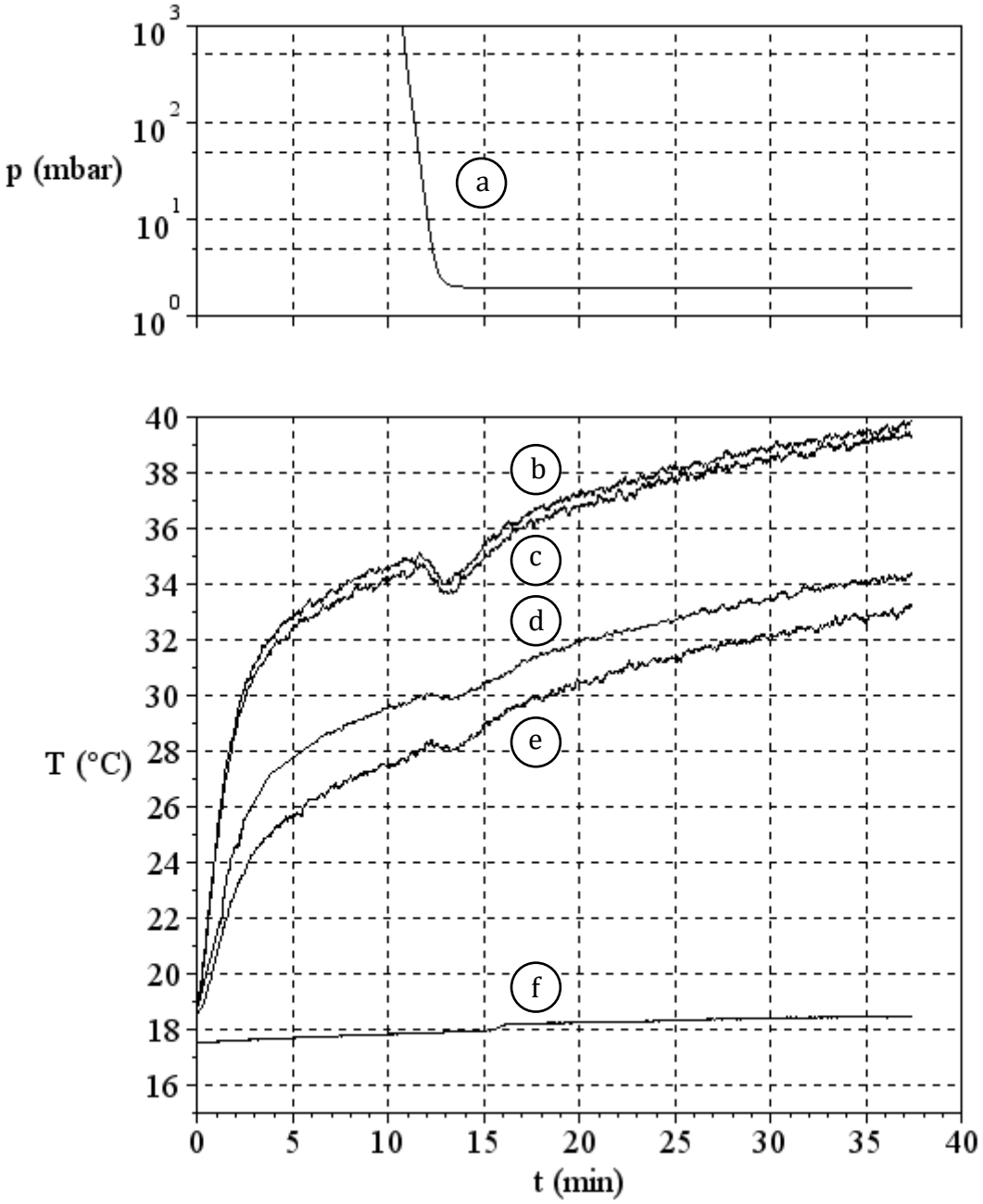

Figure 8. Measurement of the thermal conductivity of graphite: air pressure (a), measured temperatures (b ÷ e) and reference temperature (f).

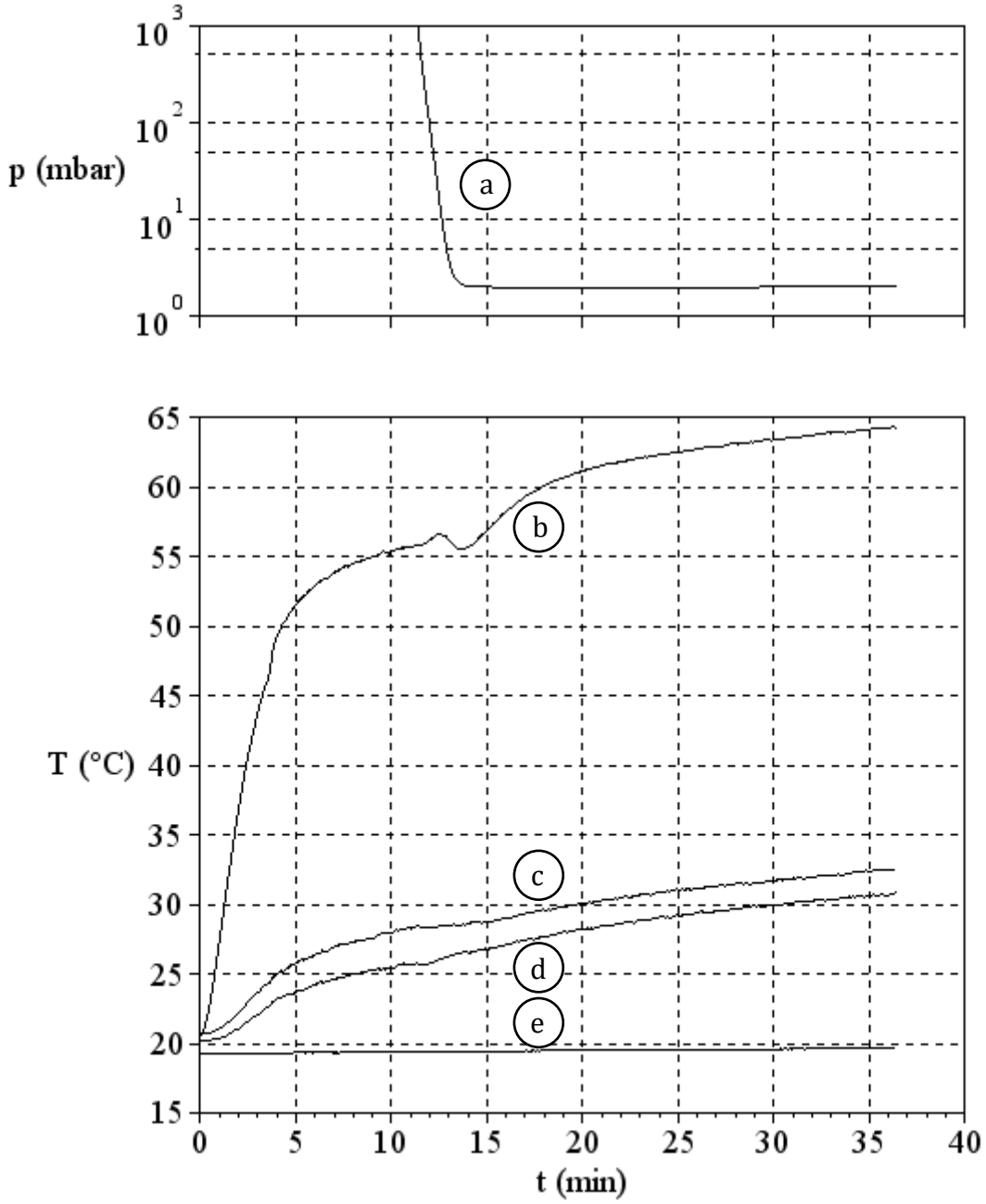

Figure 9. Measurement of the thermal conductivity of alumina: air pressure (a), measured temperatures (b ÷ d) and reference temperature (e).

2.2. Measurement in the transient state

The thermal conductivity of the magnesium powder was measured in the transient state, by the hot wire method described by Vozár [Vozár, 1996], as shown in Figure 10 and Figure 11.

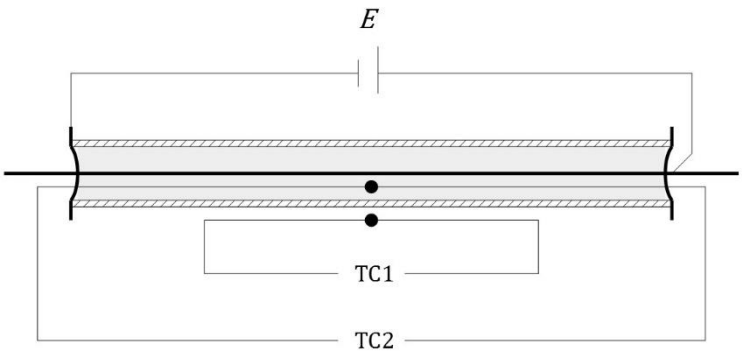

Figure 10. Measurement of the thermal conductivity in the transient state.

A quartz tube filled with powder was heated by a filament lying on the axis of symmetry. The tube had an inner diameter of 8 mm, an outer diameter of 10 mm and a length of 200 mm. It was filled with 5.70 g of magnesium powder, therefore the density of the powder was 0.57 g $\cdot$ cm^{-3}.

Two copper sheets were used to close both the ends of the tube. Each of them had a hole in the centre for the filament and another hole for a thermocouple. The sheet closing the bottom of the tube was stuck to the tube by means of epoxy resin, while the one at the top was free to move.

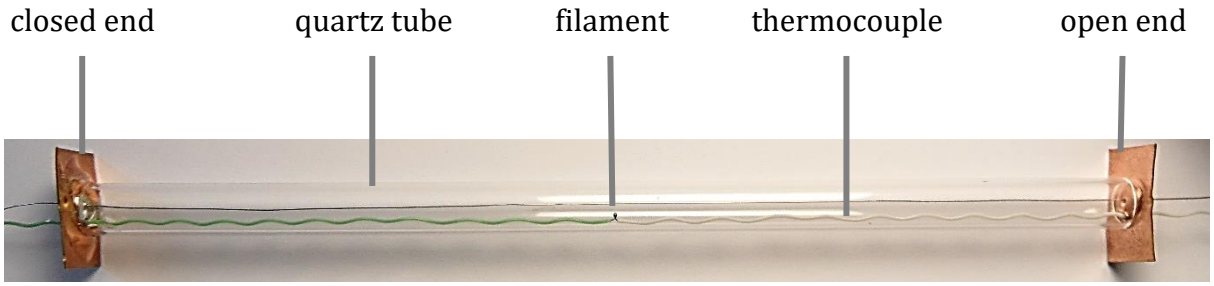

Figure 11. Construction of the set-up before filling with powder.

The heating filament had a diameter of 0.2 mm and it was made of a nickel-chromium alloy with a 20% by weight of chromium. At the lower end, the wire was soldered to the copper sheet, while at the upper end it was fixed with a crocodile clip. The resistance of the wire was 6.12 Ω. The set-up was powdered at 4.95 W by a 20 V / 4 A generator. This was a model 6622A instrument provided by HP Inc.

Two thermocouples were used to measure the temperature both inside and outside the tube. They were type K thermocouples with the two wires separately insulated by a PTFE sheath. The measuring junction of the internal thermocouple was located at half the length of the tube. The outer thermocouple was used exclusively to check that the external temperature was constant.

In the temperature vs. time diagram, with time on a logarithmic scale, the transient state will appear as a straight line with slope K, as shown in Figure 12. This can be used to calculate the thermal conductivity, k_c, by the formula below, where P denotes the power and L denotes the filament length. The parameter K was calculated by regression from the linear segment of the curve, which was automatically selected by a specific algorithm that minimized the average squared deviation.

$$k_c = \frac{P}{4 \cdot \pi \cdot L \cdot K}$$

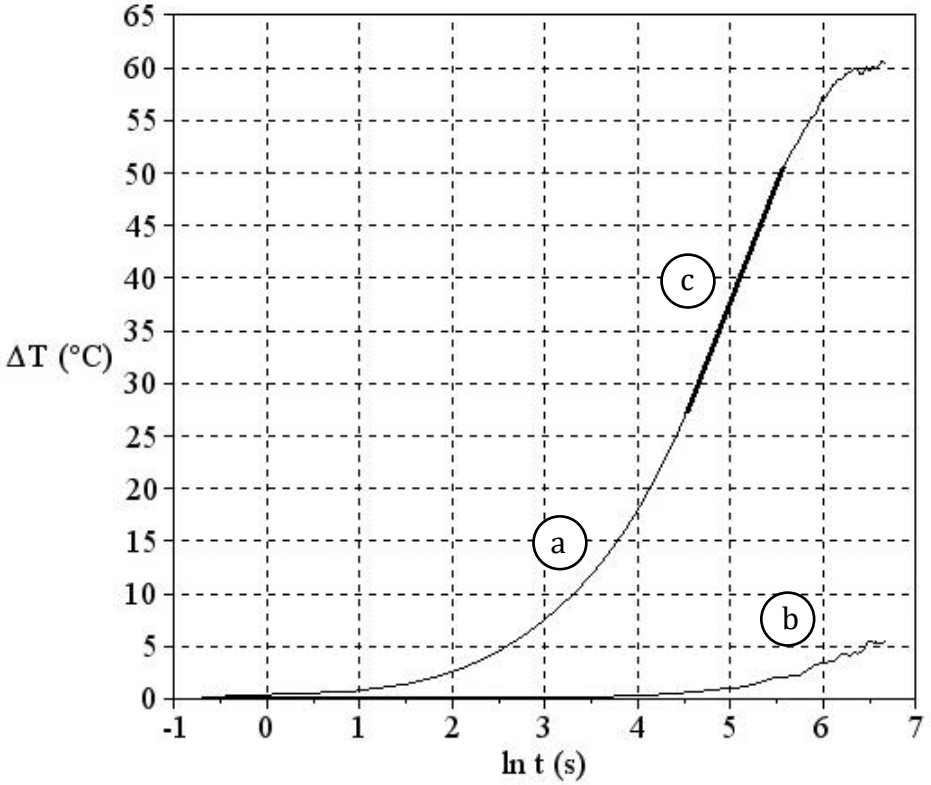

Figure 12. Measurement of the thermal conductivity on magnesium powder: internal (a) and external (b) temperature change and model (c).

The uncertainty is estimated by the formula below, where ΔT denotes the temperature change during the linear segment of the transient state. This is the major source of uncertainty. Since the temperature interval equals 23 °C, its relative uncertainty can be estimated as 2%.

$$u_r^2(k_c) = u_r^2(P) + u_r^2(L) + u_r^2(\Delta T)$$

The uncertainty of the generator was equal to 0.05% of reading + 0.050 V for voltage and 0.01% of reading + 0.008 A for current. Since the voltage was 5.5 V and the current was 0.9 A, the power uncertainty was 1.3%. The effective length of the filament can be measured with an uncertainty of 1%. Therefore the overall uncertainty is estimated as 2.6%.

Three repetitions were carried out and the repeatability was within the uncertainty. The linear fitting was applied between 45 °C and 70 °C. The thermal conductivity of the magnesium powder is equal to (86 ± 2) mW · m^{-1} · K^{-1}.

3. Thermal model of the sintering process

3.1. Development of the model

A thermal model of the sintering process was developed by the FreeFEM++ finite element analysis software, version 3.26-3, provided by the Jacques-Louis Lions Laboratory of the Pierre and Marie Curie University.

3.1.1. Design of the system

The system is essentially made of a sintering die with two equal graphite punches inserted into an alumina tube and filled with magnesium powder. A filament is used to externally heat the die and is wrapped in a thermal insulating sheet. A fastener is used to compress a copper foil around the insulating sheet in order to give the whole a sufficient rigidity and to reduce the heat dispersion by irradiation. Two alumina tubes used as thermal insulating elements are put above and below the die, with a copper bridge that permits the passage of current.

The design of the system is shown in Figure 13a and the dimensions are reported in Table 2.

nominal diameter	20	mm
height of the powder	6	mm
height of the punches	31	mm
outer diameter of the tube	26	mm
height of the tube	35	mm
diameter of the filament	1.2	mm
pitch between the turns	4	mm
outer diameter of the coat	40	mm
height of the insulators	10	mm
inner diameter of the insulators	20	mm
outer diameter of the insulators	32	mm
thickness of the copper bridges	3	mm

Table 2. Dimensions of the modelled system.

3.1.2. Design of the mesh

The system geometry was defined by taking advantage from the axial symmetry of the sintering die. Consequently, a heating filament coiled around the alumina tube was modelled as equivalent to the real zig zag shaped filament. The equivalent coil is made of nine turns with a 4 mm pitch and the cross section of the wire was equated to a square having a side of 1 mm.

The copper elements bridging the thermal insulators do not have an axial symmetry either and they were replaced by equivalent symmetrical elements with reduced thickness.

Two fictitious cylindrical elements were added above and below the system to reproduce the pistons and bellows that dissipate heat by conduction and to equalize the temperature

at the outer borders of the system. These elements have a diameter of 30 mm and a height of 2 mm.

The linear density of vertices along the borders is 2 mm^{-1} in most cases, but it becomes as large as 8 mm^{-1} on the borders of the filament, where an intense divergence is expected in the heat flux. The density of vertices is nowhere smaller than 1 mm^{-1}.

The design of the mesh is shown in Figure 13b and some quantities are reported in Table 3.

number of vertices	16033	
number of triangles	31244	
area of the mesh	12.3	cm^2
average density of vertices	13.0	mm^{-2}
average area of triangles	0.039	mm^2

Table 3. Details of the mesh.

3.1.3. Boundary conditions

The Dirichlet boundary condition was set at the outer border of the fictitious elements representing the pistons and bellows that dissipate heat by conduction. The room temperature was set at 24 °C. The overall thermal resistance was calculated from the results of previous experiments and was set at 1.15 $K \cdot W^{-1}$.

The Neumann boundary condition was set at the exposed borders of the thermal insulating sheet and the graphite punches in order to compute the radiative heat transfer. The heat flux, $\dot{Q}_{\mathrm{rad}}$, was computed by the following formula, where ϵ denotes the emissivity, σ the Stefan-Boltzmann constant, A the surface area, T the absolute temperature of the surface and T_0 the absolute temperature of the chamber walls.

$$\dot{Q}_{\mathrm{rad}} = \epsilon \cdot \sigma \cdot A \cdot \left(T^4 - {T_0}^4\right)$$

The Stefan-Boltzmann constant equals $5.670 \cdot 10^{-8}\ W \cdot m^{-2} \cdot K^{-4}$. The temperature of the chamber walls was set at 25 °C, which is the average temperature of the water of the cooling system. Emissivity was set at 0.8 for graphite and 0.07 for the copper foil, as recommended by Omega Engineering Inc. and Infrared Services Inc.

3.1.4. Parameters

The thermal conductivity of copper was set at 400 $W \cdot m^{-1} \cdot K^{-1}$, while the conductivities of graphite, alumina and the insulating sheet were calculated by the software as functions of the local temperature. The functions used to compute the thermal conductivities are reported in a subsequent section and are summarized below.

The conductivity of graphite is calculated from the data reported by GrafTech International Ltd. for an isostatically moulded graphite. The conductivity of alumina was calculated by the formula reported by Kita [Kita, 2015]. The conductivity of the insulating sheet was calculated by second degree polynomial regression from the data reported by Morgan Advanced Materials plc.

The conductivity of the magnesium powder was measured at low temperature as reported in a previous section and was set at 86 $mW \cdot m^{-1} \cdot K^{-1}$. However this value does not consider the effect of sintering. Therefore at temperatures above 500 °C the sintered magnesium is equated to bulk magnesium and its conductivity is calculated by linear regression from the data given by the International Magnesium Association as discussed in a subsequent section.

The model permits to set the filament power and the injected power independently. The injected power is assumed to heat the powder only, with a uniform power density.

3.1.5. Algorithm

The Cholesky factorization was used for solving the model. Since the software does not compute irradiation, an algorithm was developed that neglects irradiation in the first place. This is needed to have a first approximation of the surface temperature before calculating the radiative heat flux.

Then the algorithm gradually increases the emissivity of the hot surfaces and repeatedly computes the solution by changing the Neumann boundary conditions accordingly. Twenty repetitions are carried out while the emissivity increases linearly, in order to keep the algorithm stable and convergent.

Moreover at each repetition the boundary conditions are adjusted by smaller steps, equal to one tenth of the required variation. These steps are repeated until the temperature in any vertex of the mesh is stable within a variable tolerance. As the repetitions are carried out the temperature tolerance gets progressively smaller until it sets at 0.1 °C.

Finally the software computes the minimum and maximum of temperature and thermal conductivity in each major component of the system. It also computes the average temperature in selected 1×1 mm locations throughout the mesh, to be compared with the experimental results.

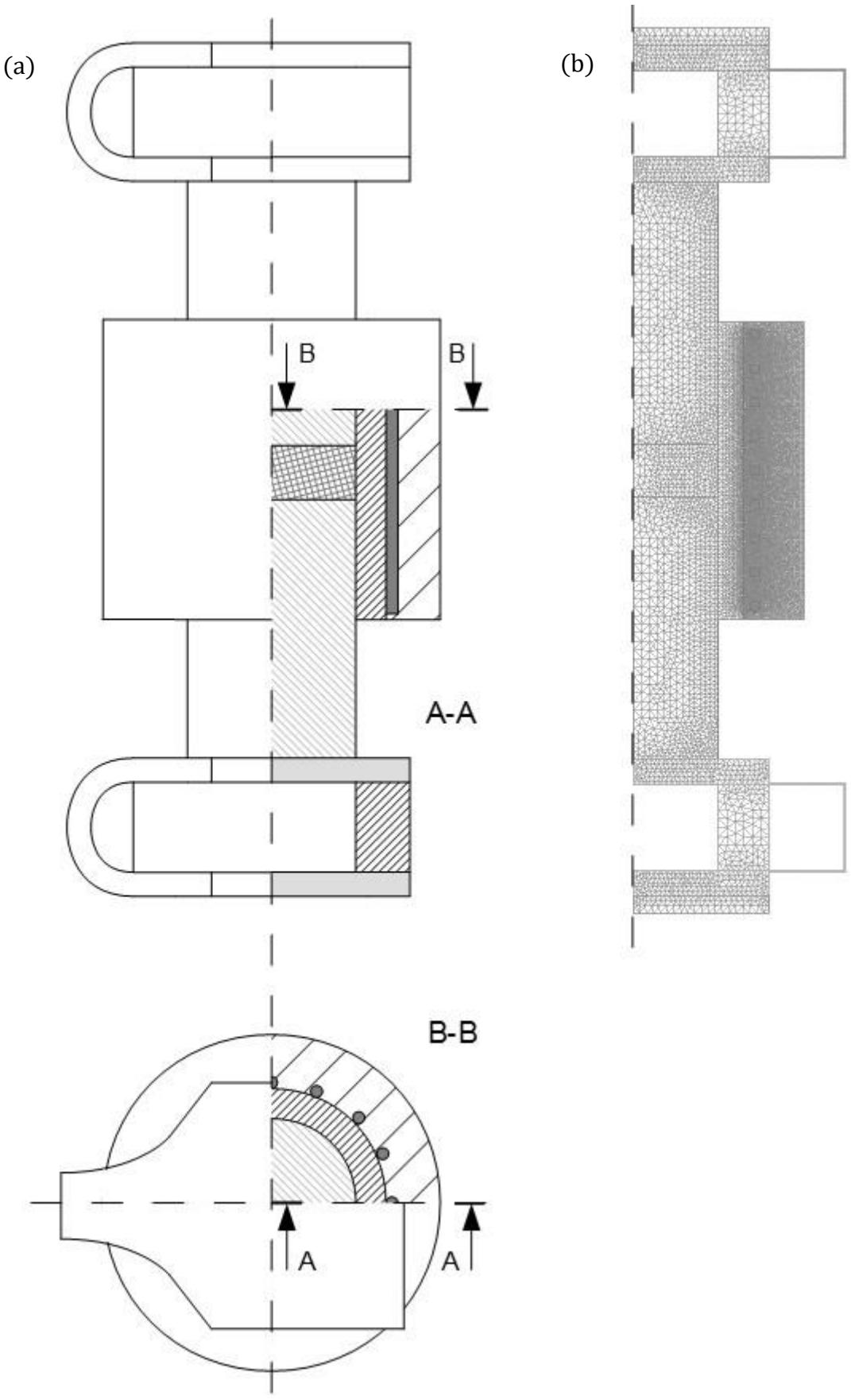

Figure 13. Design of the system (a) and design of the mesh (b).

3.2. Results and validation

The model was run in two modes:

- the pre-heating mode is implemented by setting the filament power at 195 W and the injected power at 1 W; this mode represents the pre-heating of the die and was used to perform the validation of the model;
- the sintering mode is implemented by setting the filament power at 195 W and the injected power at 58 W; this mode represents the actual sintering process, to be carried out at 600 °C.

3.2.1. Results

The results obtained from the model are reported in Table 4.

	pre-heating	sintering	
filament power	195	195	W
injected power	1	58	W
temperature of magnesium	465 ÷ 488	599 ÷ 602	°C
simulated thermocouple	456	593	°C
thermal conductivities			
magnesium	0.086	131	$W \cdot m^{-1} \cdot K^{-1}$
punches	74 ÷ 81	62 ÷ 73	$W \cdot m^{-1} \cdot K^{-1}$
tube	10.2 ÷ 10.5	9.8	$W \cdot m^{-1} \cdot K^{-1}$
thermal insulating sheet	0.11 ÷ 0.20	0.13 ÷ 0.22	$W \cdot m^{-1} \cdot K^{-1}$
thermal insulators	0.34 ÷ 0.45	0.31 ÷ 0.41	$W \cdot m^{-1} \cdot K^{-1}$

Table 4. Results of the thermal model.

The obtained temperature maps are shown in Figure 14a and Figure 15. The maximum temperature is reached by the filament, and it equals the maximum operating temperature of 1150 °C. The temperature inside the powder before is comprised in a range of 23 °C, while after the sintering this interval is reduced to 3 °C. In general the temperature of magnesium is not uniform, the central layer being warmer then the upper and lower layers.

A computed temperature value was sampled in proximity of the powder to simulate a measurement performed by a thermocouple. The selected location has a 1 × 1 mm area and lies on the axis of symmetry, 1 mm below the powder. The maximum difference between the simulated measure and the temperature of any part of the powder is 32 °C, therefore the model must be used to correct the measured temperature.

The thermal conductivity of all the components of the die show some variability The thermal insulating sheet has the most significant variability and its thermal conductivity is mapped in Figure 14b.

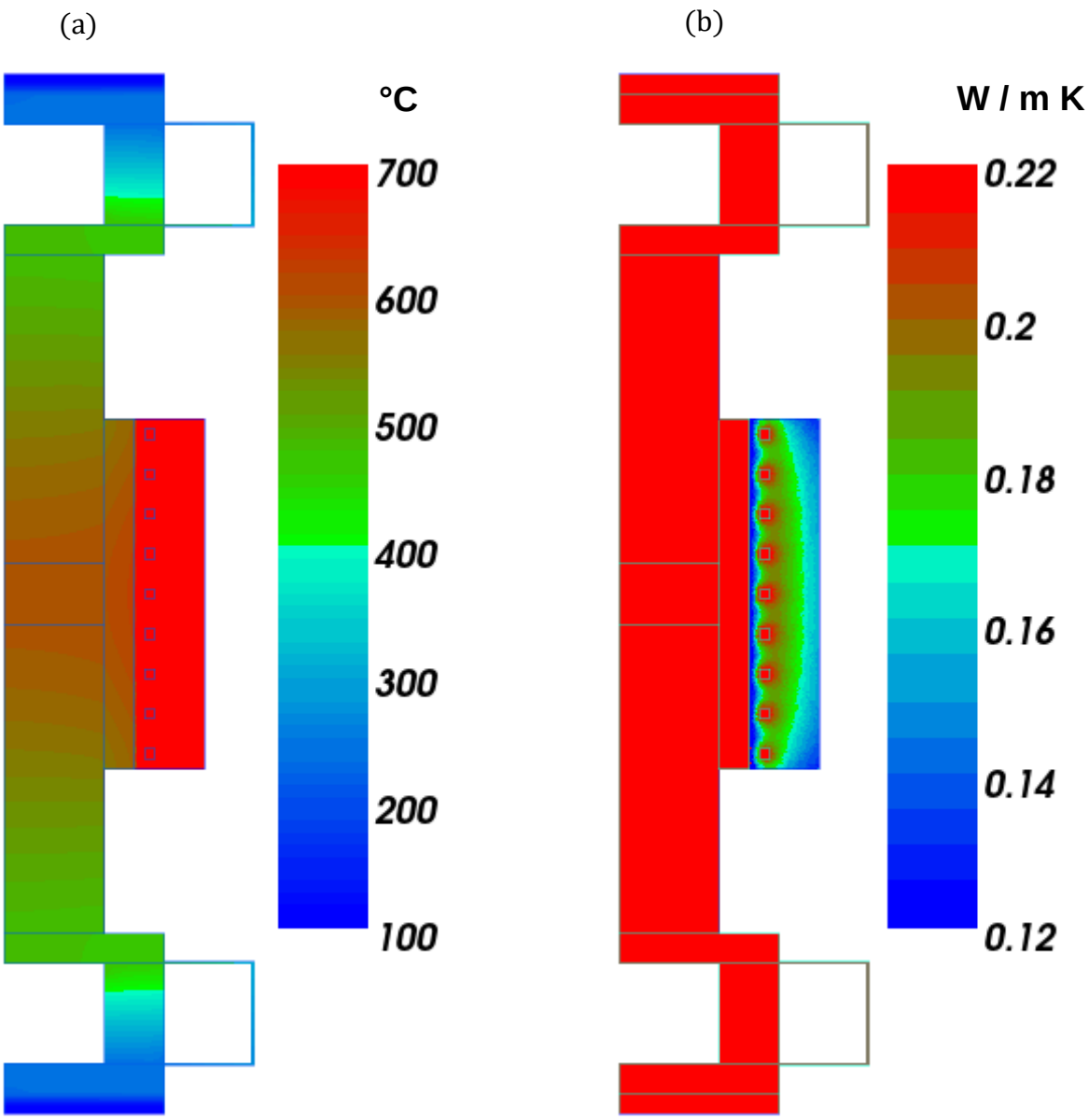

Figure 14. Computed temperature (a) and computed thermal conductivity of the insulating sheet (b) during the sintering at 600 °C.

3.2.2. Validation

The validation of the model was performed by setting up the system described in Figure 13a and by running the pre-heating of the die. Six thermocouples were inserted in the locations indicated in Figure 16 to map the temperature:

- thermocouple 'a' was inserted into the thermal insulating sheet, in the nearest point to the filament, still avoiding the electrical contact; this is the hottest point in the system that can be measured by a thermocouple;
- thermocouple 'b' was inserted between the thermal insulating sheet and the copper foil; this measurement was performed to estimate the radiative heat flux;
- thermocouple 'c' was inserted into the lower punch, on the axis of symmetry, at a distance of about 1 mm from the powder; this returns the nominal temperature of the powder;
- thermocouple 'd' was also inserted into the lower punch, on the axis of symmetry, at a distance of about 1 mm from the base;
- thermocouples 'e' and 'f ' were both put in contact with the outer parts of the copper bridges; they return the temperature at the borders of the system.

The thermal process is reported in Figure 17. A linear power ramp was performed from 0 to 195 W in 180 min and then the power was maintained for 40 min. The measured temperatures consequently increased and then stabilized at a stationary state. The experimental results are compared in Table 5 to the computed temperatures sampled in the corresponding locations of the model.

thermocouple	measured	computed	error	
a	980 ± 7	975	–5	°C
b	879 ± 6	866	–13	°C
c	437 ± 3	456	+19	°C
d	389 ± 3	388	–1	°C
e	190 ± 2	194	+4	°C
f	194 ± 2	194	0	°C

Table 5. Results of the validation.

The computed temperatures are substantially consistent with the experimental results, as the differential temperatures measured by the thermocouples differ by less then 4% from the computed values.

The thermocouple located near the filament (a) is the less likely to match because of the intense thermal gradient found in proximity of the filament, but the computed temperature sampled 0.5 mm away from the central turn of the coil is a good estimation of the measured value. However the largest observed errors refer to the thermocouple located outside of the thermal insulating sheet (b) and to the one located in proximity of the powder (c). In fact the model tends to overestimate the temperature of the core of the die and to underestimate the temperature in the outer part.

The discrepancy may be due to a major limit of the model, that neglects the vacuum between the alumina tube and the filament. In fact the wire has a round cross section and it is not in

close contact with the tube, while the surrounding sheet is pressed against the tube, therefore in this simplified bi-dimensional model the real configuration can not be accurately represented. In the model the empty spaces between the filament and the tube are emulated by a small layer of insulating sheet in between.

Moreover the actual conductivity of the insulating sheet may be larger then what stated by the manufacturer, because the fibres are compressed by the copper foil and the empty spaces in between are partially collapsed. However increasing the conductivity of the sheet will also result in an increased heat transfer toward the core of the die in this simplified model.

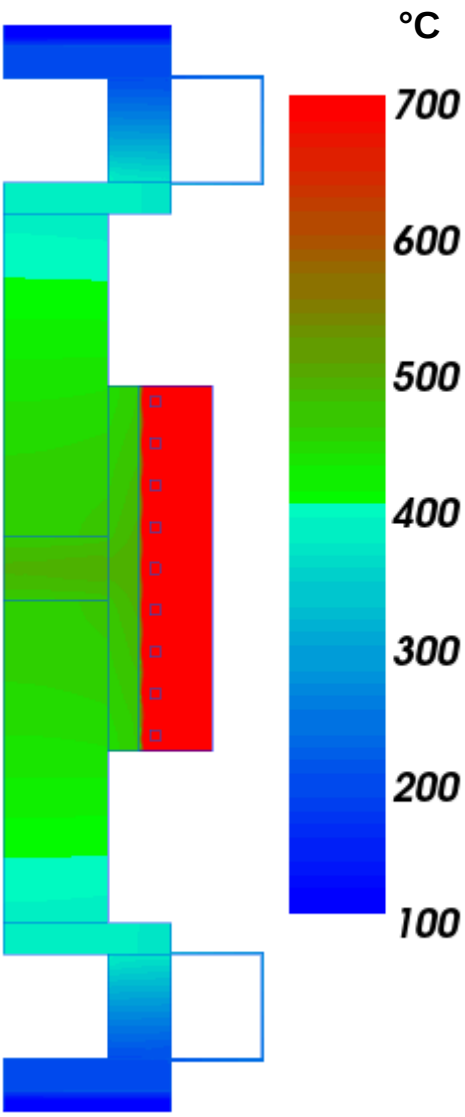

Figure 15. Computed temperature map during the pre-heating of the die.

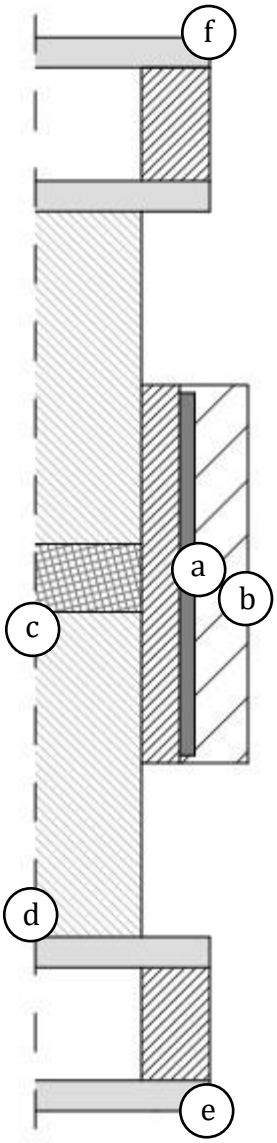

Figure 16. Location of the thermocouples used for the validation.

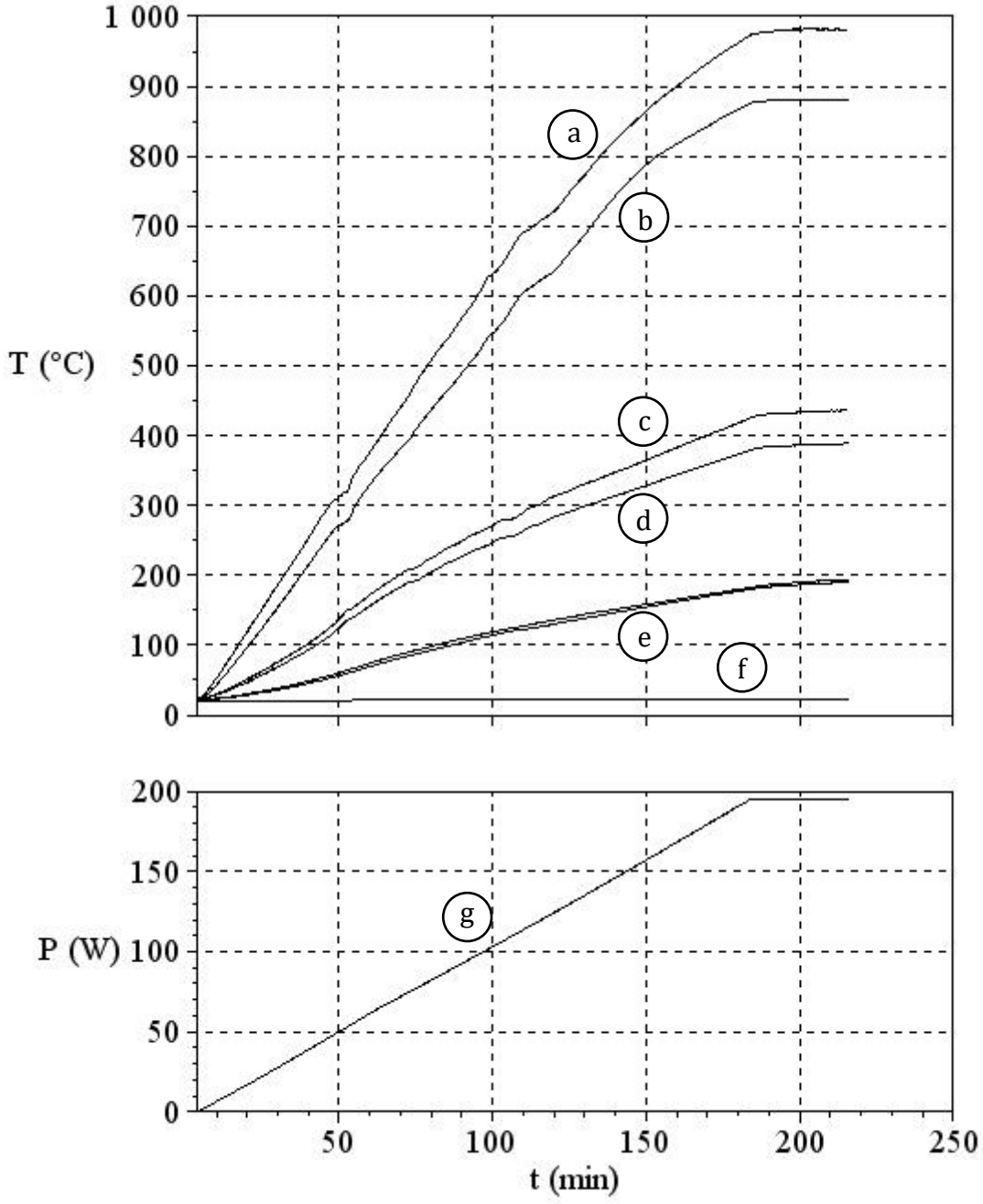

Figure 17. Results of the validation: measured temperatures (a ÷ e), refer. temperature (f) and heating power (g).

4. Calibration activities

4.1. Calibration of a generator

The 20 V / 50 A generator that was used for the measurements of thermal conductivity in the stationary state was calibrated between 0.1 A and 0.6 A to reduce the measurement uncertainty. The same 33 Ω resistor was used for the measurement of the thermal conductivity and for the calibration. A model 34411A digital multimeter provided by Agilent Technologies Inc. was used to measure the generated current with a resolution of 0.01 mA.

The calibration curve is reported in Figure 18, where I_{set} denotes the set current and I_{meas} the measured current. The linear regression returned an offset of 3.9 mA and a gain of 1.002. The maximum deviation from linearity equals 0.3 mA. After the calibration the uncertainty in the calculation of power was reduced to 0.3%.

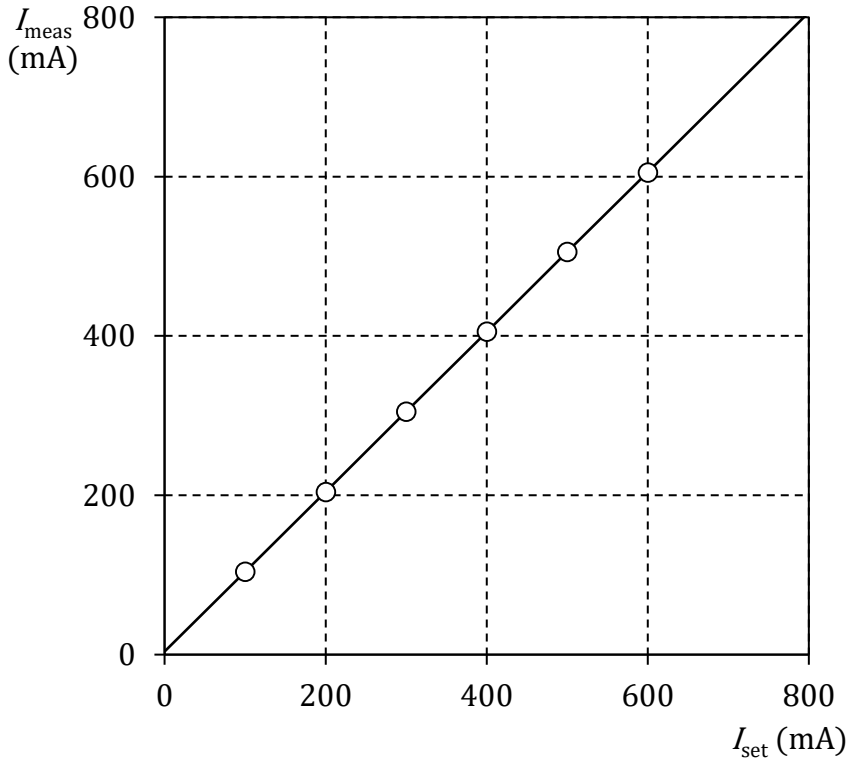

Figure 18. Calibration curve of the HP 6032A generator for small currents.

4.2. Measurement of displacement

The lower piston of the press was equipped with an external shaft coupling with a displacement sensor. This is a model D22-5S linear variable displacement transformer (LVDT) provided by Shinko Denshi Co. Ltd. The sensor is powered by a 12 V direct voltage and returns an analog output between −4.1 V and +5.7 V.

Since the datasheet is not available, the sensor was calibrated by the author. The zero displacement was set at the upmost position of the piston, therefore a negative displacement is associated to any other piston position, although the probe of the sensor can slide also by positive displacements.

The calibration was carried out by inserting an increasing number of foils between the shaft and the sensor probe. All the foils had a thickness of 0.1 mm and the whole interval of displacements between –2.7 mm and +0.8 mm was covered. The obtained calibration curve is reported in Figure 19, where z denotes the displacement and V the output.

As expected, the output is linear respect to the displacement, with a maximum deviation of 0.03 mm, corresponding to a 0.9% of linearity error. The obtained transduction function is the following.

$$z = -4.70\ \text{mm} + 1.47\ \frac{\text{mm}}{\text{V}} \cdot V$$

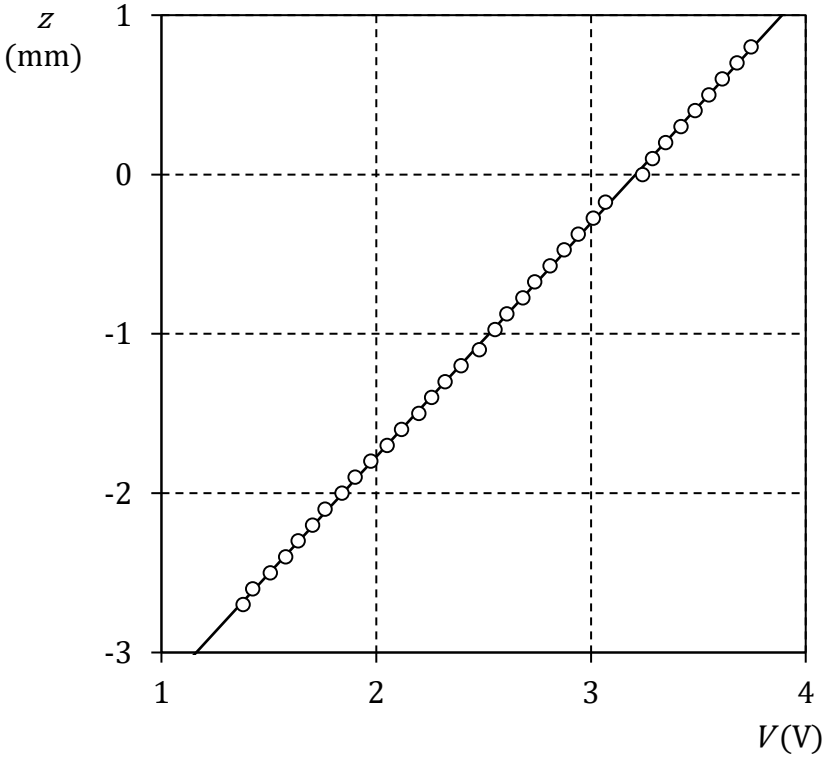

Figure 19. Calibration curve of the displacement sensor.

4.3. Off-line measurement of force

The force generated by the press of the sintering apparatus was measured by a load cell in order to verify the effectiveness of the oleodynamic system. The load cell is a model LCM202 sensor with a range of 50 kN provided by Omega Engineering Inc. It is powered by a 10 V direct voltage and returns an analog output, V, proportional to the input, E, and the load, F.

$$F = 20.10\ \frac{\text{kN} \cdot \text{V}}{\text{mV}} \cdot \frac{V}{E}$$

The uncertainty of the sensor is 0.25%. The measurements were carried out with loads between 11.5 kN and 20 kN and no discrepancy between the measured force and the oil pressure was observed, as permitted by the resolution of the manometer.

Due to geometrical restraints, it was not possible to implement the load cell for an in-line measurement.

Part II

Theoretical information

5. Magnesium metal and alloys

5.1. Pure magnesium

Magnesium is the lightest of the metals which find structural applications. It is a low melting metal which is used for castings, although its coefficient of thermal expansion is the highest among structural metals. It has the highest specific heat capacity, in comparison with iron, aluminium, titanium, nickel and copper, but its thermal diffusivity is also very high thank to its low density. The following physical and mechanical properties of magnesium and other metals were reported by Nicodemi [Nicodemi, 2008].

Magnesium crystallizes with the hexagonal close packed lattice. Table 6 reports some physical properties of magnesium with a 99.8% purity. Density, specific heat capacity and conductivities refer to 20 °C. Coefficient of thermal expansion refers to 0 °C. Temperature coefficients refer to 0 ÷ 100 °C.

density	1.741	$kg \cdot dm^{-3}$
thermal conductivity	158.4	$W \cdot m^{-1} \cdot K^{-1}$
specific heat capacity	1.05	$kJ \cdot kg^{-1} \cdot K^{-1}$
coefficient of thermal expansion	$24.80 \cdot 10^{-6}$	K^{-1}
temperature coefficient of thermal expansion	$+9.61 \cdot 10^{-9}$	K^{-2}
electrical conductivity	22.4	$m \cdot \Omega^{-1} \cdot mm^{-2}$
temperature coefficient of electrical resistance	+0.0145	$\Omega \cdot mm^2 \cdot m^{-1} \cdot K^{-1}$
melting point	650	°C
heat of fusion	372.6	$kJ \cdot kg^{-1}$
volume change on melting	+4.1	%

Table 6. Physical properties of magnesium.

Table 7 reports some mechanical properties of magnesium with a 99.8% purity, in three metallurgical states. Mechanical resistance is improved by strain hardening after the cold working, compared to the hot worked material.

	as cast	hot worked	cold worked	
Young's modulus	45			GPa
shear modulus	18			GPa
yield strength	21	98	190	MPa
ultimate strength	85	190	260	MPa
elongation at failure	5	15	10	%
Brinell hardness	30	40	50	

Table 7. Mechanical properties of magnesium.

Most structural applications of magnesium are justified by its very high specific strength, which is the ratio between tensile strength and density. This is an important parameter in the applications where load is substantially determined by weight, like transport systems. The specific strength of any material is proportional to its breaking length, that is the length of the longest cable hung vertically which bears its own weight.

Table 8 compares density, ultimate strength and breaking length of the most used metals. Breaking length of magnesium is at least double respect to that of any other. Density refers to 20 °C. Ultimate strength is approximate and refers to the hot worked material.

	density	ultimate strength	breaking length
	$kg \cdot dm^{-3}$	MPa	km
magnesium	1.74	190	11
titanium	4.51	250	5.5
nickel	8.90	320	3.6
iron	7.87	250	3.2
copper	8.93	220	2.5
aluminium	2.70	60	2.2

Table 8. Compared properties of several metals.

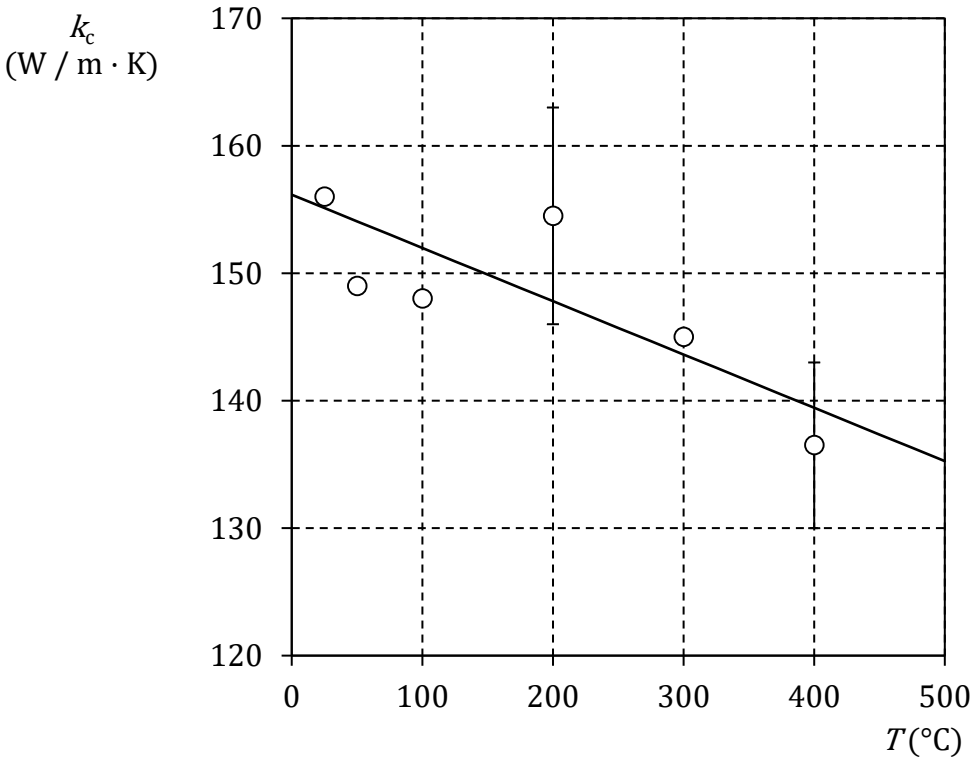

Figure 20. Thermal conductivity of magnesium.

The thermal conductivity of magnesium can be calculated by the function below, where k_c denotes the conductivity and T denotes the temperature in Celsius degrees.

$$k_\mathrm{c} = 156\ \frac{\mathrm{W}}{\mathrm{m}\cdot\mathrm{K}} - 0.04180\ \frac{\mathrm{W}}{\mathrm{m}\cdot\mathrm{K}^2}\cdot T$$

The function was obtained by linear regression from the data given by the International Magnesium Association between 0 °C and 400 °C, as shown in Figure 20. The maximum deviation of the model from the data equals 6.7 $\mathrm{W}\cdot\mathrm{m}^{-1}$.

5.2. Magnesium alloys

An overview concerning the properties of magnesium alloys was composed by Nicodemi [Nicodemi, 2008]. Detailed properties of the alloys are reported by the datasheets provided by Magnesium Elektron Ltd., Superform Products Ltd. and Kenwalt Die Casting Co.

Magnesium alloys are divided into two classes: the ones containing aluminium and manganese and the ones containing zirconium. They are generally designed to increase the poor mechanical and corrosion properties of the metal without excessively increasing its density. Most of them are used as cast alloys, although also wrought alloys have been developed.

5.2.1. Main alloying elements

Aluminium is soluble in magnesium by 12% at 450 °C and strengthens the alloy by precipitation of an eutectic compound with formula $Mg_{17}Al_{12}$. The tensile performance of cast alloys is optimal for a 6% aluminium content, while hardness increases further for higher concentrations. Aluminium is the lightest of the alloying elements, except lithium, and maintains the thermal expansion coefficient of magnesium. It improves the corrosion resistance, but strongly reduces the thermal and electrical conductivities.

Manganese is not soluble in magnesium and is added to the magnesium-aluminium alloys by 0.3% ÷ 0.6% for improving their corrosion behaviour.

Zirconium is not soluble in magnesium and is added to magnesium with a concentration of about 0.6% for its grain refinement effect. This would be hindered in presence of aluminium or manganese in the alloy, because of the formation of intermetallic compounds.

Zinc is a common alloying element in both classes of alloys and is soluble by 3% at 350 °C. As in the case of aluminium, zinc strengthens magnesium by precipitation of an eutectic compound and the tensile properties of cast alloys are maximum for a 5% of zinc content. Moreover zinc improves the corrosion resistance of magnesium, but markedly increases its thermal expansion coefficient.

5.2.2. Designation

The composition of the magnesium alloys is commonly denoted following the ASTM B275 standard. This uses two letters denoting the main alloying elements, followed by two digits denoting the rounded concentration of those elements, expressed in weight percent units.

The association between alloying elements and denoting letters is reported in Table 9. The exact composition of each alloy is defined by a specific reference standard and a final letter is used to distinguish between similar alloys.

5.2.3. Heat treatments

The mechanical properties of magnesium alloys containing aluminium or zinc can be improved by heat treatments. A solution treatment at 400 ÷ 420 °C or an artificial ageing (precipitation treatment) at 130 ÷ 200 °C are commonly performed, followed by air cooling. The solution and precipitation treatments may also be performed in sequence.

The metallurgical states of magnesium alloys are denoted by symbols, reported in Table 10, which are the same as for aluminium alloys. To denote an alloy in a specific metallurgical

state, the associated symbol may be appended to the designation of the alloy, also by interposing a hyphen.

5.2.4. Mechanical properties

The average composition of several magnesium alloys is reported in Table 11, where REE is the overall concentration of rare earth elements.

The mechanical properties of the alloys in selected metallurgical states were collected from the datasheets provided by Magnesium Elektron Ltd., Superform Products Ltd. and Kenwalt Die Casting Co. Yield strength (R_y), ultimate strength (R), elongation (e), Brinell hardness (BH) and fatigue resistance in notched ($R_{f,n}$) and unnotched ($R_{f,u}$) modes are reported in Table 12 and plotted in Figure 21, Figure 22, Figure 23 and Figure 24. The oblique line in Figure 21 ideally represents materials with no strain hardening, while that in Figure 24 ideally represents notch insensitive materials.

Typical values are reported, except where specification minima are noted. Tensile properties were obtained with separately cast test bars. For the fatigue performance, datasheets report the stress corresponding to a lifetime of $5 \cdot 10^7$ cycles in rotating bending type tests; notch was semicircular with a 1.2 mm radius and a stress concentration factor of about 2.

A	aluminium	N	nickel
B	bismuth	P	lead
C	copper	Q	silver
D	cadmium	R	chromium
E	rare earths	S	silicon
F	iron	T	tin
H	thorium	V	gadolinium
J	strontium	W	yttrium
K	zirconium	X	calcium
L	lithium	Y	antimony
M	manganese	Z	zinc

Table 9. Alloying elements and denoting letters.

F	as-fabricated
O	annealed or recrystallized (wrought product)
H1	strain hardened
H2	strain hardened and partially annealed
H3	strain hardened and stabilized
W	solution heat treated to produce unstable temper
T2	annealed (cast product)
T3	solution heat treated and cold worked
T4	solution heat treated
T5	artificially aged
T6	solution heat treated and artificially aged
T7	solution heat treated and stabilized
T8	solution heat treated, cold worked and artificially aged
T9	solution heat treated, artificially aged and cold worked
T10	artificially aged and cold worked

Table 10. Metallurgical states of magnesium alloys.

alloy	Mg	Al	Mn	Zr	REE	Zn	Ag	Y	Cu	Si
	%	%	%	%	%	%	%	%	%	%
AM50A	94.5	5.0	0.5							
AM20	97.5	2.0	0.6							
AM60B	93.5	6.0	0.5							
A8	91.2	8.0	0.3			0.5				
AZ31B	95.4	3.0	0.6			1.0				
AZ81	91.1	8.0	0.2			0.7				
AZ91D	90.2	9.0	0.3			0.5				
AZ91E	90.3	8.7	0.3			0.7				
AZ91	89.7	9.5	0.3			0.5				
AE42	93.3	4.0	0.3		2.4					
AS41B	94.6	4.0	0.4							1.0
ZA	99.4			0.6						
ZK60A	94.0			0.5		5.5				
ZRE1	93.9			0.6	3.0	2.5				
21	95.1			0.6	4.0	0.3				
RZ5	93.8			0.7	1.3	4.2				
MSR-B	94.4			0.6	2.5		2.5			
QE22	94.9			0.6	2.0		2.5			
EQ21	95.8			0.6	2.0		1.5		0.1	
WE43	92.0			0.5	3.5			4.0		
WE54	90.8			0.5	3.5			5.3		

Table 11. Average composition of several magnesium alloys.

alloy	state	R_y	R	e	BH	$R_{f,u}$	$R_{f,n}$	
		MPa	MPa	%		MPa	MPa	
AM50A	F	110 ÷ 120	200 ÷ 220	6 ÷ 10	57	70		
AM20	F	105	220	8 ÷ 12	47	70		
AM60B	F	130	220	6 ÷ 8	62	70		
A8	F	85	140 ÷ 185	2 ÷ 4	55 ÷ 70	75 ÷ 90	58 ÷ 70	*
	T4	105	260	10	55 ÷ 70	75 ÷ 90	58 ÷ 70	
AZ91E	T4	125	260	9	75		70	
	T6	170	270	4.5	75		70	
AZ91D	F	150 ÷ 160	230	3	75	70 ÷ 100		
AZ81	F	150	220	3	72	70		
AZ31B	O	140	240	10				
	T5	150 ÷ 220	255 ÷ 290	13 ÷ 16				
AZ91	F	95 ÷ 100	125 ÷ 170	2	60 ÷75	70 ÷92	58 ÷ 77	*
	T4	80	200 ÷ 215	4 ÷ 5	60 ÷75	70 ÷92	58 ÷ 77	*
	T6	120	200 ÷ 215	2	85 ÷100	70 ÷92	58 ÷ 77	*
AE42	F	140	185	8 ÷ 10	57			
AS41B	F	140	225	6	75			
ZA	F	48	170	19				
ZK60A	F	200	310	6				
ZRE1	T5	110	160	3	50 ÷60	65 ÷ 75	50 ÷ 55	
21	T6	145	248	2	70 ÷ 80	115 ÷ 120		*
RZ5	T5	148	218	4.5	55 ÷ 70	90 ÷ 115	75 ÷ 90	
MSR-B	T6	205	266	4	80 ÷ 105	100 ÷ 110	60 ÷ 70	
QE22	T6	175	240	2	80 ÷ 105	100 ÷ 110	60 ÷ 70	*
EQ21	T6	175 ÷ 185	240	2	80 ÷ 105	100 ÷ 110	60 ÷ 70	
WE43	T6	180	250	7	85 ÷ 105	85		
WE54	T6	205	280	4	80 ÷ 90	95 ÷ 100		

Table 12. Mechanical properties of several magnesium alloys.

* Specification minima are reported for yield strength, ultimate strength and elongation.

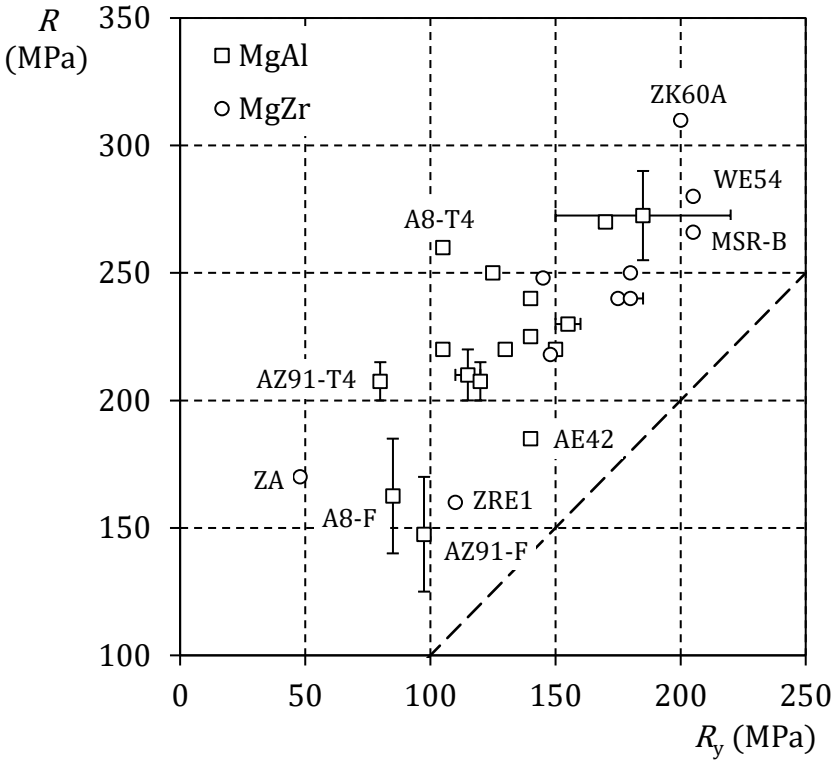

Figure 21. Yield strength and ultimate strength of several magnesium alloys.

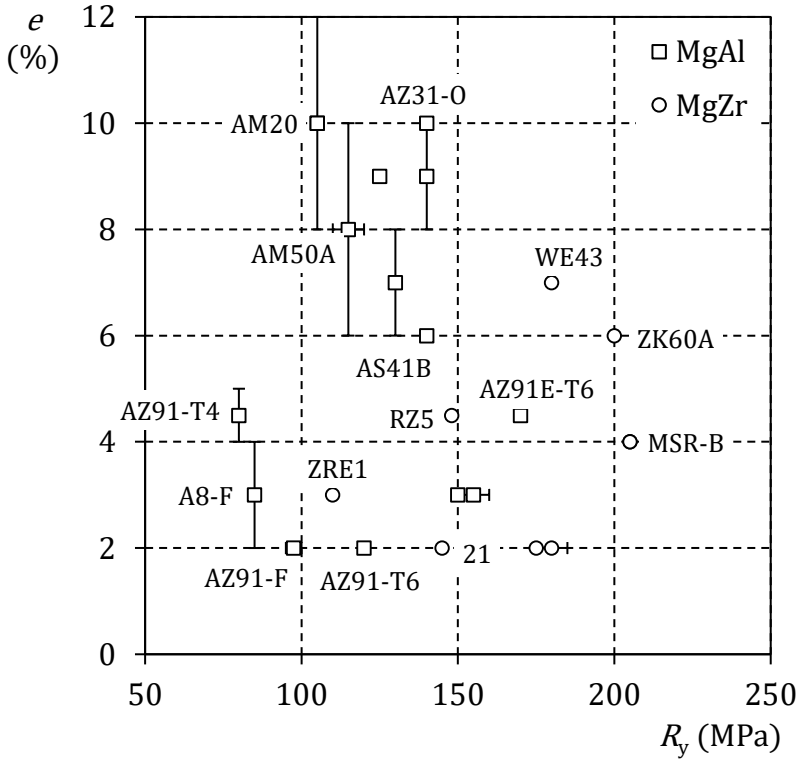

Figure 22. Yield strength and elongation of several magnesium alloys.

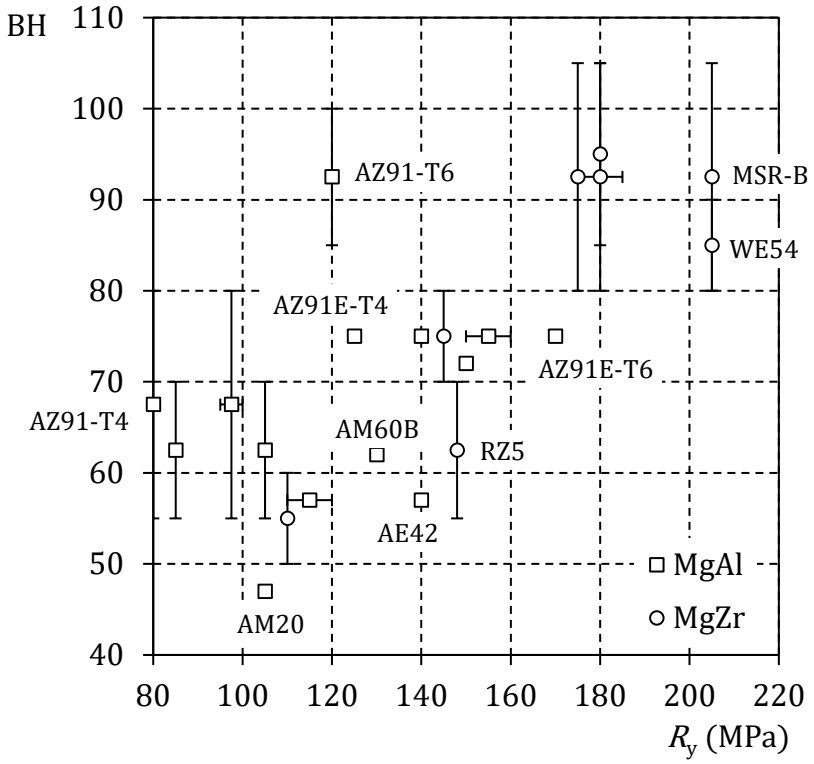

Figure 23. Yield strength and Brinell hardness of several magnesium alloys.

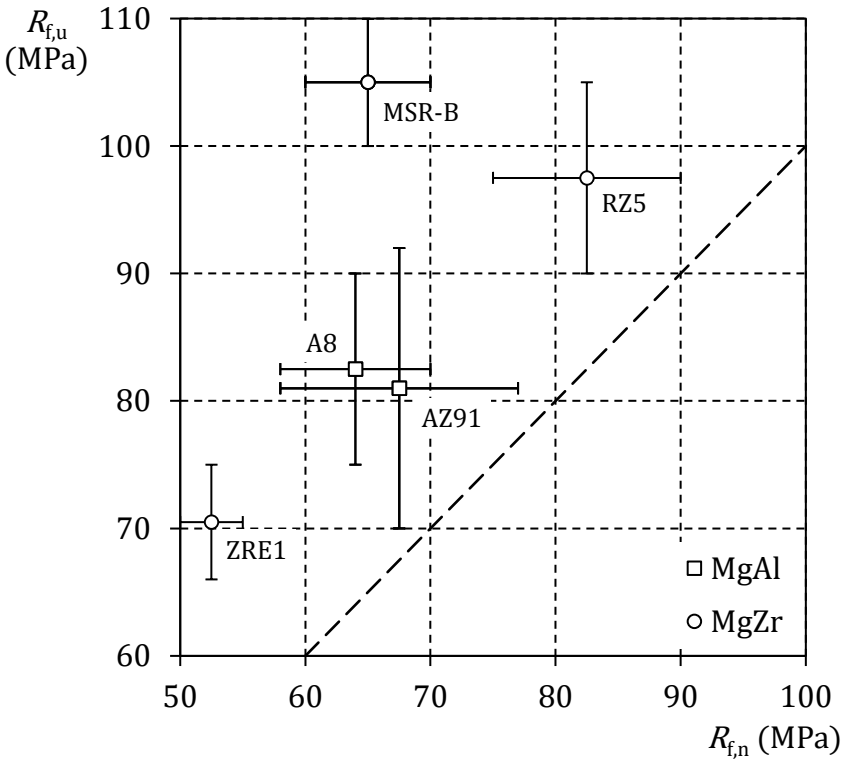

Figure 24. Fatigue resistance of some magnesium alloys in notched and unnotched modes.

6. Corrosion of magnesium

Corrosion phenomena of magnesium and its corrosion protection were reviewed by Makar and Kruger [Makar, 1993] and by Song and Atrens [Song, 1999]. The phenomena described in the following are those observed for magnesium metal and alloys in aqueous environment at 25 °C.

Pure magnesium is highly resistant to corrosion in pure water. Anyway the use of magnesium as a structural material is partially hindered by its poor corrosion resistance in presence of aggressive species in the corrosion medium and in presence of impurity elements in the metal.

Although magnesium undergoes mostly localised corrosion, the general corrosion rate is more easily quantified. It is often expressed in meters per year (mpy), which in the case of pure magnesium can be converted to daily mass loss per unit area as follows.

$$1\ \text{mpy} = 476.9\ \text{mg} \cdot \text{d}^{-1} \cdot \text{cm}^{-2}$$

6.1. Thermodynamics

Fundamental investigations on the corrosion thermodynamics of magnesium metal were reported by Pourbaix [Purbaix, 1974] and by Perrault [Perrault, 1974], the latter being more complete. The Pourbaix diagram proposed by Perrault is reported in Figure 25.

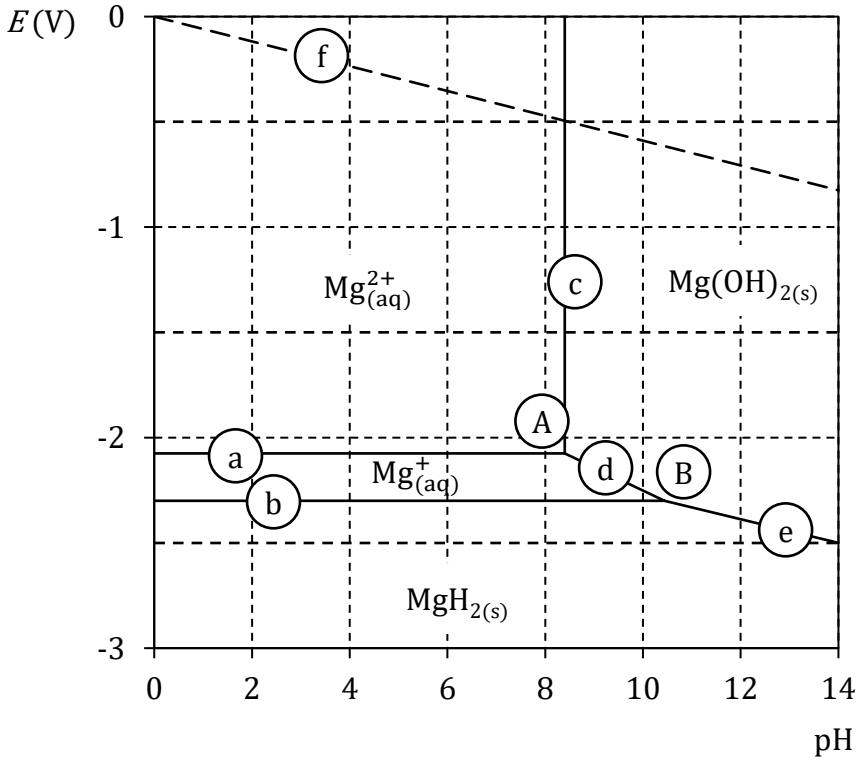

Figure 25. Pourbaix diagram of magnesium in aqueous environment.

The pH and potential of the triple points of the Pourbaix diagram and the equilibria associated to the lines are reported in Table 13. Hydrogen gas is formed only below line f.

point A	$\mathrm{pH} = 8.4 \qquad E = -2.1\ \mathrm{V}$
point B	$\mathrm{pH} = 10.4 \qquad E = -2.3\ \mathrm{V}$
line a	$\mathrm{Mg^{2+}_{(aq)} + e^- \rightleftarrows Mg^{+}_{(aq)}}$
line b	$\mathrm{Mg^{+}_{(aq)} + H_{2(g)} + e^- \rightleftarrows MgH_{2(s)}}$
line c	$\mathrm{Mg(OH)_{2(s)} \rightleftarrows Mg^{2+}_{(aq)} + 2\ OH^{-}_{(aq)}}$
line d	$\mathrm{Mg(OH)_{2(s)} + 2\ e^- \rightleftarrows Mg^{+}_{(aq)} + 2\ OH^{-}_{(aq)}}$
line e	$\mathrm{Mg(OH)_{2(s)} + H_{2(g)} + 2\ e^- \rightleftarrows MgH_{2(s)} + 2\ OH^{-}_{(aq)}}$
line f	$\mathrm{2\ H^{+}_{(aq)} + 2\ e^- \rightleftarrows H_{2(g)}}$

Table 13. Details of the Pourbaix diagram reported in Figure 25.

At the free corrosion potential the divalent Mg^{2+} ion and magnesium hydroxide are formed. Magnesium hydroxide forms a corrosion layer which is stable in alkaline solutions but soluble in neutral and acidic solutions.

By cathodic polarization the monovalent Mg^{+} ion and magnesium hydride are produced, therefore thermodynamic equilibrium does not exist for magnesium in contact with water. Neither magnesium oxide is stable when exposed to water, because it gets readily converted to magnesium hydroxide.

6.2. Mechanism

The corrosion mechanism occurring in magnesium when exposed to aqueous environment is not thoroughly understood, but shall be described in the following at the best of the current knowledge. The development of an electrochemical model for magnesium must consider that when magnesium is anodically polarized hydrogen production occurs at rates far in excess of those calculated from Faraday's law. This phenomenon is commonly described as a negative difference between theoretical and observed corrosion current and several models have been proposed to explain this discrepancy, called negative difference effect (NDE).

As described by the partial reactions below, magnesium is firstly dissolved into water in the form of monovalent Mg^{+} ion by an anodic process, while the coupled cathodic process involves the formation of hydrogen gas and the basification of the liquid phase.

$$\mathrm{Mg_{(s)} \rightarrow Mg^{+}_{(aq)} + e^-}$$

$$\mathrm{2\ H_2O_{(l)} + 2\ e^- \rightarrow H_{2(g)} + 2\ OH^{-}_{(aq)}}$$

The standard corrosion potential of the $Mg^{+}|Mg$ couple is –2.37 V vs. NHE, but in presence of magnesium oxide or hydroxide the potential rises to about –1.7 V. An applied potential major than the free corrosion potential accelerates the anodic process, while a reduced potential accelerates the cathodic process.

The unstable Mg^{+} ion is readily oxidized to Mg^{2+} ion in solution, as described by the reaction below, with further production of hydrogen gas [Przyluski, 1970].

$$2\ Mg^{+}_{(aq)} + 2\ H^{+}_{(aq)} \rightarrow 2\ Mg^{2+}_{(aq)} + H_{2(g)}$$

This second stage is a mere chemical, rather than electrochemical, process and is not directly controlled by applied potential. However this reaction is accelerated by a more rapid magnesium dissolution, which is promoted in the case of anodic polarization. Therefore both an increase and a decrease of applied potential can increase the production of hydrogen gas [Polmear, 1992] and this may explain the negative difference effect.

If magnesium is exposed to a small volume of water, the solution becomes more basic and when pH increases above 10, magnesium gets covered by a magnesium hydroxide layer as described by the reaction below. As results by X-ray diffractometry (XRD), this layer is crystalline, though slightly different from bulk magnesium hydroxide [Hanawalt, 1942].

$$Mg^{2+}_{(aq)} + 2\ OH^{-}_{(aq)} \rightarrow Mg(OH)_{2(s)}$$

Anyway the passivation given by this layer is poor and magnesium shows a low resistance to pitting. For example, in a sodium borate – boric acid buffer solution at pH 9.3, the passive current density of magnesium is as large as $1 \div 2\ mA \cdot cm^{-2}$ [Hagans, 1987], while that of iron is just $4\ \mu A \cdot cm^{-2}$.

The magnesium hydroxide layer is not passivating because it does not have the ability to repair its own flaws. When magnesium ions are dispersed through a defect in the layer, the consequent hydrolysis in the aqueous phase reduces local pH, as described by the reaction below, causing the nearby magnesium hydroxide to be dissolved [Tunold, 1977].

$$Mg^{2+}_{(aq)} + 2\ H_2O_{(l)} \rightarrow Mg(OH)_{2(s)} + 2\ H^{+}_{(aq)}$$

Consequently, the failure of the protective layer promotes further magnesium dissolution, besides activating a larger area to the cathodic reaction. By this mechanism an anodic polarization can increase both the anodic and the cathodic processes and this may explain the negative difference effect.

Figure 26 summarizes the chemical and electrochemical processes identified in the corrosion mechanism of magnesium in water as described above.

6.3. Effect of impurities

Certain trace elements, considered impurities, have a great effect on corrosion resistance of magnesium. Nickel, cobalt, iron and copper are nearly insoluble in magnesium and are found in minor phases at the grain boundaries. These phases are cathodic to the grains and may cause a dramatic increase in corrosion rate by galvanic attack when their amount is above certain tolerance limits.

The tolerable amounts of impurities in magnesium are given as follows: 1000 ppm for copper, 170 ppm for iron and 5 ppm for nickel. Cobalt is not a common impurity and its tolerance limit is not well documented. Much higher concentrations of calcium, silver and zinc are tolerated without deleterious effects [Hanawalt, 1942].

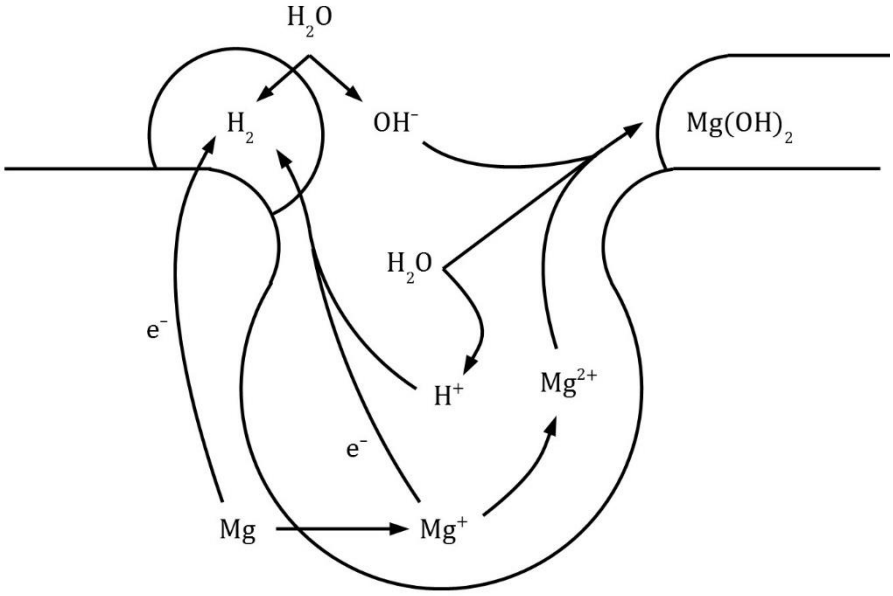

Figure 26. Corrosion mechanism of magnesium in water.

The development of high purity magnesium metal and alloys has markedly improved their corrosion resistance. For example, commercially pure magnesium (99.9% purity) gets corroded at a rate of 410 ÷ 8300 mpy in a 3% sodium chloride solution, while high purity magnesium (99.994% purity) gets dissolved at just 12 mpy [Hanawalt, 1942]. AM60B and AZ91D are examples of alloys designed to control the amount of impurities.

Since minor phases at grain boundaries are cathodic to the grains, magnesium never undergoes true intergranular corrosion, although the metal nearest to the boundaries is more readily dissolved and this gives a morphology similar to that of intergranular corrosion.

Magnesium dissolution commonly proceeds by undercutting the grains and causing them to get dispersed into the medium [Makar, 1998]. Since dispersed material is always at the free corrosion potential, an anodic polarization can promote the hydrogen gas production by increasing the amount of magnesium debris. This is another mechanism by which an anodic polarization can increase both the anodic and the cathodic processes, thus giving a third explanation of the negative difference effect.

6.4. Effect of alloying elements

A 10% of aluminium content reduces to zero the tolerable amount of iron because of the formation of $FeAl_3$ compound, which is even more active than iron itself [Emley, 1966]. Anyway aluminium generally improves the corrosion behaviour of magnesium by promoting passivation, since the aluminium rich phase gives a more protecting layer for a wide range of pH values.

Manganese reduces the effect of copper exceeding its tolerance limit [Loose, 1946] and increases the tolerance limits of both nickel [Makar, 1993] and iron. The tolerance limit of iron in magnesium-aluminium alloys is equal to 0.032 times the amount of manganese, that is 320 ppm of iron per percent point of manganese [Reichek, 1985].

Zirconium increases the tolerable amounts of iron and nickel, because these impurity elements precipitate together with zirconium before casting [Emley, 1966].

Zinc increases the tolerance limit of nickel and iron and reduces the effect of impurity elements exceeding their tolerable amounts [Loose, 1946]. Anyway zinc also promotes filiform corrosion [Albright, 1988].

6.5. Effect of dissolved species

The soluble species most aggressive to magnesium are chlorate, sulphate, nitrate, chloride, bromide and nitrite ions, the oxidizing ions being more corrosive than non-oxidizing ones.

Chloride ions are by far the most common corrosive agent. Their presence in solution alters the composition of the magnesium hydroxide layer, further compromising passivation and promoting pitting. Chlorides and oxychlorides like $MgCl_2 \cdot 6\ H_2O$ and $Mg_3(OH)_5Cl \cdot 4\ H_2O$ can be identified by XRD in the corrosion layer of magnesium exposed to a 3% sodium chloride solution [Brun, 1976].

Hydrofluoric acid attacks magnesium only at very low concentration, because it forms a protective layer of magnesium fluoride, which inhibits also other forms of corrosion. For this reason hydrofluoric acid can be used as a corrosion inhibitor [Tawil, 1987]. Sulphuric acid has a similar behavior, but is passivating only at very high concentration.

Magnesium is highly resistant to chromic acid, as well as to alkali solutions with pH above 10.5 at any temperature, even in presence of sodium chloride [Loose, 1946]. Therefore magnesium can be cleaned for removing the corrosion products with a hot solution of chromic acid or alkali salt, also at the boiling point [Froats, 1987]. Acetic acid and tartatic acid can also be used for pickling magnesium [Loose, 1946].

The concentration of oxygen in the aqueous phase is not influential to magnesium corrosion. As a consequence, crevice corrosion is not observed in magnesium.

6.6. Protective coatings

Magnesium can be protected from corrosion in atmospheric and aqueous environment by painting with an epoxy resin. Before applying the paint it is necessary to deposit a priming paint containing zinc chromate or strontium chromate. Then the metal must be dried between 180 °C and 220 °C, to ensure a good penetration into the surface defects, and cooled down to 60 °C before the immersion into the resin [Adamson, 1976].

As an alternative to the priming paint, some chemical and electrochemical coating processes can be used, that involve an acidic chromate solution and produce a magnesium oxide layer containing chromium compounds [Adamson, 1976].

Alternatively, a silicon oxide coating is produced by electrodeposition, with an improved corrosion and wear resistance [Bartak, 1991]. Physical vapour deposition (PVD) is an easier coating technique for magnesium; by RF sputtering, it is possible to deposit a compact and adherent film of amorphous silicon carbide, again with good corrosion and wear resistance [Benmalek, 1990].

Anodizing of magnesium is possible by alternating current up to 120 V in a bath of 25% ammonium bifluoride at 30 °C, thus producing a film of magnesium fluoride. This gives a good corrosion protection, but impedes any subsequent painting [Emley, 1966].

All coatings except paints are ineffective in aqueous environment because they activate a particular form of corrosion, called filiform or wormtrack, which is caused by an active corrosion cell moving across the substrate-coating interface. The same phenomenon can also be observed on certain uncoated alloys, as an effect of the partially protecting natural layer.

7. Elements of electrochemical characterization

7.1. Simulated body fluids

Biomaterials must be tested *in vitro* for assessing their interaction with a simulated physiological environment before any test *in vivo* is carried out. Simulated body fluids (SBF) are saline solutions that simulate the inorganic component of certain physiological fluids and are used for a preliminary analysis before considering the effect of the organic component. Simulated body fluids are often employed in the assessment of the electrochemical behaviour of biocompatible metals in a corrosive environment similar to that of a living tissue.

The most simple solution used as a corrosive agent is sodium chloride 0.9 wt%. This solution however does not reproduce the buffering effect of the physiological environment, that widely influences the electrochemical processes occurring at the material/fluid interface. Phosphate buffered saline (PBS) instead is used as a simple test solution that has the capability to maintain pH around 7, thanks to the equilibrium between $H_2PO_4^-$ and HPO_4^{2-} ions. A balanced solution has both a physiological pH and a physiological osmotic pressure.

More complex solutions commonly contain the inorganic ions found in blood, namely sodium, chloride, carbonate, potassium, calcium, phosphate, magnesium and sulfate ions. Both carbonate and phosphate ions have a buffering capability. However a pH indicator may be added for visually assessing any change in acidity.

The molar composition of some test solutions, published by Muller [Muller, 2006] and by Xin [Xin, 2011], are reported in Table 14 and compared to the physiological concentrations in human blood plasma. Hanks' balanced salt solution (HBSS) is a cell culture medium that also contains glucose as an energy source.

	NaCl 0.9%	PBS	Ringer	Hanks	plasma	
Na^+	153	157	39	141.7	142	mM
K^+		4.1	1.4	5.7	3.6 ÷ 5.5	mM
Mg^{2+}				0.8	1	mM
Ca^{2+}			0.4	1.7	2.1 ÷ 2.6	mM
Cl^-	153	140	40.7	145.6	95 ÷ 107	mM
HCO_3^-			0.6	4.2	27	mM
HPO_4^{2-}		11.5		0.7	0.7 ÷ 1.5	mM
SO_4^{2-}				0.8	1	mM

Table 14. Composition of several test solutions compared to human blood plasma.

7.2. Electrochemical Impedance Spectroscopy

Electrochemical Impedance Spectroscopy (EIS) investigates the electrochemical properties of a system by measuring its impedance over a wide frequency range and by developing an electrical circuit reproducing the same features with a small number of components. Finding a proper arrangement of model components requires a visual interpretation of the experimental data in the form of plots. Being able to recognize the most prominent features of an impedance plot is important to correctly develop the equivalent circuit. Several impedance plot methods that are used to report EIS measurements were reviewed by Walter [Walter, 1986].

Impedance, Z, is a complex quantity dependent on frequency, f, and characterized by two cartesian components, namely the active, a, and reactive, b, impedances. Alternatively, impedance is characterized by its polar components, namely modulus, r, and phase, θ. Their relationships are described by the following formulas.

$$Z = a + i \cdot b \qquad Z = r \cdot \exp(i \cdot \theta)$$

$$a = r \cdot \cos\theta \qquad r = \sqrt{a^2 + b^2}$$

$$b = r \cdot \sin\theta \qquad \theta = \arctan\frac{b}{a}$$

The Nyquist plot represents impedance in a complex plane having the active component as the horizontal axis and the additive inverse of reactive component as the vertical axis. The inverse is convenient because a typical impedance value having a phase between –90° and 0° will appear in the first quadrant of the plot.

The Bode plot independently represents modulus and the additive inverse of phase as functions of frequency, which is reported on a logarithmic scale. The scale of modulus is also logarithmic, while the scale of phase is linear. In the following the Bode plot of modulus and phase shall be split into two individual plots for an easier reading.

7.2.1. Simple circuits

A simple resistor with resistance R has zero reactive impedance and phase and has modulus constant and equal to R. In Figure 27 a 3 kΩ resistor is represented in the Nyquist plot as a point on the horizontal axis, while modulus and phase are represented as constant functions of frequency.

A simple capacitor with capacitance C has zero active impedance and a –90° phase. Modulus is the additive inverse of reactive impedance, which is calculated by the formulas below, where ω is pulsation. In Figure 28 a 400 nF capacitor is represented in the Nyquist plot as a line superimposing the vertical axis and in the Bode plots as straight lines. The slope of modulus in the Bode plot is always –1 for capacitors.

$$-b = \frac{1}{\omega \cdot C} \qquad \omega = 2 \cdot \pi \cdot f$$

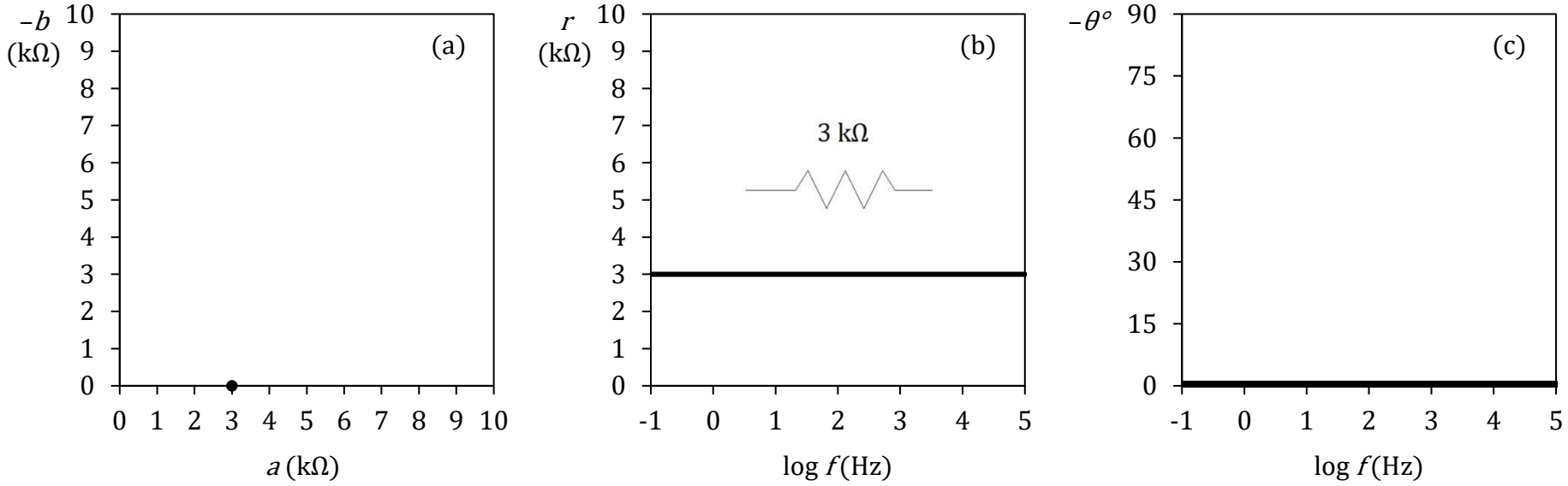

Figure 27. Nyquist plot (a), scheme (b), modulus (b) and phase (c) of a 3 kΩ resistor.

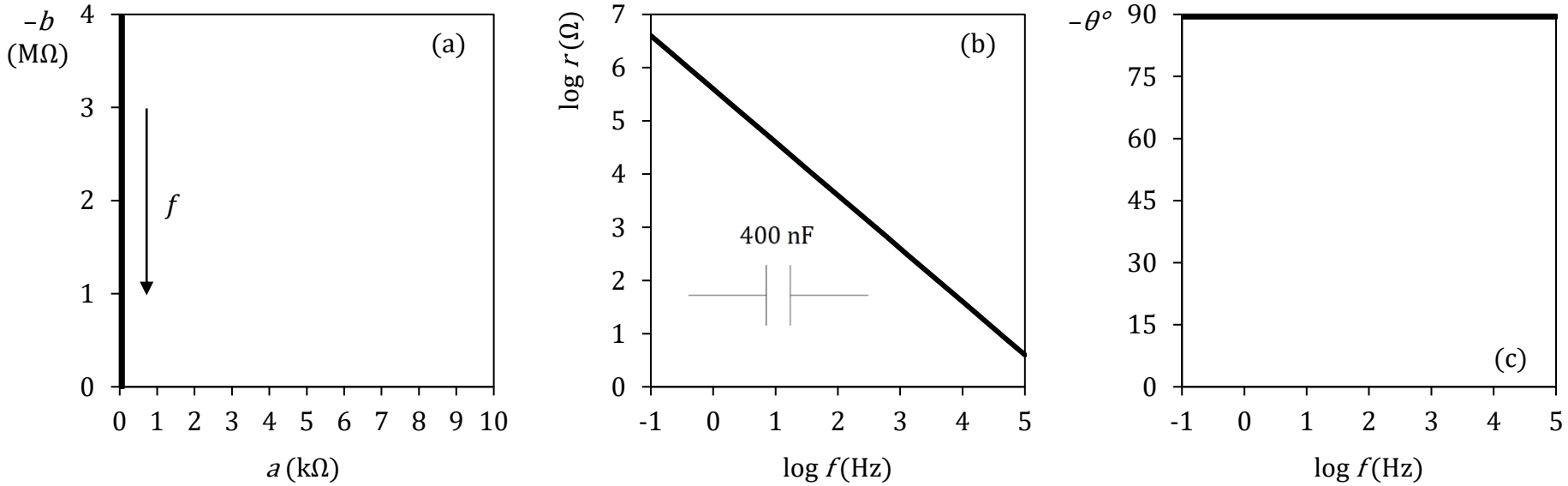

Figure 28. Nyquist plot (a), Bode plots (b, c) and scheme (b) of a 400 nF capacitor.

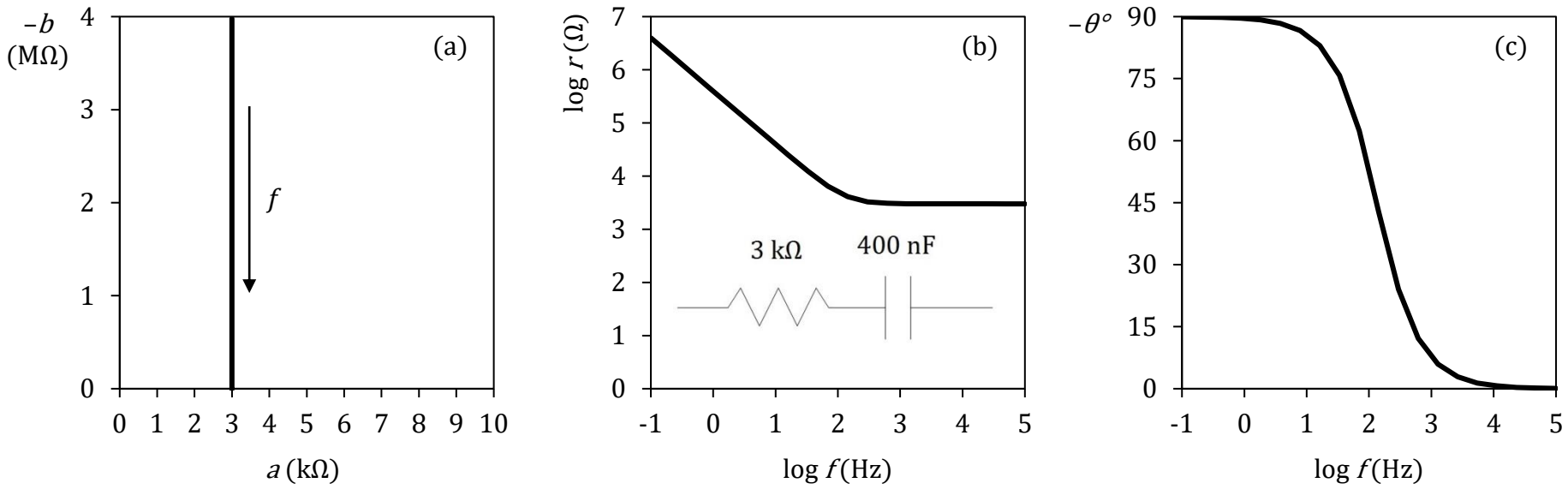

Figure 29. Nyquist plot (a), Bode plots (b, c) and scheme (b) of a 3 kΩ resistor in series with a 400 nF capacitor.

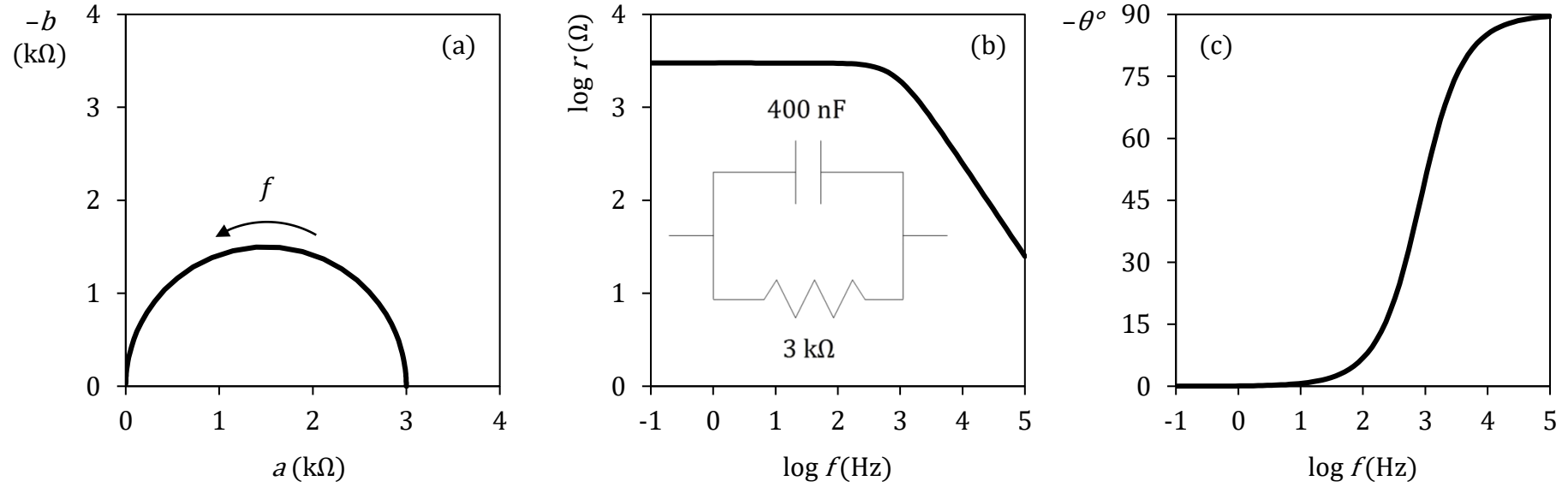

Figure 30. Nyquist plot (a), Bode plots (b, c) and scheme (b) of a 3 kΩ resistor in parallel with a 400 nF capacitor.

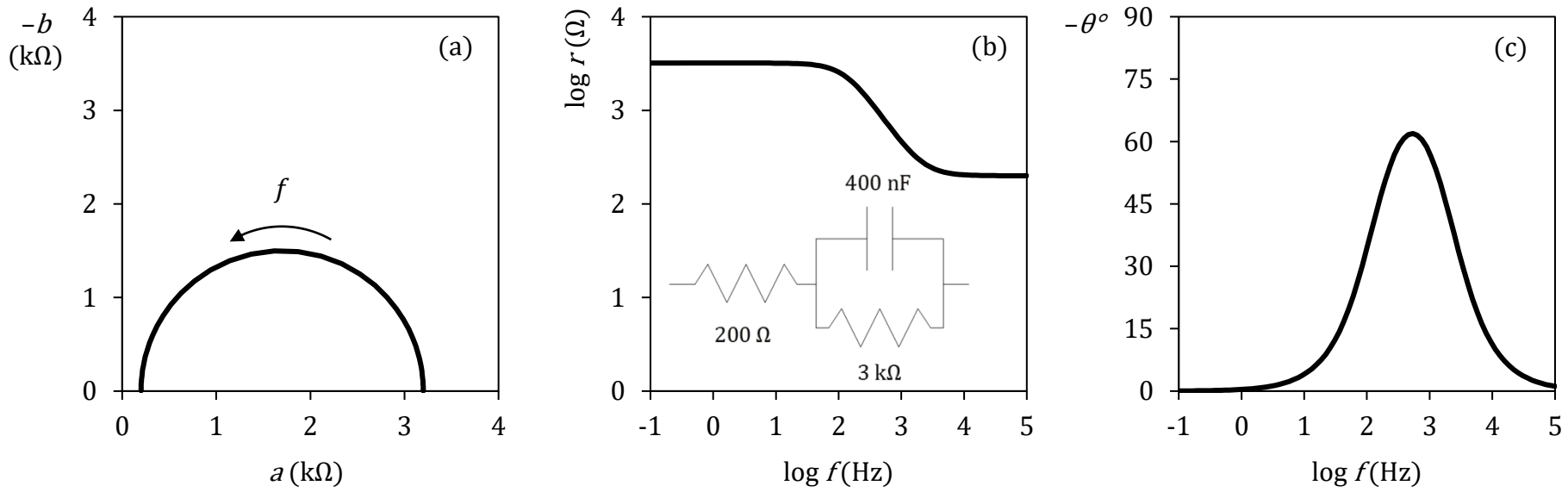

Figure 31. Nyquist plot (a), Bode plots (b, c) and scheme (b) of a circuit representing a metal in contact with an electrolyte solution.

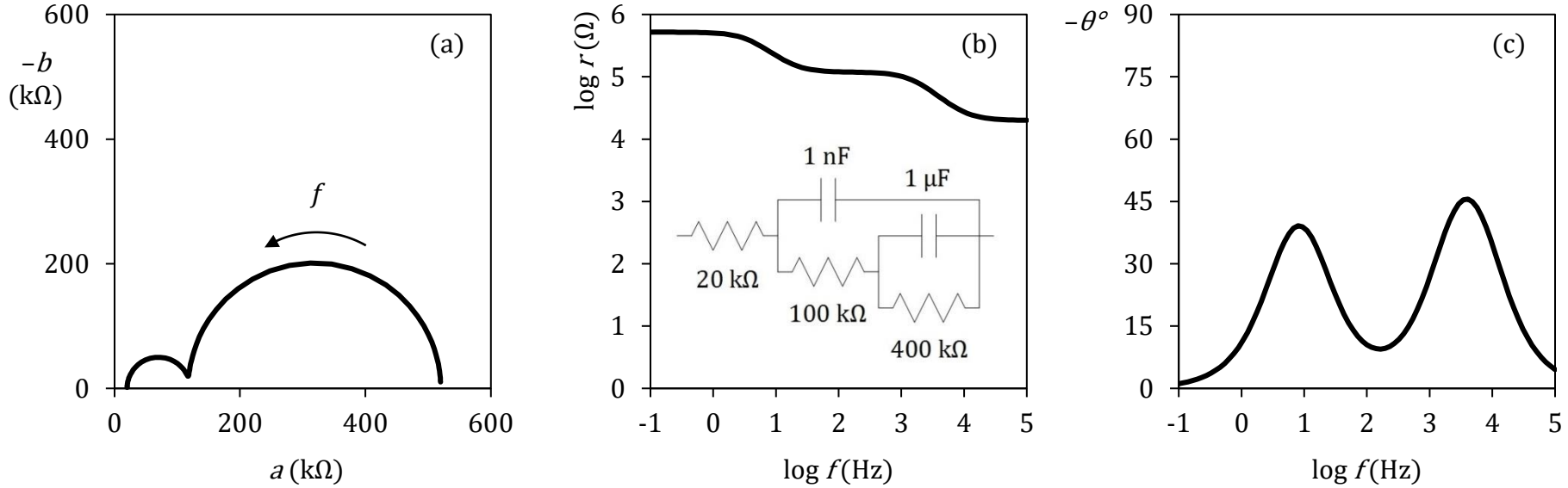

Figure 32. Nyquist plot (a), Bode plots (b, c) and scheme (b) of a circuit representing a coated metal in contact with an electrolyte solution.

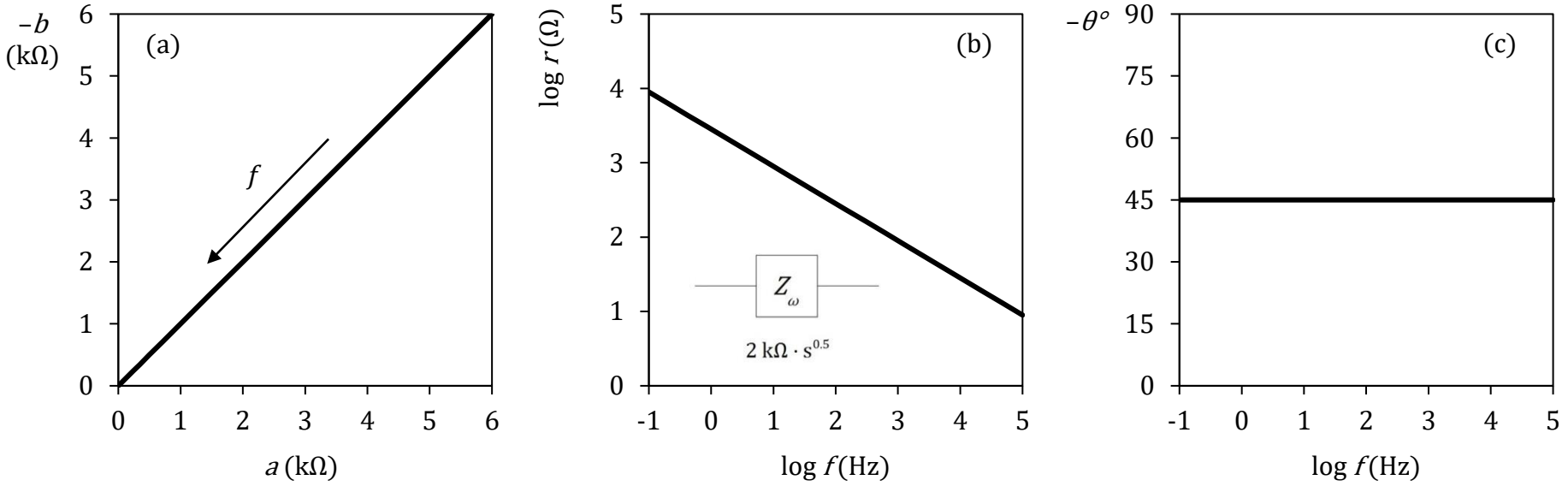

Figure 33. Nyquist plot (a), Bode plots (b, c) and scheme (b) of a Warburg element with a 2 kΩ · $s^{0.5}$ coefficient.

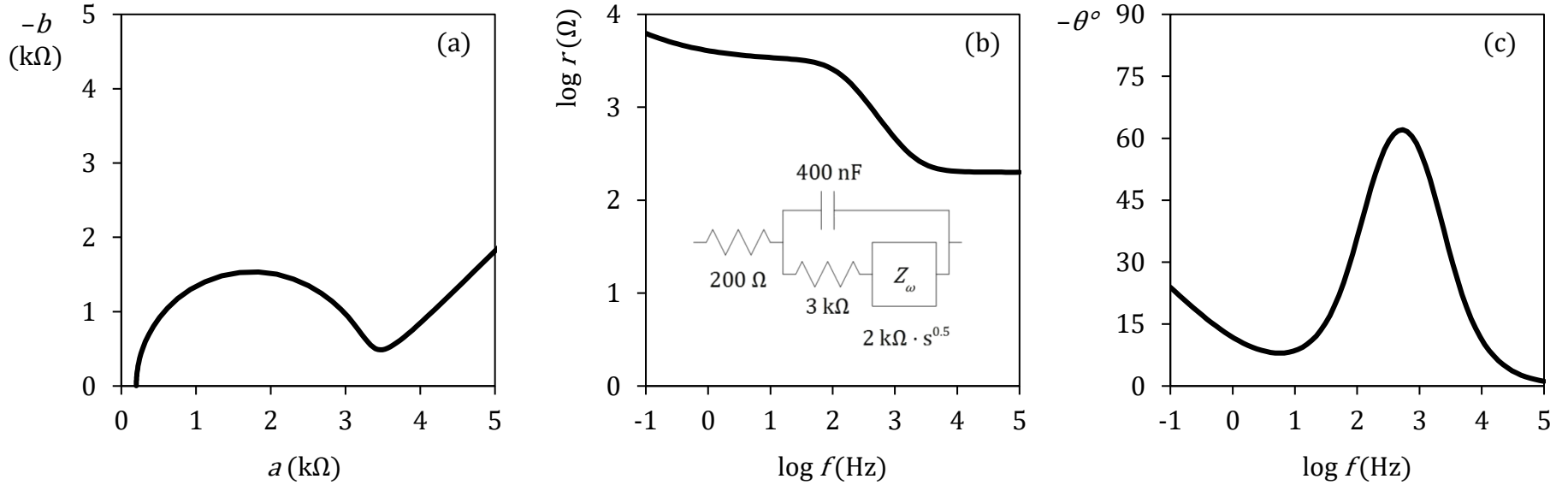

Figure 34. Nyquist plot (a), Bode plots (b, c) and scheme (b) of a circuit representing a porous metal in contact with an electrolyte solution.

The impedance of a resistor in series with a capacitor is the complex sum of their individual impedances. In Figure 29 a 3 kΩ resistor in series with a 400 nF capacitor is represented in the Nyquist plot as a vertical line and in the Bode plots with a bent line for modulus and a descending sigmoid for phase.

Phase equals –45° when active and reactive impedances are equal, at the frequency where the modulus plot shows a bend. This frequency, $f_{45°}$, is calculated by the following formulas, where τ is the time constant.

$$f_{45°} = \frac{1}{2 \cdot \pi \cdot \tau} \qquad \tau = R \cdot C$$

The impedance of a resistor in parallel with a capacitor is the reciprocal of the sum of the reciprocals of their individual impedances. In Figure 30 a 3 kΩ resistor in parallel with a 400 nF capacitor is represented in the Nyquist plot as a semicircle of diameter R, centered on the horizontal axis and passing through the origin. In the Bode plots it is represented as a bent line for modulus and an ascending sigmoid for phase. Reactive impedance is maximum when phase is –45°, which occurs at the frequency $f_{45°}$.

7.2.2. Metal in contact with an electrolyte solution

A simple electrochemical system is formed by a metal in contact with an electrolyte solution. This system is described by the equivalent circuit shown in Figure 35, where R_0 is the resistance of metal and solution, R_t is the charge transfer resistance of their interface and C_d is the double layer capacitance of the interface. Active and reactive impedances of this circuit can be calculated by the following formulas.

$$a = R_0 + \frac{R_t}{1 + \omega^2 \cdot R_t^2 \cdot C_d^2} \qquad -b = \frac{\omega \cdot R_t^2 \cdot C_d}{1 + \omega^2 \cdot R_t^2 \cdot C_d^2}$$

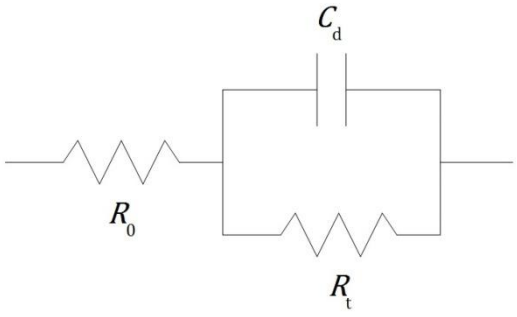

Figure 35. Circuit representing a metal in contact with an electrolyte solution.

In Figure 31 the system is represented in the Nyquist plot as a semicircle of diameter R_t centered on the horizontal axis. In the Bode plots the modulus function shows two plateaus and a central descending portion, whereas phase shows a peak.

7.2.3. Coated metal in contact with an electrolyte solution

A more complex electrochemical system is formed by a coated metal in contact with an electrolyte solution; the coating is supposed to be non conductive, though permitting the permeation of dissolved species through its pores or defects.

This system my be described by the equivalent circuit show in Figure 36, where R_0, R_t and C_d have the same meaning as above, while R_pf is the resistance of the pores and C_pf is the capacitance of the porous film. Active and reactive impedances of this circuit can be calculated by the following formulas.

$$a = R_0 + \frac{R_\mathrm{pf} + R_\mathrm{t} + \omega^2 \cdot R_\mathrm{pf} \cdot {R_\mathrm{t}}^2 \cdot {C_\mathrm{d}}^2}{\left(1 - \omega^2 \cdot R_\mathrm{pf} \cdot R_\mathrm{t} \cdot C_\mathrm{pf} \cdot C_\mathrm{d}\right)^2 + \omega^2 \cdot \left(R_\mathrm{pf} \cdot C_\mathrm{pf} + R_\mathrm{t} \cdot C_\mathrm{pf} + R_\mathrm{t} \cdot C_\mathrm{d}\right)^2}$$

$$-b = \omega \cdot \frac{2 \cdot R_\mathrm{pf} \cdot R_\mathrm{t} \cdot C_\mathrm{pf} + {R_\mathrm{pf}}^2 \cdot C_\mathrm{pf} + {R_\mathrm{t}}^2 \cdot C_\mathrm{pf} + {R_\mathrm{t}}^2 \cdot C_\mathrm{d} + \omega \cdot {R_\mathrm{pf}}^2 \cdot {R_\mathrm{t}}^2 \cdot C_\mathrm{pf} \cdot {C_\mathrm{d}}^2}{\left(1 - \omega^2 \cdot R_\mathrm{pf} \cdot R_\mathrm{t} \cdot C_\mathrm{pf} \cdot C_\mathrm{d}\right)^2 + \omega^2 \cdot \left(R_\mathrm{pf} \cdot C_\mathrm{pf} + R_\mathrm{t} \cdot C_\mathrm{pf} + R_\mathrm{t} \cdot C_\mathrm{d}\right)^2}$$

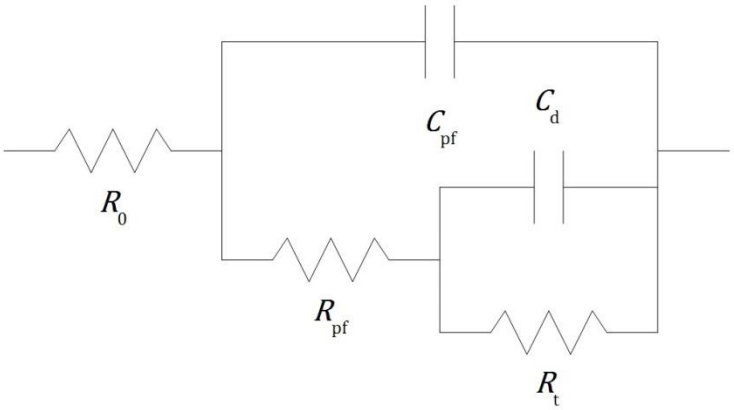

Figure 36. Circuit representing a coated metal in contact with an electrolyte solution.

In Figure 32 the system is represented in the Nyquist plot as two semicircles of diameter R_c and R_t centered on the horizontal axis and partially merged together. In the Bode plots the modulus function shows three plateaus and two descending portions, whereas phase shows two peaks. The features of these plots may overlap if the two time constants τ_pf and τ_m are not well differentiated.

$$\tau_\mathrm{pf} = R_\mathrm{pf} \cdot C_\mathrm{pf} \qquad\qquad \tau_\mathrm{m} = R_\mathrm{t} \cdot C_\mathrm{d}$$

In some cases it is necessary to modify the model of Figure 36 in order to account for the diffusion of the dissolved species through the porous coating, a phenomenon that increases the impedance at low frequency in a different manner than a capacitor does. Although diffusion phenomena are overshadowed by convection when occurring in the bulk liquid, they can be dominant at low frequencies when occurring in a porous material.

Diffusion phenomena are described by a specific circuit element, called Warburg element, which is characterized by a modulus inversely proportional to the square root of frequency

and by a phase constant and equal to –45°. Its Cartesian components are defined by the formula below, where σ is a parameter called Warburg coefficient.

$$a = -b = \frac{\sigma}{\sqrt{\omega}}$$

In Figure 33 a Warburg element with a 2 kΩ · $s^{0.5}$ coefficient is represented as straight lines in the Nyquist plot and in the Bode plots. The slope of modulus in the Bode plot is always -0.5 for Warburg elements.

The Warburg element should be included in the circuit in series with the charge transfer resistor, as shown in Figure 37. Anyway the impedance components of this kind of model tend to be exceedingly complicated to be reasonably expressed in a formula.

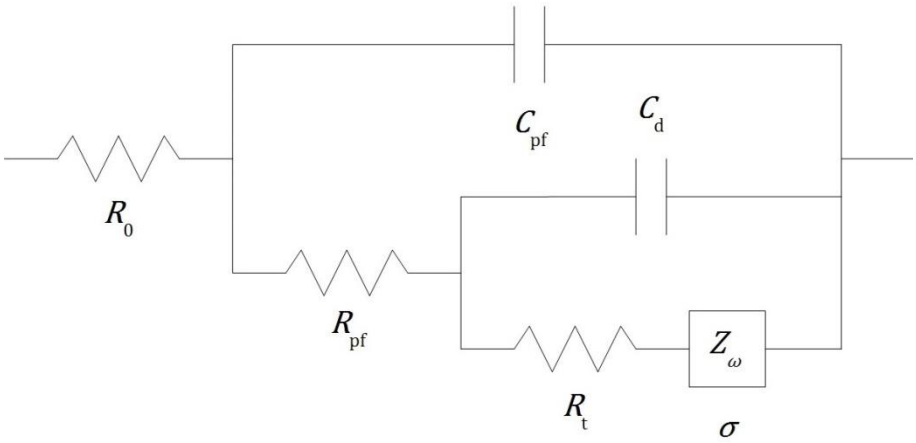

Figure 37. Warburg element implemented in the model of Figure 36.

7.2.4. Porous metal in contact with an electrolyte solution

The Warburg element can also be implemented in the model of a metal in contact with an electrolyte solution, as shown in Figure 38. The circuit obtained may represent an uncoated porous metal or a metal with a porous coating where the two time constants are not differentiated. Active and reactive impedances of this circuit can be calculated by the following formulas.

$$a = R_0 + \frac{R_t + \sigma \cdot \omega^{-0.5}}{(1 + \omega \cdot R_t \cdot C_d)^2 + (\omega \cdot R_t \cdot C_d + \sigma \cdot \omega^{0.5} \cdot C_d)^2}$$

$$-b = \frac{\omega \cdot {R_t}^2 \cdot C_d + 2 \cdot \sigma \cdot \omega^{0.5} \cdot R_t \cdot C_d + 2 \cdot \sigma^2 \cdot C_d + \sigma \cdot \omega^{-0.5}}{(1 + \omega \cdot R_t \cdot C_d)^2 + (\omega \cdot R_t \cdot C_d + \sigma \cdot \omega^{0.5} \cdot C_d)^2}$$

In Figure 34 the system is represented in the Nyquist plot as a circular arc of diameter R_t centered on the horizontal axis and joint to a straight line with a 45° slope. In the Bode plots the modulus function shows two plateaus and two descending portions, while phase shows a peak; a plateau at –45° would appear at lower frequencies.

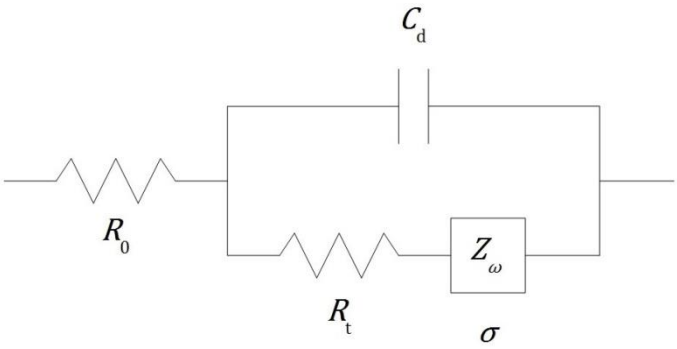

Figure 38. Warburg element implemented in the model of Figure 35.

7.2.5. Constant phase element

For representing non-ideal diffusion phenomena, a generalization of the Warburg element is defined. This is called constant phase element (CPE) and is characterized by a modulus inversely proportional to a power of frequency and by a constant phase, as described by the following formulas.

$$a = \frac{\sigma}{\omega^n} \cdot \cos\theta \qquad b = \frac{\sigma}{\omega^n} \cdot \sin\theta \qquad -\theta = \frac{\pi}{2} \cdot n$$

The unit of measure of σ is $\Omega \cdot \mathrm{Hz}^n$. For $n = 0$, the CPE is equivalent to a resistor of resistance σ. For $n = 1$, it is equivalent to a capacitor of capacitance $1/\sigma$. For $n = 0.5$, it is a Warburg element.

Part III

Experimental details

8. Method

8.1. Sintering apparatus

The sintering experiments were performed in a pre-existing apparatus, which was modified for the purpose of this work. The main changes concerned the sensors and the measurement and control system. A PC was programmed to acquire and record all the measured quantities and to control some of the operations of the system.

8.1.1. Process chamber

The process is performed in a cylindrical vacuum chamber, provided by VCS S.r.l. The chamber is made in stainless steel, with an internal diameter of 267 mm and an internal height of 220 mm.

The chamber has a round window in the front, with a diameter of 153 mm; this is fixed by twenty screws and sealed by a copper gasket. The chamber also has two CF16 flanges on one side, which are used for the gas inlet and the vacuum pumping. Moreover the chamber is equipped with two bellows which permit to press the material in between. Their distance equals 101 mm at rest and can be reduced down to 98 mm by using a press.

8.1.2. Cooling system

The walls of the process chamber are designed to permit an effective cooling by means of a water circulation system. The chiller unit is a model KRA200A52405 apparatus provided by Kelvin S.r.l. The refrigeration is performed by air ventilation and it is set to maintain the water temperature at the outlet of the chiller between 23 °C and 27 °C.

8.1.3. Press

The press operates on the vertical axis by two pistons, that are coupled with the bellows of the process chamber. The lower piston is the one designed for pressing, while the upper piston is to be used for positioning only. The pistons are coupled with two double-acting cylinders connected to an oleodynamic system which was provided by B-Fluid S.r.l. A scheme of the system is reported in Figure 39.

The oleodynamic system is basically composed by an oil tank, a pump, a pressure regulator and two directional four-way valves. For safety reasons, the press is operated independently from the PC and the operator controls the directional valves by means of a control panel.

The pump operates up to 260 bar and the pressure is controlled by the pressure regulator, which is adjusted manually. The pressure is measured by analog manometers both upstream and downstream from the regulator. These are model 213.53 Bourdon tube pressure gauges provided by WIKA Italia S.r.l. & C. sas. The upstream manometer has a range of 400 bar and divisions of 20 bar. The downstream manometer has a range of 40 bar and divisions of 2 bar.

The system is connected to the cylinders via check valves which open at a minimum pressure of 10 bar. Since the cylinders have an internal diameter of 115 mm, the applied force is between 10 kN and 270 kN.

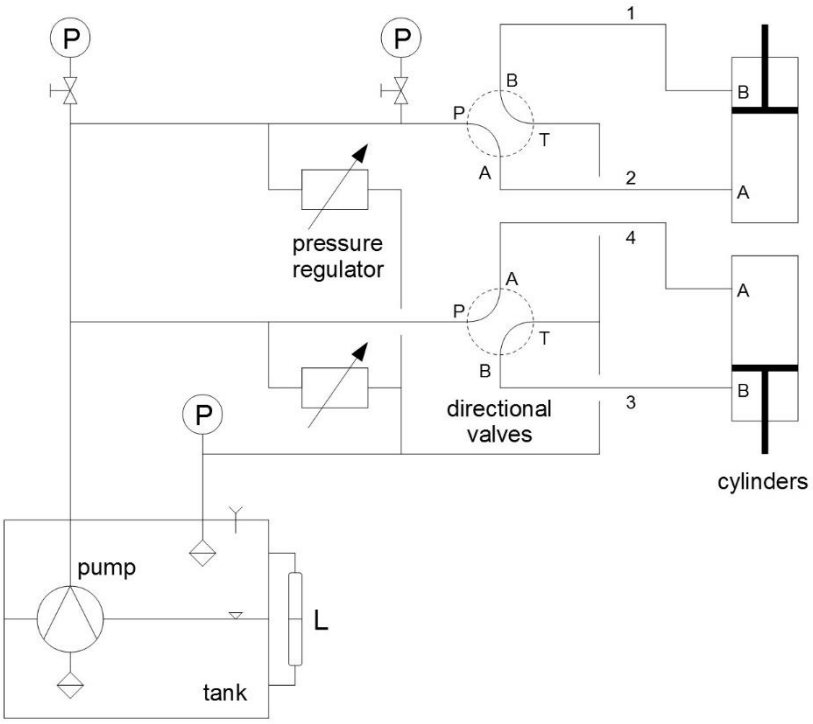

Figure 39. Essential scheme of the oleodynamic system.

8.1.4. Measurement of displacement

The lower piston of the press is equipped with an external shaft that couples with a displacement sensor. This is a model D22-5S linear variable displacement transformer (LVDT) provided by Shinko Denshi Co. Ltd. The sensor is powered by a 12 V direct voltage and returns an analog output between –4.1 V and +5.7 V. The transduction function is the following, where V denotes the output and z denotes the vertical displacement, measured from the upmost position of the piston upwards.

$$z = -4.70\ \text{mm} + 1.47\ \frac{\text{mm}}{\text{V}} \cdot V$$

The calibration was carried out by the author between –2.7 mm and +0.8 mm. The maximum deviation from linearity was equal to 0.03 mm, corresponding to a 0.9% of linearity error.

8.1.5. Vacuum system

The apparatus is designed to operate in vacuum and the scheme of the vacuum system is reported in Figure 40.

The system is evacuated by a vacuum rotary vane pump. This is a model A652-01-884 equipment, that is a type RV3 pump provided by Edwards S.p.A. It has a maximum flow rate of 3.7 $m^3 \cdot h^{-1}$, a backflow rate of 10^{-5} mbar $\cdot$ L $\cdot$ s^{-1} and a theoretical pressure limit of 0.001 mbar, although the actual pressure at regime is not smaller than 1 mbar. The apparatus is also equipped with a manual vent valve for breaking the vacuum.

The pressure is measured by an active Pirani gauge, which is a model APG100-XM sensor provided by Edwards S.p.A. The sensor is located on the pump line, in proximity of the chamber. It can measure pressures between 0.001 mbar and 1000 mbar, with an uncertainty of 15%

below 100 mbar. The sensor is powered by a 24 V direct voltage and returns an analog signal between 1.9 V and 9.1 V. The transduction function is the following, where p denotes the pressure in millibar and V the output in Volt.

$$p = 10^{V-6}$$

The chamber is also connected to an argon cylinder via a solenoid valve which is controlled by the PC. A pressure regulator at the outlet of the cylinder sets the pressure at 1 bar. High purity argon is used for purging the chamber prior to the sintering process. A purging carried out for 5 min above 2 mbar (at the outlet of the chamber) is considered sufficient for removing any residual air.

The pressure sensor is calibrated for dry air, but the measurement is influenced by the gas composition. In the case of pure argon at pressures below 10 mbar, the real pressure may be computed multiplying the nominal value by the factor 1.7. Anyway, due to the lack of knowledge about the composition of the gaseous phase, this correction was not eventually implemented in the acquisition software.

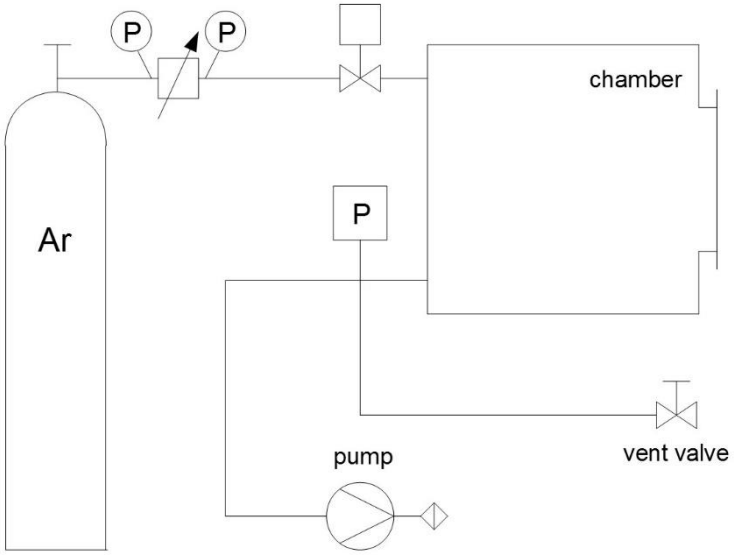

Figure 40. Scheme of the vacuum system.

8.1.6. Main current generator

The main current generator is a model GIS1000/2KA-20KVA-1 instrument provided by Zenone Elettronica S.r.l. It is capable of producing alternate currents between 100 A_{rms} and 2000 A_{rms} at 50 Hz, with a maximum voltage of 10 V_{rms}.

The generator is connected to the PC by the RS-232 serial interface for the acquisition of the current, voltage and power factor measures. The current measurement has a resolution of 0.5 A_{rms}, a range of 2200 A_{rms} and an uncertainty of 0.3% at full range. The voltage measurement has a resolution of 2.5 mV_{rms}, a range of 11 V_{rms} and an uncertainty of 0.5% at full range. The power factor is expected to be about 1 in all cases.

Three modes of operation are available:

- the generator can be programmed to carry out a user defined cycle;
- the generator can be controlled manually;

- the generator can be controlled by an analog input, in the booster mode.

To permit the remote control of the instrument, the booster mode of the generator was implemented by connecting a signal generator (model 3324A, provided by HP Inc.), which is controlled by the PC via the IEEE-488.2 interface. The current generator produces 200 A_{rms} for a signal amplitude of 1 V_p. By this configuration the generator can only be used above 200 A_{rms} because passing through the limit of 200 A_{rms} will cause the instrument to raise a trip error.

8.1.7. Minor current generators

Two minor current generators are used in the experiments that require smaller currents and larger voltages. They are connected to the PC by the IEEE-488.2 interface for their control and the acquisition of their current and voltage measures.

One generator is a model 6032A instrument provided by HP Inc. It can produce direct currents between 0 and 50 A, with a maximum voltage of 20 V. The uncertainty of the current measurement is 0.08% of reading + 0.035 A, that of the voltage measurement is 0.08% of reading + 0.02 V.

The other generator is a model PS 8080-120 2U instrument provided by EA-Elektro-Automatik GmbH. It can produce direct currents between 0 and 120 A, with a maximum voltage of 80 V. The uncertainty of the current and voltage measurements is 0.2% of reading.

8.1.8. Power connections

The main generator is used during the sintering processes performed by means of a graphite die. In this case the generator is connected by copper bars and braids to the upper piston of the press and to the lower bellow of the chamber.

The two minor generators are used simultaneously in the sintering processes performed by a die that requires independent internal and external heating. In this case the 80 V / 120 A generator is connected to the bellows of the process chamber, in order to inject current into the die, while the 20 V / 50 A generator is connected directly to the heating filament of the die to provide the external heating.

This secondary line is made by two power wires and by a custom electrical feedthrough, connected by means of screw down terminals. The selected terminals, provided by RS Components S.p.A. (code 703-3858), are made in nickel plated brass, with screws in galvanized steel, and they can operate up to 350 °C with a current of 57 A.

8.1.9. Thermocouples

The temperatures inside the process chamber are measured by one to six thermocouples. Chromel-alumel (type K) thermocouples are used for their high operating temperature. Two thermocouple models provided by RS Components S.p.A. are used for different temperature intervals. The code 621-2158 thermocouples are made of two wires separately insulated with a PTFE sheath and can operate below 250 °C. The code 787-7835 thermocouples instead have a stainless steel sheath and a magnesium oxide insulation; this way they can operate up to 1100 °C; the probe has a diameter of 1 mm and a length of 50 cm.

The inverse polynomial coefficients reported in Table 15 are provided by the National Institute of Standards and Technology (NIST). They are defined for an output expressed in millivolt and permit to calculate the differential temperature in Celsius degrees.

polynomial degree	inverse coefficient 0 ÷ 500 °C 0 ÷ 21 mV	inverse coefficient 500 ÷ 1372 °C 21 ÷ 55 mV
0	0	$-1.318058 \cdot 10^{+2}$
1	$+2.508355 \cdot 10^{+1}$	$+4.830222 \cdot 10^{+1}$
2	$+7.860106 \cdot 10^{-2}$	$-1.646031 \cdot 10^{0}$
3	$-2.503131 \cdot 10^{-1}$	$+5.464731 \cdot 10^{-2}$
4	$+8.315270 \cdot 10^{-2}$	$-9.650715 \cdot 10^{-4}$
5	$-1.228034 \cdot 10^{-2}$	$8.802193 \cdot 10^{-6}$
6	$+9.804036 \cdot 10^{-4}$	$-3.110810 \cdot 10^{-8}$
7	$-4.413030 \cdot 10^{-5}$	0
8	$+1.057734 \cdot 10^{-6}$	0
9	$-1.052755 \cdot 10^{-8}$	0

Table 15. Inverse coefficients of type K thermocouples.

The NIST reports the measurement uncertainty for the type K thermocouples as the greater between 2.2 °C and the 0.75% of the measure. Therefore the absolute uncertainty equals 4.5 °C for a differential temperature of 600 °C and equals 7.5 °C for a differential of 1000 °C.

8.1.10. Measurement and control system

The PC is equipped with a model PCI-6251 data acquisition board provided by National Instruments Italy S.r.l. It has eight digital input-output channels, sixteen single ended analogue inputs, a resolution of 16 bit and a sampling rate of 1.25 MS $\cdot$ s^{-1}. The accuracy of the analogue inputs is estimated as reported in Table 16.

nominal range	−0.1 ÷ +0.1	−1 ÷ +1	−10 ÷ +10	V
offset error	15	20	200	μV
gain error	150	80	60	ppm
offset temp. coeff.	9	27	210	$\mu V \cdot K^{-1}$
gain temp. coeff.	113	113	113	$ppm \cdot K^{-1}$
random noise	15	32	280	μV_{rms}

Table 16. Accuracy of the analogue inputs.

The acquisition board is connected to a model SCB-68 connector block provided by National Instruments Italy S.r.l. An integrated circuit sensor is used for measuring the reference temperature of the thermocouples. The sensor returns an analogue output, V, proportional to

the temperature, T_{ref}, in Celsius degrees and operates between 0 °C and 110 °C with an uncertainty smaller than 1 °C.

$$T_{\mathrm{ref}} = 0\ ^{\circ}\mathrm{C} + 0.1\ \frac{^{\circ}\mathrm{C}}{\mathrm{mV}} \cdot V$$

The output of the thermocouples is measured with 100 samples per acquisition to reduce the random noise. The uncertainty is smaller than 90 μV, corresponding to less than 2.3 °C for differential temperatures up to 1000 °C. Therefore the overall temperature uncertainty is estimated as 8 °C at a measured temperature of 600 °C and as 11 °C at 1000 °C.

In the case of the pressure and displacement measurements, the uncertainty associated to the measurement of the sensor outputs is negligible respect to that of the direct measurements.

The PC also operates the valve that controls the argon inlet to the process chamber. A digital output channel of the acquisition board is used to operate a model PRMA 1A reed relay provided by Relay Specialties Inc. and this relay operates on the 24 V power line to the valve.

A scheme featuring the sensors and the valve connected to the acquisition board is reported in Figure 41.

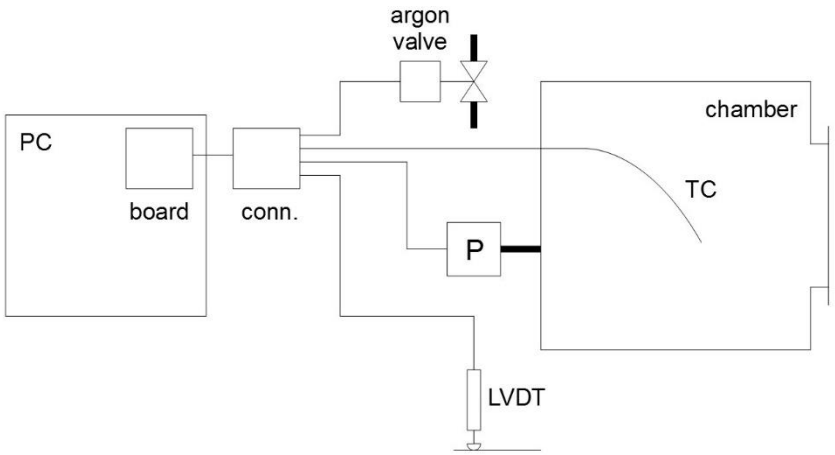

Figure 41. Partial scheme of the measurement and control system.

8.1.11. Software

A specific software, named SparkPlasmaSintering, was developed in the C# programming language and was implemented to monitor and to control the apparatus. Figure 42 shows a screenshot of the software, that was recorded during the experimental validation of the thermal model described in this thesis.

All the analogue and digital measurements are carried out together, with a period defined by the operator. Derived quantities are then calculated at each acquisition cycle. Both the measured and the calculated values are reported in a panel and plotted on a chart, with distinct layout options that may be set by the operator. The measurements may also be individually deactivated by the operator to permit diagnostic and calibration activities.

The software also permits to control the argon inlet valve and the current generated by the instruments. The generators can be commanded to perform current steps as well as current ramps. The ramps shall be linear respect to the square of current, that is linear respect to the

power in the case of a constant resistance. For safety reasons, none of the control functions is programmable.

The acquired measures are permanently recorded as soon as the acquisition cycle is completed, together with the acquisition time and the controlled parameters. The derived quantities are not recorded to avoid redundancy. The data are optionally recorded in two distinct files: a raw data file and a spreadsheet. Both the files are automatically saved in a dedicated directory and they have a name composed by the date and time of the process start.

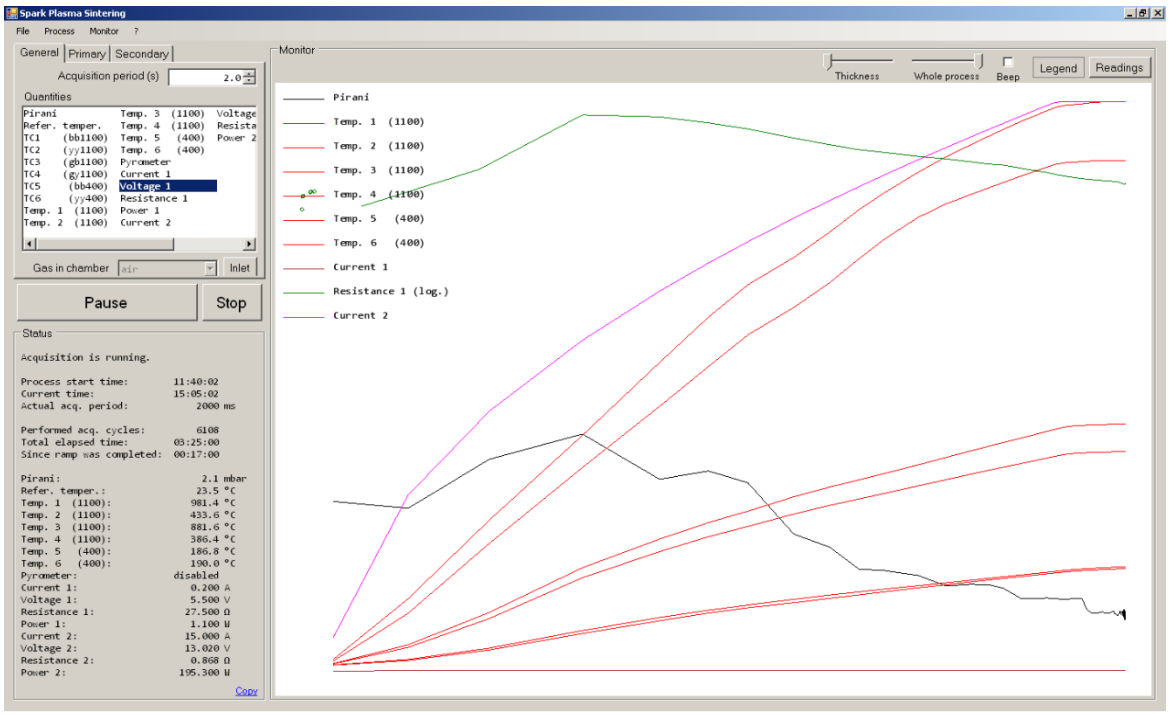

Figure 42. Screenshot of the developed software that controls the sintering apparatus.

8.1.12. File formats

The raw data file has a txt extension and is intended for a subsequent automatic elaboration. It contains the user name given by the operating system in the first line, the date and time of the process start in the second line and the title of the recorded quantities in the third line, followed by the data. The data comprise the machine time in 10^{-7} s as integer numbers, the output voltages of the sensors in Volt as double precision floating point numbers, the digitally acquired quantities as returned by the instruments and the controlled parameters as integer or double precision floating point numbers. The data are separated by commas and the missing data are replaced by placeholder values.

The spreadsheet has a csv extension and is intended for the human elaboration. It contains the user name given by the operating system in the first line, the date and time of the process start in the second line, the title of the recorded quantities in the third line and the units of measure in the fourth line, followed by the data. The data comprise the time elapsed since the process start in seconds, the measured quantities and the controlled parameters, all being defined in their specific units of measure as integer or single precision floating point numbers. The data are separated by tabulation characters and placeholders are not used for replacing the missing data.

8.2. Selection of materials

8.2.1. Magnesium

Magnesium powder and bulk specimens were both provided by Goodfellow Cambridge Ltd. The finest available powder (code MG006021) was selected and its properties are reported in Table 17. The amount of impurities is reported in ppm by weight.

maximum particle size	50	µm
auto-ignition temperature	473	°C
purity	99.8	%
max. aluminum	500	ppm
max. iron	400	ppm
max. manganese	300	ppm
max. zinc	100	ppm
max. carbon	60	ppm
max. chlorine	30	ppm
max. copper	20	ppm

Table 17. Properties of the magnesium powder.

The apparent density of the uncompressed powder is between 0.5 and 0.7 $g \cdot cm^{-3}$. A measurement of density was performed by gas pycnometry on 3.7 g of powder and returned a bulk density of 1.800 $g \cdot cm^{-3}$. This is larger then the theoretical density of magnesium, which equals 1.738 $g \cdot cm^{-3}$, because of the impurities and the surface oxide. The amount of magnesium oxide is estimated as 3% by weight.

The bulk magnesium specimens were manufactured from a magnesium foil with a thickness of 2.0 mm (code MG000350), cut in squares with a side of (25 ± 1) mm. Some properties are reported in Table 18. The amount of impurities is reported in ppm by weight.

temper	as-rolled	
purity	99.9	%
iron	280	ppm
manganese	170	ppm
aluminum	70	ppm
silicon	50	ppm
copper	20	ppm
max. zinc	20	ppm
max. nickel	10	ppm

Table 18. Properties of the bulk magnesium.

8.2.2. Graphite

The graphite components used for sintering were provided by Atal S.r.l. Isostatically moulded graphite of the type AT101 was selected for its superior mechanical properties. Some typical properties of isostatic graphite are reported in Table 19 as given by GrafTech International Ltd. Thermal expansion coefficient refers to 20 ÷ 100 °C. Thermal conductivity, specific heat capacity and electrical resistivity refer to room temperature.

average grain size	25	µm
density	1.76	$g \cdot cm^{-3}$
Young's modulus	9.6	GPa
compressive strength	67	MPa
flexural strength	29	MPa
tensile strength	25	MPa
thermal expansion coefficient	$2.5 \cdot 10^{-6}$	K^{-1}
thermal conductivity	115	$W \cdot m^{-1} \cdot K^{-1}$
specific heat capacity	0.6	$kJ \cdot kg^{-1} \cdot K^{-1}$
electrical resistivity	$1.2 \cdot 10^{-5}$	$\Omega \cdot m$

Table 19. Properties of isostatically molded graphite.

The thermal expansion coefficient increases linearly to $3.4 \cdot 10^{-6}$ K^{-1} for temperature intervals extending to 20 ÷ 600 °C. The thermal conductivity decreases linearly down to 62 $W \cdot m^{-1} \cdot K^{-1}$ at 600 °C. The specific heat capacity increases linearly to 1.5 $kJ \cdot kg^{-1} \cdot K^{-1}$ at 430 °C and then increases to 1.6 $kJ \cdot kg^{-1} \cdot K^{-1}$ at 600 °C. The electrical resistivity linearly decreases to $9.6 \cdot 10^{-6}$ $\Omega \cdot m$ at 300 °C and then decreases down to $8.9 \cdot 10^{-6}$ $\Omega \cdot m$ at 600 °C.

Measurements of density were performed on a cylindrical specimen having a diameter of 20 mm and a height of 20 mm. The geometrical measurement returned 1.75 g · cm–3, while the gas pycnometer returned a density of 2.109 $g \cdot cm^{-3}$. Since the bulk density is 2.26 $g \cdot cm^{-3}$, the material has a total porosity of 23% and an open porosity of 17%.

Atal S.r.l. also provided some accessory products. A graphite foil with a thickness of 0.5 mm (Grafoil®) was used to improve the mechanical, thermal and electrical contact between metallic parts inside the process chamber of the sintering apparatus. A graphite based dry lubricant (Grafitene) was used to avoid the adhesion of the sintered powder to the graphite components, while a boron nitride based dry lubricant (Boroflon®) was used where no electrical conduction was needed.

8.2.3. Alumina

Alumina tubes were provided by Haldenwanger Technische Keramik GmbH Co. KG. The tubes have an internal diameter of 20 mm, and external diameter of 26 mm and a length of 35 mm. They are manufactured in compliance with DIN 40680, that sets a tolerance of 0.45 mm for the inner diameter and of 0.55 mm for the outer diameter.

The tubes are made of sintered alumina (Alsint) with a purity of 99.7% (type C 799 according to DIN EN 60672). Some properties of the sintered alumina are reported in Table 20. The flexural strength is measured in the three point configuration at 20 °C. The thermal expansion coefficient refers to 20 ÷ 700 °C. The thermal conductivity refers to 200 °C. The specific heat capacity refers to 20 ÷ 100 °C.

bulk density	3.8	$g \cdot cm^{-3}$
Young's modulus	340 ± 40	GPa
flexural strength	300	MPa
thermal expansion coefficient	$7.8 \cdot 10^{-6}$	K^{-1}
thermal conductivity	25	$W \cdot m^{-1} \cdot K^{-1}$
specific heat capacity	990	$J \cdot kg^{-1} \cdot K^{-1}$
maximum temperature	1700	°C

Table 20. Properties of Alsint 99.7 alumina.

The dependence of the thermal conductivity of alumina from temperature was studied by Kita [Kita, 2015]. Kita carried out measurements at six temperatures between 20 °C and 500 °C on a 99.99% purity alumina and defined the fitting function below, where k_c denotes the conductivity and T the absolute temperature. The same measurements were carried out by Parchovianský [Parchovianský, 2014] at temperatures up to 1000 °C, obtaining consistent results.

$$k_c = 9.4 \frac{W}{m \cdot K} + 141.4 \frac{W}{m \cdot K} \cdot \exp\left(-\frac{T}{147\ K}\right)$$

Measurements of density were carried out on a tube having an internal diameter of 20 mm, an outer diameter of 26 mm and a length of 35 mm. The geometrical measurement returned a density of 3.7 $g \cdot cm^{-3}$ and the gas pycnometer returned a density of 3.8 $g \cdot cm^{-3}$. Therefore the porosity is not measurable but is definitely smaller then 5%.

8.2.4. Heating filaments

Heating filaments were provided by RS Components S.p.A. They are nickel alloy wires with a 20% by weight of chromium and they operate up to 1150 °C with a stable resistance. The available sizes are reported in Table 21 with their unit resistance at 20 °C.

st. wire gauge	diameter	unit resistance
	mm	$\Omega \cdot m^{-1}$
14	2.032	0.33270
16	1.626	0.51883
18	1.220	0.92388
20	0.913	1.64240
22	0.711	2.71250
24	0.559	4.40060
25	0.508	5.32850
29	0.345	11.48600
35	0.213	30.30900

Table 21. Properties of the nickel-chromium wires.

The size of the filament used to heat the alumina tubes was selected to permit an efficient implementation of the 20 V / 50 A generator. The length of the coiled filament can be calculated by assuming a 4 mm pitch between two neighbouring turns. Since the surface to be covered has an area of 2859 mm^2, the filament is about 715 mm long. The resistance should be around 0.4 Ω, therefore the wire gauge 18 was selected (RS code 714-1729). The expected resistance is about 0.66 Ω and the maximum heating power is about 600 W.

For the measurement of the thermal conductivity of magnesium powder, the wire with the smallest diameter was used, in order to minimize the thermal capacity of the filament. Therefore the wire gauge 35 was selected (RS code 714-1741).

8.2.5. Thermal insulating sheet

A thermal insulating sheet of the type Superwool 607 HT was provided by Morgan Advanced Materials plc. It is a paper made of a refractory calcium and magnesium silicate, binded with organic compounds that will burn out at 150 °C. Some properties are reported in Table 22. A sheet thickness of 2 mm was selected (RS code 417-6757).

silicon oxide	60 ÷ 70	%
calcium oxide	25 ÷ 35	%
magnesium oxide	4 ÷ 7	%
nominal density	160 ÷ 208	$g \cdot cm^{-3}$
tensile strength	0.52 ÷ 0.69	MPa
operating temperature	1100	°C
loss of ignition	5 ÷ 10	%

Table 22. Properties of the thermal insulating sheet.

The thermal conductivity of the sheet can be calculated by the function below, where k_c denotes the conductivity in $W \cdot m^{-1} \cdot K^{-1}$ and T denotes the temperature in Celsius degrees. The function was obtained by second degree polynomial regression from the data given between 200 °C and 1200 °C, as shown in Figure 43. The maximum deviation from the model is 0.003 $W \cdot m^{-1} \cdot K^{-1}$.

$$k_c = 1.03 \cdot 10^{-7} \cdot T^2 + 6.3 \cdot 10^{-5} \cdot T + 2.5 \cdot 10^{-2}$$

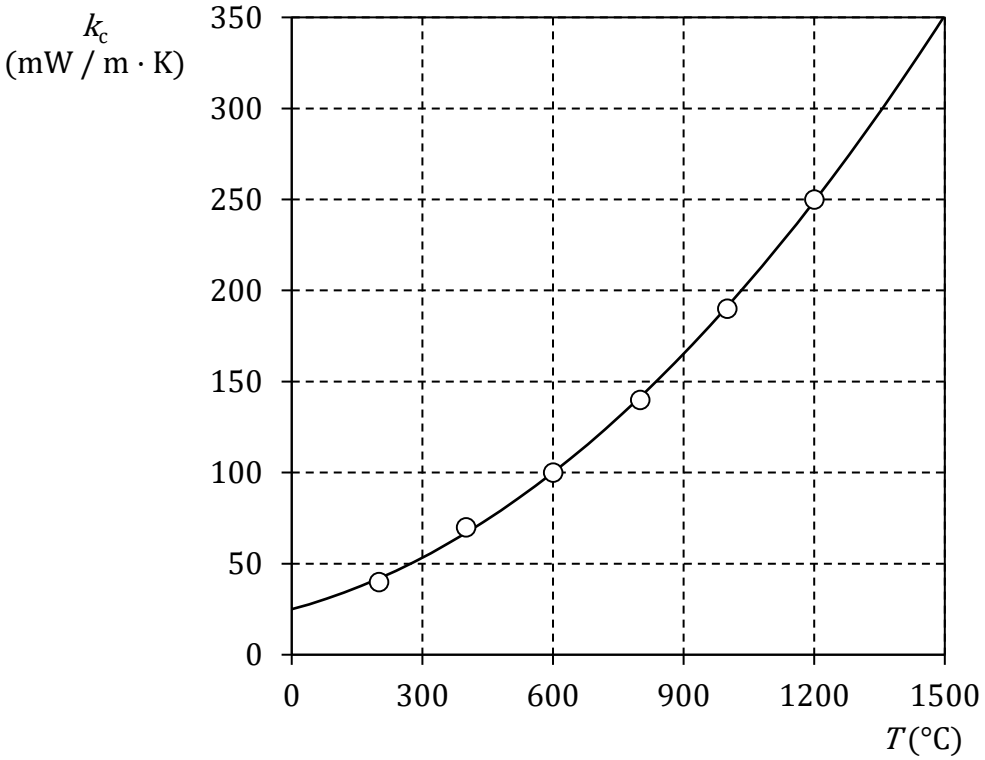

Figure 43. Thermal conductivity of the thermal insulating sheet.

8.2.6. Chemicals

All the used chemicals were provided by Sigma Aldrich S.r.l. and they are listed in Table 23.

	formula	CAS number	molar mass
			$g \cdot mol^{-1}$
urea	CH_4N_2O	57-13-6	60.06
sodium chloride	NaCl	7647-14-5	58.44
potassium chloride	KCl	7447-40-7	74.55
calcium chloride	$CaCl_2$	10043-52-4	110.98
sodium bicarbonate	$NaHCO_3$	144-55-8	84.01

Table 23. List of used chemicals.

The urea powder is crystalline, with a 99.5% purity (puriss p.a.; ACS and Ph.Eur standards); carbamide is a common synonym of urea. Sodium chloride has a 99.5% purity (puriss p.a.). Potassium chloride has a 99.9% purity (ACS standard). Calcium chloride is in the granular form, with a maximum particle size of 7 mm, and it has a 93.0% purity. Sodium bicarbonate has a 99.7% purity (ACS standard).

8.3. Synthesis procedure

8.3.1. Preparation of the powder

The preparation of the powder was performed by a Pulverisette 5 planetary mill, provided by Fritsch GmbH. The instrument is capable of operating with a couple of bowls with capacity between 80 mL and 500 mL. Grinding balls with diameters between 5 mm and 40 mm can be used, depending on the bowl size. The recommended parameters are reported in Table 24. The selected bowls and balls were made in agate to avoid the corrosion of the components and the contamination of the powders.

capacity of bowl	80	250	500	mL
volume of powder	1 ÷ 30	30 ÷ 125	80 ÷ 225	cm^3
nr. of 5 mm balls	250 ÷ 300	1200 ÷ 1300	2000 ÷ 2500	
nr. of 10 mm balls	30 ÷ 35	50 ÷ 150	100 ÷ 250	
nr. of 15 mm balls	10	45 ÷ 50	70 ÷ 100	
nr. of 20 mm balls	5	15 ÷ 20	25 ÷ 35	
nr. of 30 mm balls	–	5 ÷ 6	10	
nr. of 40 mm balls	–	–	4	

Table 24. Recommended use of the planetary mill.

The instrument can be programmed to operate at any speed between 50 rpm and 400 rpm, with a resolution of 10 rpm, for a grinding time between 1 min and 100 h. Up to 100 repetitions can be carried out, alternating with cooling periods of adjustable duration.

Firstly, the spacer powder is grinded to reduce its particle size to about the size of the magnesium powder. An 80 mL bowl made in agate is filled with 10 g of urea and with 230 agate balls having a diameter of 5 mm. The total mass of the balls is 40 g. The grinding is carried out at 120 rpm for 60 min.

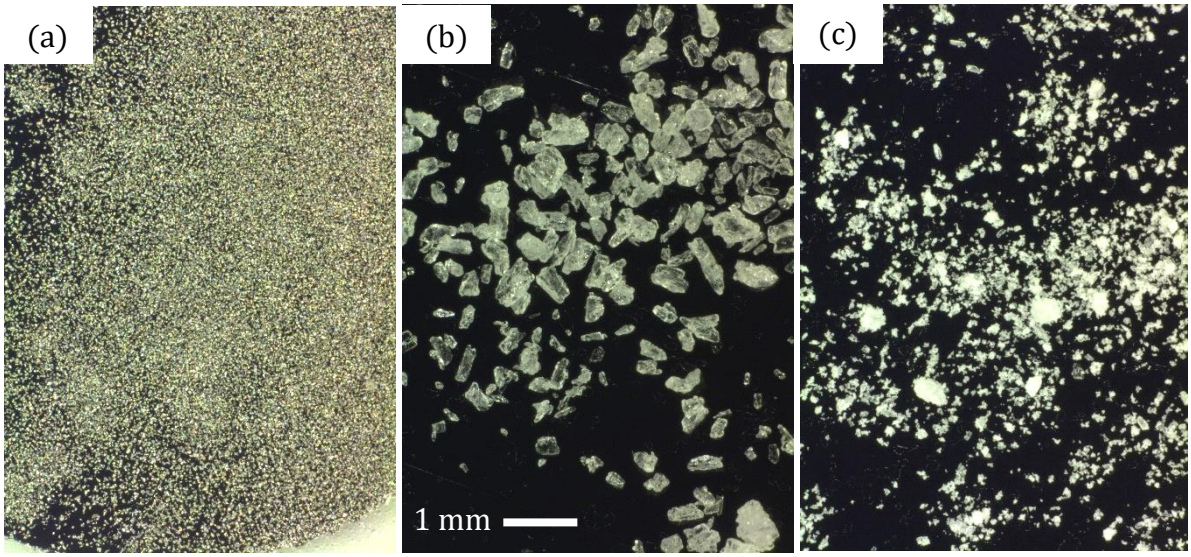

Figure 44. Optical magnifications of magnesium powder (a), urea (b) and grinded urea(c).

Figure 44 shows some magnifications of the magnesium and urea powders and compares their particle size before and after the grinding of urea. The efficiency of grinding is limited by the tendency of urea to form flakes of agglomerated particles.

Then, the spacer is mixed with the magnesium powder in the required ratio. The powders are separately weighted on a balance having a resolution of 0.01 g, obtaining a total mass of 10 g. Then the powders are transferred into an 80 mL jar made in agate, together with 230 agate balls having a diameter of 5 mm. The mixing is carried out at 120 rpm for 10 min.

8.3.2. Sintering

The required amount of powder to be sintered is weighted on a balance having a resolution of 0.01 g, then transferred into the sintering die and manually compressed. The die might be previously treated with dry lubricant to avoid the adhesion of the sintered material. In this case a graphite based lubricant is used on the graphite components, while a boron nitride based lubricant is used where no electrical conduction is needed.

In the case of a cylindrical specimen, the required mass of powder, m, can be calculated by the following formula, where d denotes the diameter of the specimen, h its height and ρ its final density, while w_{urea} denotes the weight fraction of urea, that will be eliminated during the sintering for increasing porosity.

$$m = \frac{\pi \cdot d^2 \cdot h \cdot \rho}{4 \cdot (1 - w_{\mathrm{urea}})}$$

A typical specimen has a diameter of 20 mm, a height of 2 mm and a density of 1.7 g · cm^{-3}. The fraction of urea is between 0 and 30% by weight. Therefore the required mass of powder is between 1 g and 1.5 g.

The die is then positioned inside the process chamber together with the required accessory components used for fitting and centering the die or for reducing the dispersion of heat. Then the press is operated for compressing the die. The pressure of the oleodynamic system, p, is previously set as calculated by the following formula, where d denotes the nominal diameter of the die, D the diameter of the cylinders of the press and σ the required compressive stress.

$$p = \frac{d^2}{D^2} \cdot \sigma$$

The diameter of the cylinders is 115 mm. Since a porous material is desired, the required compressive stress is smaller than 60 MPa. Therefore, for a nominal diameter of 20 mm, the oil pressure will be set below 18 bar. However the oil pressure can not be smaller than 10 bar, therefore stress values smaller than 33 MPa can only be obtained by increasing the nominal diameter.

After the compression, the volume of the powder will decrease by 35% ÷ 45%, regardless of the compressive stress. For an initial height of 6 mm, the dimensional change may be as large as 2.7 mm; this may consume much of the available run of the pistons and the press may became ineffective during the subsequent sintering. In order to regain the full capability of the press, the die has to be released and the fitting components have to be changed.

After compressing the die, one or more thermocouples are positioned to monitor the process. In the most simple solution, a single thermocouple is inserted into one of the graphite

components in order to measure the temperature near the processed powder. If necessary, the wires of the secondary line are connected to the heating filament of the die to provide the external heating.

The chamber is then closed and evacuated until the pressure drops below 2 mbar. A purging with argon above 2 mbar for 5 min is carried out to remove any residual air from the chamber. Then the cooling system is powered and the instruments are commanded to perform the actual sintering process, while the temperature and displacement measurements are carried out to monitor the process.

When the sintering is completed, the die has to cool down to a temperature at which magnesium will not ignite. Then the chamber is vented and opened. All the connections are broken and the compression is released. Finally the sintered specimen is extracted from the die for the subsequent analyses.

8.4. Analytical instruments and methods

8.4.1. Geometrical density

Geometrical measurements of density were performed on cylindrical specimens, by using an analytical balance for measuring their weight and a Vernier caliper for their diameter and height.

The density, ρ, was calculated by the following formula, where m denotes the mass of the specimen, d the diameter and h the height.

$$\rho = \frac{4 \cdot m}{\pi \cdot d^2 \cdot h}$$

The balance has a resolution of 0.1 mg, while the resolution of the caliper is 0.05 mm. The typical specimen has a mass of 1 g, a diameter of 20 mm and a height of 2 mm. Therefore the relative uncertainty is estimated as 2.5% and the height is the dominant term.

$$u_\mathrm{r}^2(\rho) = u_\mathrm{r}^2(m) + 4 \cdot u_\mathrm{r}^2(d) + u_\mathrm{r}^2(h)$$

8.4.2. Archimedes' method

Measurements of density based on the Archimedes' principle were performed by weighting the specimens when dry and when immersed into a standard liquid. The weight was measured by an analytical balance. The standard liquid was lamp oil of the type Axton, having a density of 0.802 g · cm^{-3}.

The specimen density, ρ, was calculated by the following formula, where m_d denotes the weight of the specimen when dry, m_i the weight when immersed and ρ_f the density of the fluid.

$$\rho = \rho_\mathrm{f} \cdot \frac{m_\mathrm{d}}{m_\mathrm{i}}$$

The balance has a resolution of 0.1 mg. The typical specimen has a mass of 1 g and a density of 1.7 g · cm^{-3}, thus its apparent mass when immersed is 0.47 g. The temperature, T, was not controlled, but all measurements were performed between 19 °C and 25 °C and the volumetric thermal coefficient of the liquid, α, equals about 10^{-3} K^{-1}. Therefore the relative uncertainty is estimated as 0.3% and the thermal effect is the dominant term.

$$u_\mathrm{r}^2(\rho) = u_\mathrm{r}^2(\rho_\mathrm{f}) + \alpha^2 \cdot u_\mathrm{a}^2(T) + u_\mathrm{r}^2(m_\mathrm{d}) + u_\mathrm{r}^2(m_\mathrm{i})$$

8.4.3. Gas pycnometry

Measurements of density based on the Boyle's law of gas expansion were performed by a model Ultrapyc 1200e instrument provided by Quantachrome GmbH & Co. KG. This is a gas pycnometer fed with high purity helium, which penetrates into crevices as little as 0.2 nm in diameter. It is equipped with the three specimen cells described in Table 25. Repeatability and uncertainty are given for a specimen cell filled with material and are relative to the measure.

cell	volume	repeatability	uncertainty
	cm^3	%	%
small	10.8	0.015	0.03
medium	48.1	0.010	0.02
large	131.7	0.010	0.02

Table 25. Properties of the cells of the pycnometer.

In most cases the specimen did not fill the cell, but the smaller cell was used compatibly with the size of the specimen. All the measurements were carried out between 19 °C and 25 °C, with three repetitions, and the standard deviation was smaller than 0.7% of the average in terms of density.

8.4.4. Uncertainty in the calculation of porosity

The calculation of the porosity of a nearly bulk material, when determined by measuring extensive quantities, as mass and volume, is necessarily affected by a large uncertainty, that may even compromise the significativity of the result. In the case of a material having a known bulk density, ρ_0, the total porosity, p, can be calculated by the following formula, where ρ denotes the apparent density.

$$p = 1 - \frac{\rho}{\rho_0}$$

As described below, if the apparent density is measured with an uncertainty of 2.5% and the bulk density is known with an uncertainty smaller than 1%, the calculation of the total porosity is impossible for porosity values smaller then 5%, because the absolute uncertainty becomes larger then the nominal value.

$$u_{\mathrm{a}}(p) = 2 \cdot \frac{1-p}{1-{u_{\mathrm{r}}}^2(\rho_0)} \cdot \sqrt{{u_{\mathrm{r}}}^2(\rho_0) + {u_{\mathrm{r}}}^2(\rho)}$$

The open porosity, p_{o}, of a specimen having a regular shape can be calculated by the following formula, where V_{g} denotes the geometrical volume and V_{i} the volume inaccessible to a penetrating fluid.

$$p_{\mathrm{o}} = 1 - \frac{V_{\mathrm{i}}}{V_{\mathrm{g}}}$$

Again, if the geometrical volume is measured with an uncertainty of 2.5% and the inaccessible volume with an uncertainty smaller than 1%, the calculation of the open porosity is impossible for porosity values smaller then 5%.

$$u_{\mathrm{a}}(p_{\mathrm{o}}) = 2 \cdot \frac{1-p_{\mathrm{o}}}{1-{u_{\mathrm{r}}}^2(V_{\mathrm{g}})} \cdot \sqrt{{u_{\mathrm{r}}}^2(V_{\mathrm{g}}) + {u_{\mathrm{r}}}^2(V_{\mathrm{i}})}$$

8.4.5. Scanning Electron Microscopy

The micromorphology of the sintered magnesium specimens was analysed by a model SUPRA 40 scanning electron microscope provided by Carl Zeiss AG. The instrument is a field emission gun scanning electron microscope (FEG-SEM), being equipped with a Schottky emitter as the electron gun; this is made by a tungsten tip with a zirconium oxide reservoir and emits a highly collimated, low energy electron beam.

The instrument has Gemini type optics that operate at beam voltages between 0.02 kV and 30 kV. It is also equipped with one backscattered electron (BSE) detector and two secondary electron (SE) detectors. One of the SE detectors has an in-lens construction that enhances its detection efficiency at low beam voltages, thus improving resolution to 1 nm.

The sintered specimens were broken by producing a fracture along their axis of symmetry and the micromorphology of the fracture surface was analysed by FEG-SEM. The analysis was performed by the in-lens detector, with magnifications between 200× and 10^5×. At a magnification of 2500× an area of 143 × 100 μm can be covered by one scan. The beam voltage was set between 5 kV and 15 kV, the aperture was 30 μm and the working distance was between 2 mm and 9 mm.

8.4.6. Electrochemical analyses

The sintered magnesium specimens were analysed by anodic polarization and by electrochemical impedance spectroscopy (EIS) in order to asses the corrosive behaviour in simulated physiological environment. All the measurements were performed in 500 mL of aerated Ringer solution, that has the composition reported in Table 26.

NaCl	9.00	$g \cdot L^{-1}$
KCl	0.43	$g \cdot L^{-1}$
$CaCl_2$	0.24	$g \cdot L^{-1}$
$NaHCO_3$	0.20	$g \cdot L^{-1}$

Table 26. Composition of the Ringer solution.

The solution was prepared by weighting the salts with an uncertainty smaller than 0.1% and by dissolving them in 1 L of demineralized water. The water was measured in two portions by a cylinder having a capacity of 500 mL and resolution of 1 mL, therefore the volume uncertainty is estimated as 0.3% and this is the dominant term.

The electrochemical measurements were performed at room temperature, by means of the three electrodes cell shown in Figure 45. The counter electrode was made of AISI 314 stainless steel. The reference electrode was a type Ag/AgCl, KCl (3 M) electrode, with a potential of +0.210 V vs. NHE.

The working electrode was made of a copper wire irreversibly connected to the back side of the specimen. The wire had a PVC sheath and was soldered to the specimen or stuck to it by means of a conductive glue. This was a type MS60805T silver glue provided by Media System Lab S.r.l. Then the whole was cold mounted with a bi-component resin; this was an acrylic resin of the type Mecaprex KM-U provided by Presi S.A. Finally the front side of the specimen was grinded with an abrasive paper of the type P4000 provided by Labormet Due S.r.l.

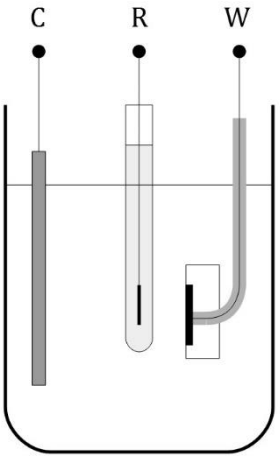

Figure 45. Electrochemical cell: counter (C), reference (R) and working (W) electrodes.

The anodic polarization was performed by a generator connected between the working and counter electrodes. This was a model 6622A instrument provided by HP Inc. It can produce currents between 0 and 4 A with a maximum voltage of 20 V. The potentials of the working and counter electrodes were measured by a model 34970A data acquisition unit provided by HP Inc. This instrument also measured the current by means of a 1 Ω shunt resistor. The polarization was carried out from the free corrosion potential, covering an interval of 0.3 V in 6 ÷ 12 min. The measurement was carried out after 1 h, 24 h, 48 h, 72 h and 144 h of permanence in solution, compatibly with the resistance of the specimen, with no electrolyte renewal.

The EIS measurements were performed by a CompactStat.h impedance analyser provided by Ivium Technologies B.V. An alternate voltage of 10 mV_{rms} was applied, with frequencies ranging between 10^{-2} Hz and 10^{5} Hz and the measurements were carried out at five frequencies per decade. The permanence in solution was longer than 24 h, depending on the resistance of the specimen, to a limit of eighteen days. The measurement was carried out three times per day in the first four days and less frequently later, with no electrolyte renewal.

9. Results and discussion

9.1. Sintering process

Several magnesium specimens were sintered by changing the composition of the powder and the sintering parameters. When urea was used as the spacer, the powder mixtures were prepared with a fraction of urea between 5% and 30% by weight. The sintering experiments failed with a 40% of urea in the powder.

Cylindrical specimens having a diameter of 20 mm were produced by sintering a mass of powder between 1 g and 1.5 g. An increased diameter, equal to 32 mm, was also used for reducing the compressive stress. This was constant during the sintering process and was set between 10 MPa and 57 MPa. The process was carried out by heating the die between 400 °C and 622 °C for 10 ÷ 20 min. Although the actual sintering occurs only above 600 °C, a pre-treatment at lower temperatures was optionally performed in order to control the micro-morphology of the sintered material.

Figure 46 shows a typical sintering process, performed on 1 g of magnesium powder with no spacer, in a graphite die with a nominal diameter of 20 mm. The powder was compressed at 40 MPa, thereby getting axially compressed from 4.3 mm to 2.7 mm in height. Then the chamber was evacuated to a pressure of 1 mbar and purged with argon above 2 mbar for 5 min. After that, the main generator (20 V_{rms} / 2000 A_{rms}) was used to carry out a pre-heating below 200 °C with the minimum generated current of 200 A_{rms}.

The actual sintering was finally performed by increasing the power up to a maximum of 1650 W, maintaining the temperature at 600 ÷ 605 °C for 10 min. Between 400 °C and 500 °C the pressure raised above 1.5 mbar due to the degassing of the die. As observed by the measurement of displacement, within the first 300 °C of heating the powder got further compressed by 0.4 mm. Later the dimensional change due to thermal expansion predominantly influenced the measured displacement. The height of the obtained specimen was equal to 2.0 mm.

9.2. Density measurements

The porosity of the sintered specimens was calculated by measuring the geometrical density. By changing the fraction of spacer and the sintering parameters, it is possible to synthesize nearly bulk magnesium as well as porous magnesium with porosities up to 37%.

In Table 27 the obtained porosity of nine specimens is correlated to the synthesis parameters. The results show that the pre-treatment at high temperature permits to maintain a larger porosity after the subsequent sintering, while nearly dense magnesium is produced by processing the powder without any pre-treatment.

pre-treatment	sintering	$w_{\text{urea}} = 20\%$ $\sigma = 32$ MPa	$w_{\text{urea}} = 20\%$ $\sigma = 10$ MPa	$w_{\text{urea}} = 30\%$ $\sigma = 10$ MPa
absent	600 °C, 10 min	$< 8\%$	$(13 \pm 3)\%$	$(21 \pm 3)\%$
450 °C, 10 min		$< 9\%$	$(17 \pm 3)\%$	$(28 \pm 3)\%$
550 °C, 10 min		$(8 \pm 4)\%$	$(31 \pm 3)\%$	$(37 \pm 2)\%$

Table 27. Porosity of magnesium synthesized with several procedures.

The density measured by Archimedes' method on magnesium specimens sintered to nearly full density is consistent to the density returned by gas pycnometry. In the case of porous magnesium instead the former is smaller because the penetrating liquid does not fill all the pores that are accessible to helium. The difference can be as large as 13% respect to the density returned by the pycnometer, for specimens with a total porosity approaching 30%. No close porosity was found by gas pycnometry in any specimen.

9.3. Scanning Electron Microscopy

Some representative FEG-SEM magnifications of the fracture micromorphology of the sintered magnesium are shown in Figure 47. They were made with a beam voltage of 10 kV, an aperture of 30 μm and a magnification of 2500× (a, c, e) or 5000× (b, d, f). All these specimens were sintered at 600 °C for 10 min, without any pre-treatment.

The 21% porous specimen (a, b) was produced by sintering the magnesium powder with a 30% by weight of urea. The compressive stress was as low as 10 MPa.

The 4% porous specimen (c, d) was produced by sintering the magnesium powder containing only a 20% by weight of urea. The compressive stress was 32 MPa in this case. Although the given porosity is uncertain, the magnifications visually corroborate the calculated value.

The dense specimen (e, f) was produced by sintering the magnesium powder with no spacer, under a compressive stress as large as 38 MPa. This caused the powder particles to collapse completely, thereby creating a continuous material.

9.4. Anodic polarization

Three sintered magnesium specimens with porosities between 5% and 29% were analysed by anodic polarization and compared to the behaviour of bulk magnesium. Figure 48 shows the results of the first two measurements, performed after 1 h (a) and 24 h (b) of immersion in Ringer solution.

All the sintered specimens were produced from a powder mixture containing a 20% by weight of urea and were sintered at 600 °C for 10 min, with a compressive stress ranging between 10 MPa and 32 MPa. Their volume was between 0.75 cm^3 and 1 cm^3, while the bulk magnesium specimen had a volume of 1.25 cm^3.

All the specimens had a free corrosion potential between –1.6 V and –1.5 V vs. Ag/AgCl after 1 h of immersion. For every specimen the current measured over an interval of 0.3 V ranged from about 10^{-6} A · cm^{-2} to $5 \cdot 10^{-4}$ A · cm^{-2}. Current showed a sudden increase when reaching $5 \cdot 10^{-5}$ A · cm^{-2} in the less porous sintered specimens, but this phenomenon essentially disappeared within two days.

After 24 h the free corrosion potential of bulk magnesium increased to –1.1 V and the specimen got completely corroded before the measurement programmed at 48 h. During the first free days also the 29% porous magnesium specimen increased its free corrosion potential, although by less then 0.1 V per day; then the specimen got completely corroded before the final programmed measurement at 144 h.

The 5% porous and the 17% porous magnesium specimens showed a marked tendency to resist to corrosion for several days, although the 5% porous magnesium specimen was the only one to resist until the sixth day. Therefore all the sintered specimens are much more resistant to corrosion then bulk magnesium, but a larger porosity will increase the corrosion rate.

9.5. Electrochemical Impedance Spectroscopy

Two sintered magnesium specimens, having a porosity of 4% and 21%, were analysed by EIS and compared to the behaviour of bulk magnesium. Figure 50, Figure 52 and Figure 54 show the Bode plots of the three specimens for several immersion times, depending on their corrosion resistance. Figure 49, Figure 51 and Figure 53 show their morphology after their permanence in Ringer solution. Figure 55 compares their impedance at 0.1 Hz as a function of immersion time.

Both the sintered specimens were sintered at 600 °C for 10 min, but the 4% porous specimen was produced from a powder mixture containing only a 20% by weight of urea, with a compressive stress of 32 MPa, while the 21% porous specimen was produced from a powder mixture with a 30% of urea and a compressive stress of just 10 MPa. Their volume was between 0.75 cm^3 and 1 cm^3, while the bulk magnesium specimen had a volume of 1.25 cm^3.

After 1 h of immersion all the specimens showed the typical behaviour of a metal in contact with an electrolyte, with a maximum phase at about 100 Hz. The bulk magnesium specimen initially had the highest impedance at low frequency, but it got corroded during the first 24 h of immersion.

The sintered specimens instead had a lower impedance, but a pseudo-passivating layer of corrosion products, which is white in the pictures, preserved them from extensive corrosion for at least six days. The 21% porous magnesium specimen steadily increased its impedance at low frequency by two orders of magnitude in eighteen days.

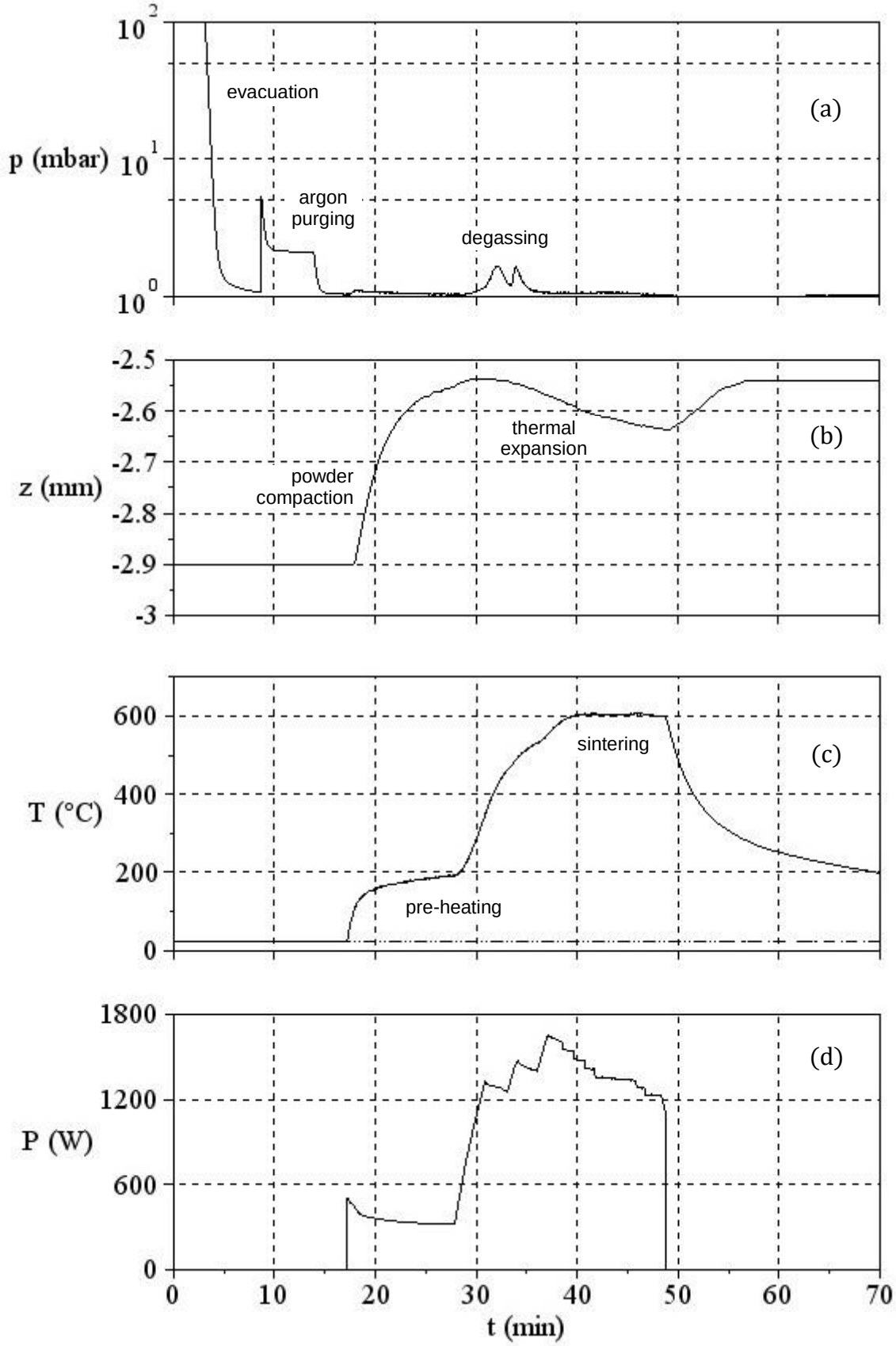

Figure 46. Sintering process: pressure (a), displacement (b), temperature (c) and power (d).

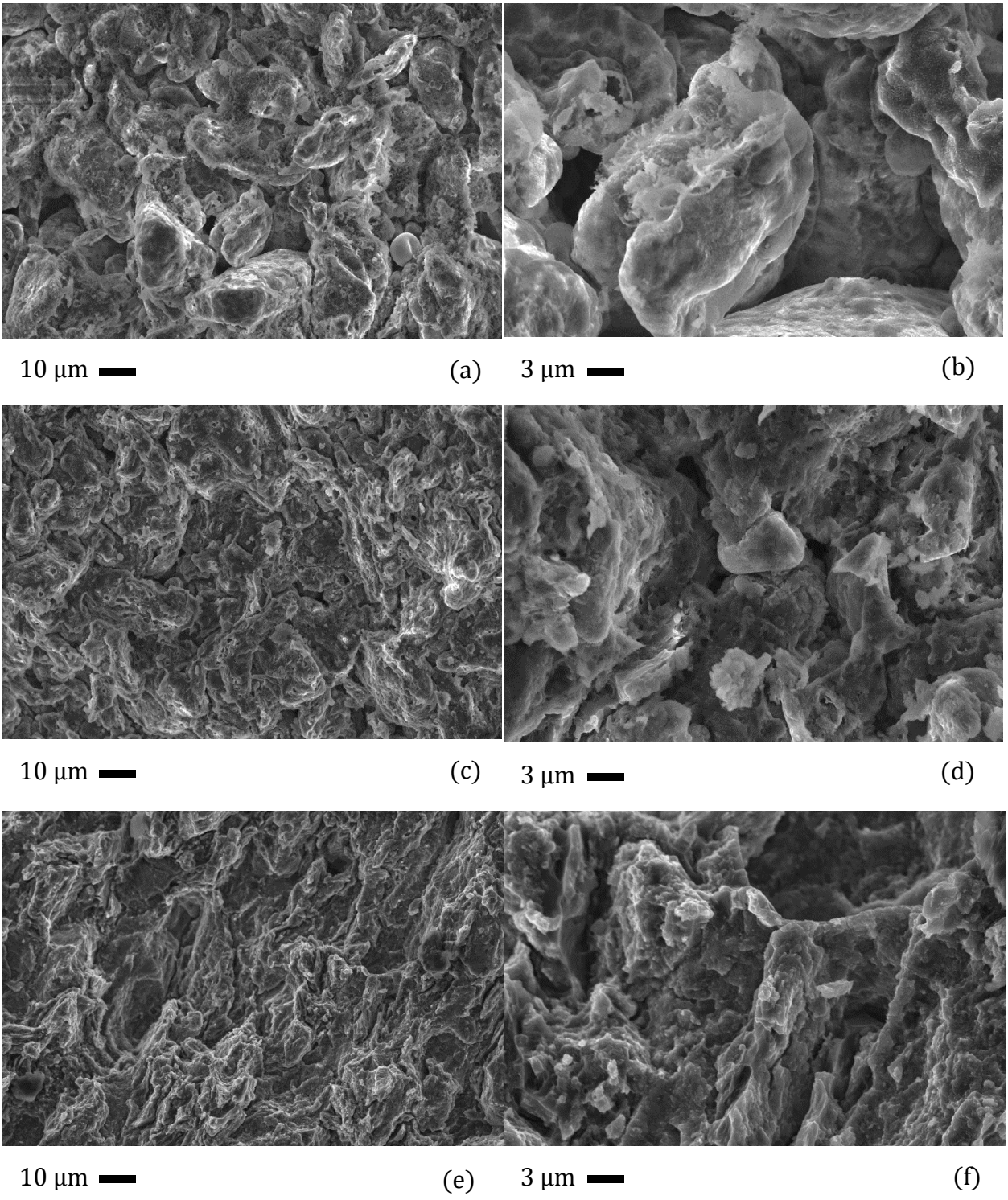

Figure 47. FEG-SEM magnifications of 21% porous (a, b), 4% porous (c, d) and dense (e, f) magnesium specimens.

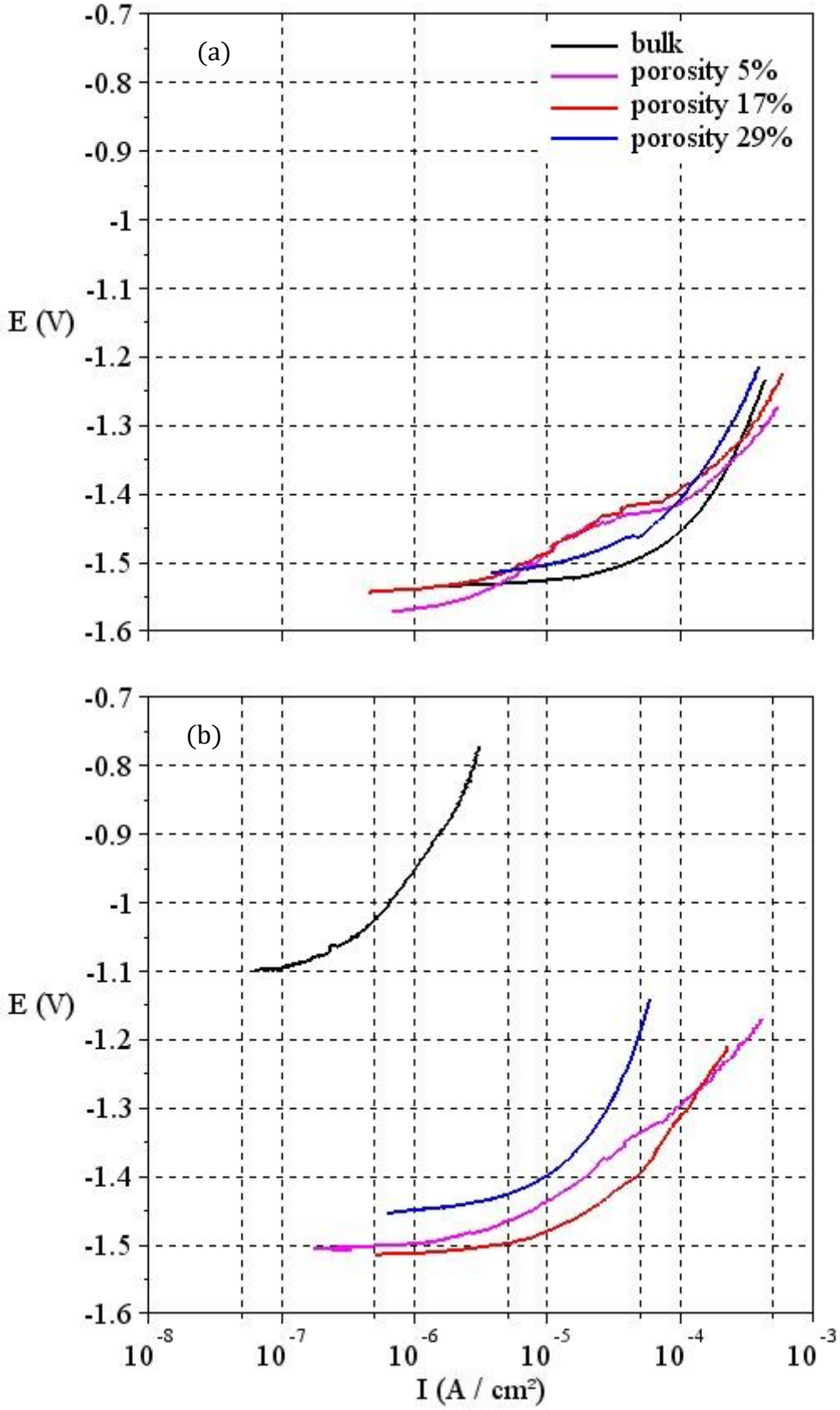

Figure 48. Results of the anodic polarization after 1 h (a) and 24 h (b).

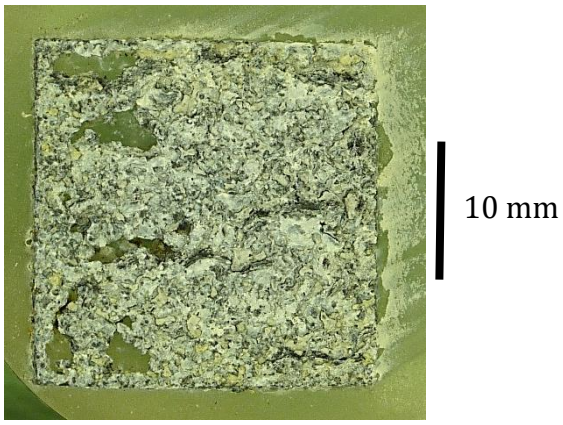

Figure 49. Morphology of bulk magnesium after 24 h in Ringer solution.

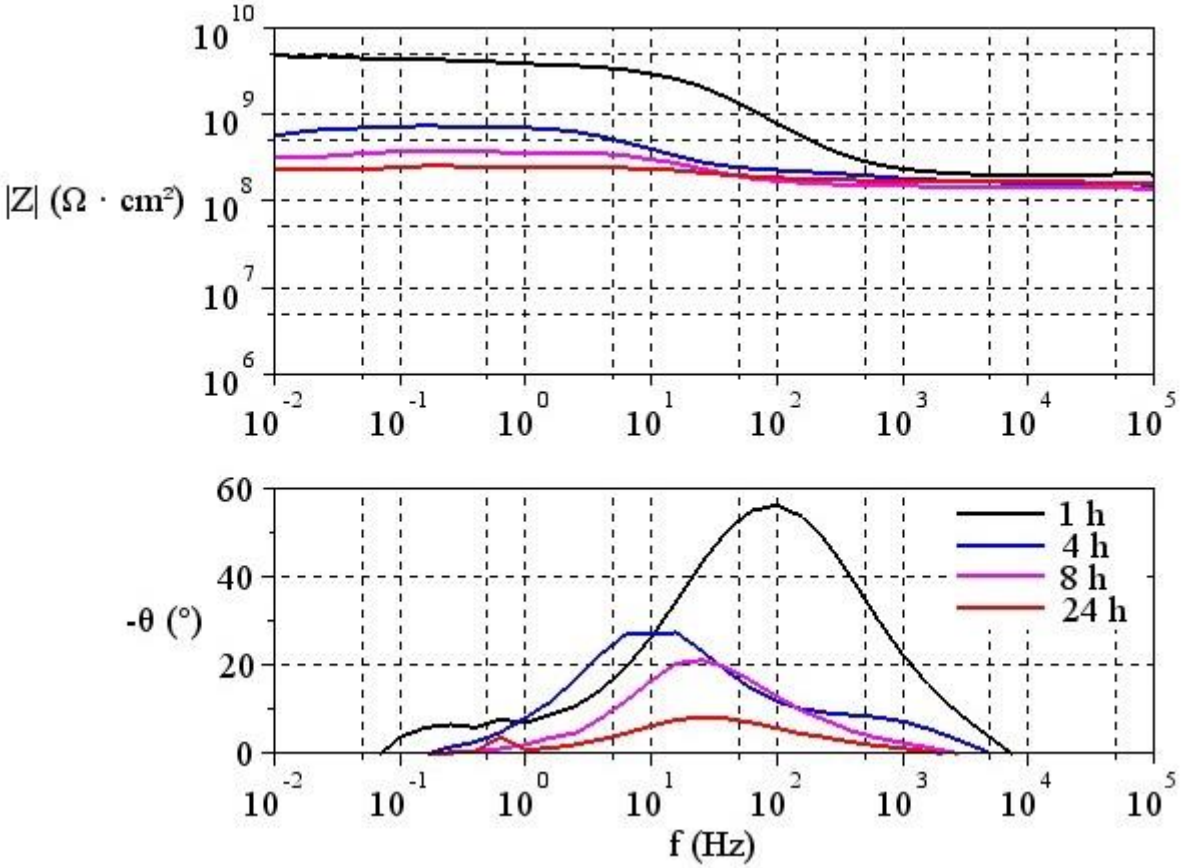

Figure 50. Results of EIS on bulk magnesium.

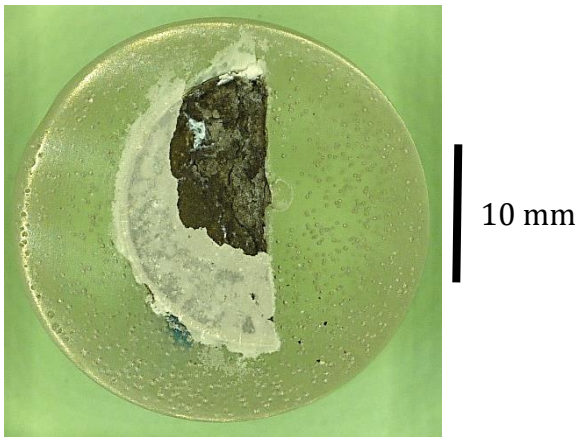

Figure 51. Morphology of 4% porous magnesium after six days in Ringer solution.

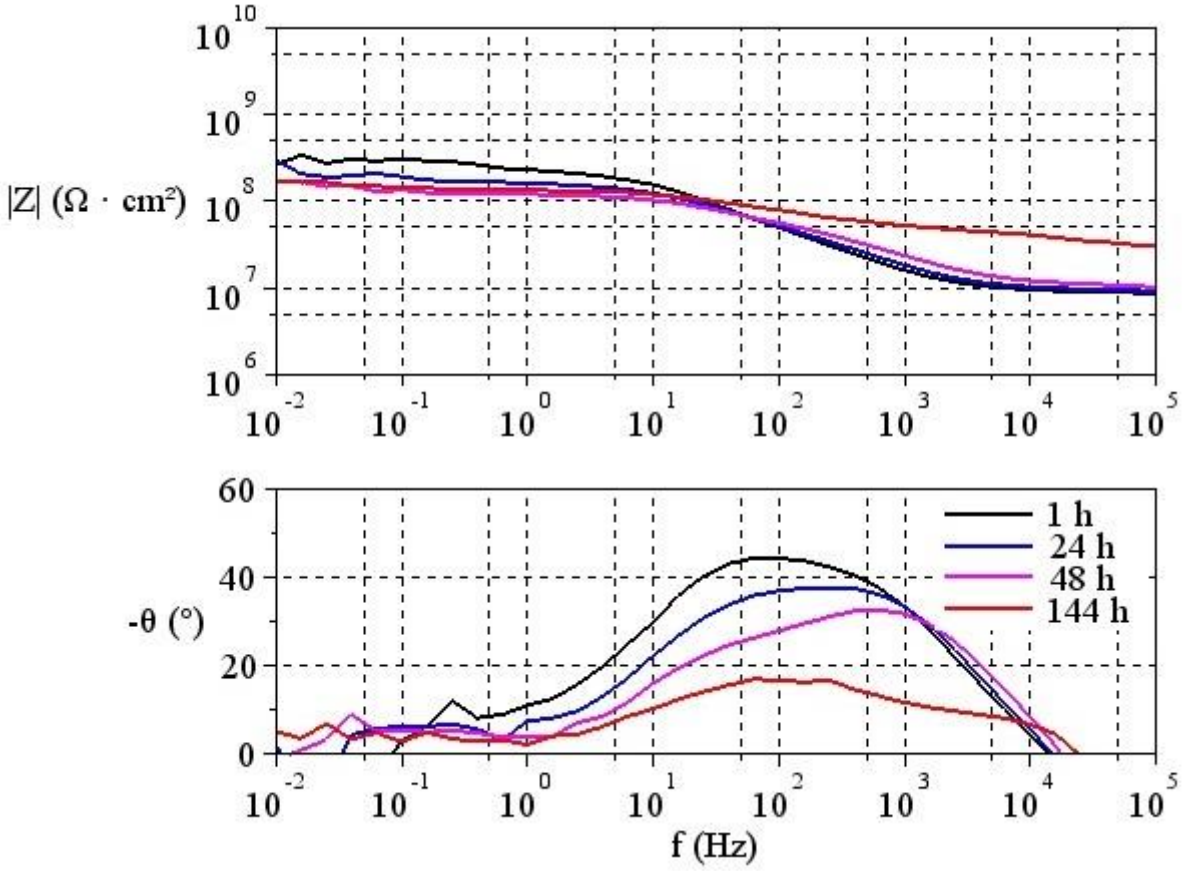

Figure 52. Results of EIS on 4% porous magnesium.

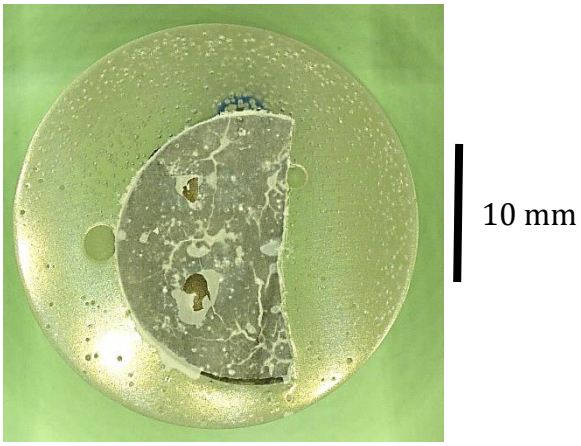

Figure 53. Morphology of 21% porous magnesium after eighteen days in Ringer solution.

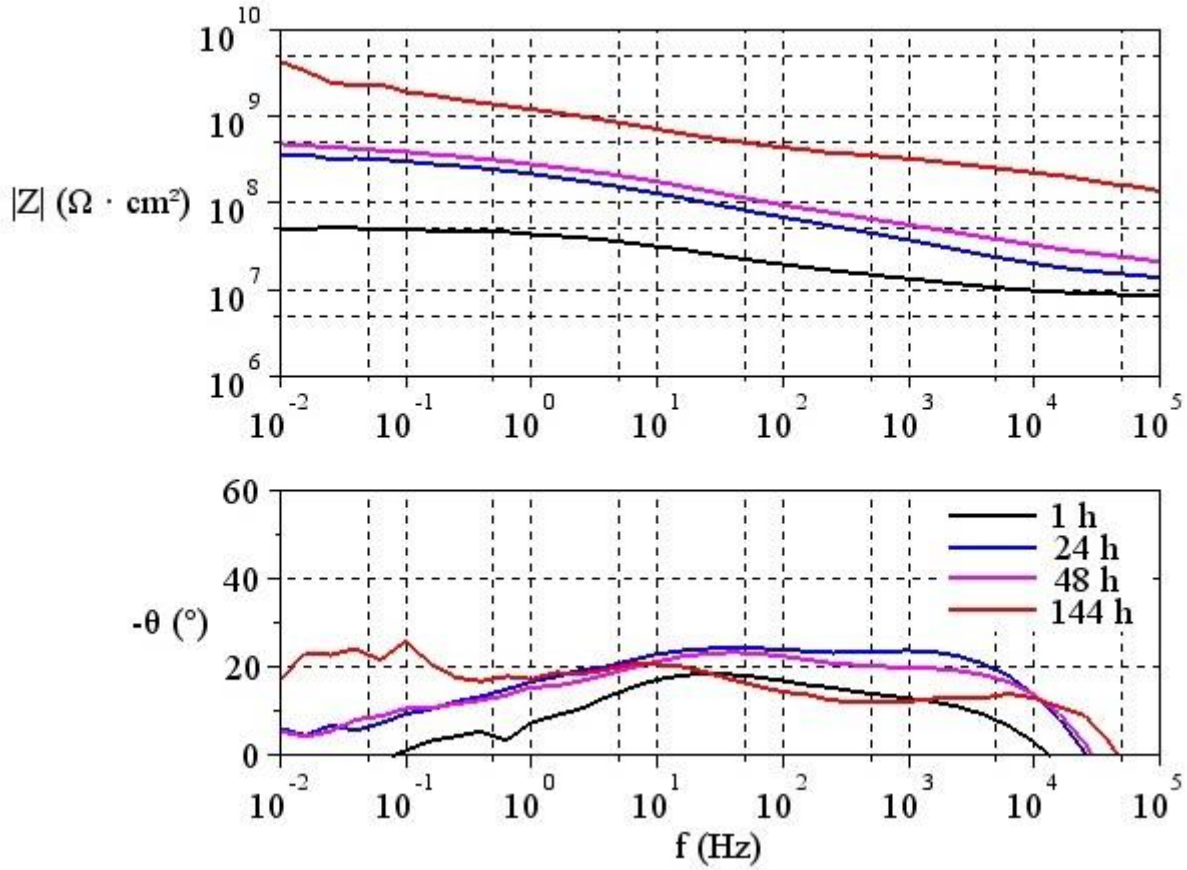

Figure 54. Results of EIS on 21% porous magnesium.

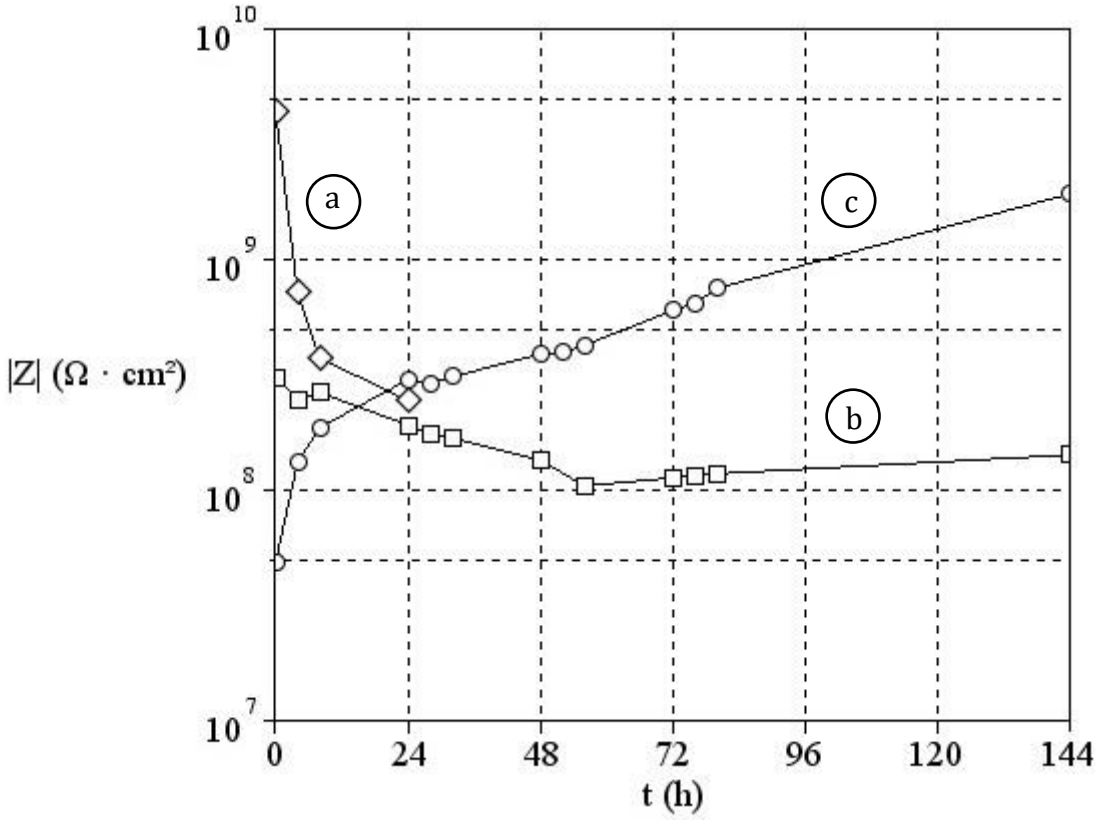

Figure 55. Impedance of bulk (a), 4% porous (b) and 21% porous (c) magnesium at 0.1 Hz.

10. Conclusion

A novel configuration of the SPS sintering process was designed to permit the synthesis of porous magnesium with a controlled micromorphology and with predictable macroscopic properties. This will lead to the production of bioabsorbable osteoimplants with properties that are optimized for specific implantation sites.

This solution required a comprehensive study of the temperature distribution within the system, in order to overcome some restraints that necessarily hindered the direct measurement of temperature. Therefore a thermal model of the sintering die was developed by the finite element analysis and was validated by means of an experimental apparatus. Measurements of thermal conductivity were previously performed on the major components of the system in order to set the model parameters.

The sintering apparatus was improved by adding and calibrating a displacement sensor and by completing the monitoring and control system. It was then used to actually produce porous magnesium specimens with varying porosity, that were characterized in order to investigate their micromorphology and to assess their corrosion behaviour in simulated body fluid.

Publications

M. Parvis, F. Ferraris, S. Grassini, E. Angelini, D. Fulginiti, *Biodegradable metallic materials: a measuring approach to predict the corrosion rate*, IEEE Instrumentation and Measurement Technology Conference (I2MTC), Minneapolis, USA, May 6-9, 2013, 228-233

S. Grassini, E. Angelini, D. Fulginiti, F. Ferraris, M. Parvis, Misure per lo Sviluppo e la Caratterizzazione di Bioimpianti Riassorbibili, XXX Congresso Nazionale del Gruppo di Misure Elettriche ed Elettroniche, Trento, Italy, September 8-11, 2013

E. Angelini, B. De Benedetti, D. Fulginiti, S. Grassini, F. Ferraris, M. Parvis, *Development and characterization of porous magnesium biosorbable implants*, IEEE International Symposium on Medical Measurements and Applications (MeMeA), Torino, Italy, May 7-9, 2015

D. Fulginiti, S. Grassini, E. Angelini, M. Parvis, *Indirect material density measurement by a simple digital imaging method*, accepted proceeding, IEEE Instrumentation and Measurement Technology Conference (I2MTC), Taipei, Taiwan, May 23-26, 2016

References

Adamson, 1976 — K. G. Adamson, *Corrosion*, Newnes-Butterworths, London (United Kingdom), 1976

Albright, 1988 — D. L. Albright, *Advances in Magnesium Alloys and Composites*, International Magnesium Association and Non-Ferrous Metals Committee, Phoenix (Arizona), 1988, 57-75

Bartak, 1991 — D. E. Bartak, T. D. Schleisman, E. R. Woolsey, Proceedings of 48th World Magnesium Conference, International Magnesium Association, 1991, 55-60

Benmalek, 1990 — M. Benmalek, P. Gimenez, G. Regazzoni, Proceedings of 47th World Magnesium Conference, International Magnesium Association, 1990, 117-123

Brun, 1976 — C. H. Brun, J. Pagetti, J. Talbot, Mémoires Scientifiques de la Revue de Métallurgie 73 (1976) 659-668

Emley, 1966 — E. F. Emley, *Principles of magnesium technology*, Pergamon Press, New York, 1966, ch. 20

Freni, 2014 — P. Freni, P. Tecchio, S. Rollino, B. De Benedetti, *Porosity characterization of biomedical magnesium foams produced by Spark Plasma Sintering*, IEEE International Symposium on Medical Measurements and Applications (MeMeA), Lisboa, Portugal, June 11-12, 2014

Froats, 1987 — A. Froats, T. K. Aune, D. Hawke, W. Unsworth, J. Hillis, *Metals Handbook*, 9th edition, ASM International, Materials Park (Ohio), 1987, 740-754

Grassini, 2014 — S, Grassini, E. Angelini, M. Parvis, S. Corbellini, M. Ishtaiwi, *Electrochemical characterization of magnesium bioabsorbable implants*, proc. of IEEE International Symposium on Medical Measurements and Applications (MeMeA), Lisboa, Portugal, June 11-12, 2014

Hagans, 1987 — P. L. Hagans, *Science and technology of rapidly quenched alloys*, Proceedings of Materials Research Society Symposium 80 (1987) 113-120

Hanawalt, 1942 — J. D. Hanawalt, C. E. Nelson, J. A. Peloubet, Transactions of AIME 147 (1942) 273-299

Kita, 2015 — J. Kita, A. Engelbrecht, F. Schubert, A. Gross, F. Rettig, R. Moos, *Some practical points to consider with respect to thermal conductivity and electrical resistivity of ceramic substrates for high-temperature gas sensors*, Sensors and Actuators B 213 (2015) 541-546

Hofmann, 1995 — G. O. Hofmann, *Biodegradable implants in traumatology: a review on the state-of-the art*, Archives of Orthopaedic and Trauma Surgery, 143 (1995) 123-132

Loose, 1946 — W. S. Loose, *Corrosion and protection of magnesium*, ASM International, Materials Park (Ohio), 1946, 173-260

Makar, 1993 — G. K. Makar, J. Kruger, *Corrosion of magnesium*, International Materials Reviews 38 (1993) 138-153

Makar, 1998 G. L. Makar, J. Kruger, A. Joshi, *Advances in magnesium alloys and composites*, International Magnesium Association and Non-Ferrous Metals Committee, Phoenix (Arizona), 1998, 105-121

Muller, 2006 L. Muller, F. A. Muller, *Preparation of SBF with different HCO_3^- content and its influence on the composition of biomimetic apatites*, Acta Biomaterialia 2 (2006) 181-189

Nicodemi, 2008 W. Nicodemi, *Acciai e leghe non ferrose*, Zanichelli, Bologna (Italy), 2008

Parchovianský, 2014 M. Parchovianský, D. Galusek, P. Švančárek, J. Sedláček, P. Šajgalík, *Thermal behavior, electrical conductivity and microstructure of hot-pressed Al_2O_3/SiC nanocomposites*, Ceramics International 40 (2014) 14421-14429

Perrault, 1974 G. G. Perrault, *The potential-pH diagram of the magnesium-water system*, Journal of Electroanalytical Chemistry and Interfacial Electrochemistry 51 (1974) 107-119

Polmear, 1992 I. J. Polmear, *Physical metallurgy of magnesium alloys*, DGM Informationsgesellschaft, Oberursel (Germany), 1992, 201

Przyluski, 1970 J. Przyluski, E. Palka, *Untersuchung der Kinetik der anodischen oxydation des magnesiums in einer ammoniumchloridlösung*, Electrochimica Acta 15 (1970) 853-864

Purbaix, 1974 M. Purbaix, *Atlas of electrochemical equilibria in acqueous solutions*, National Association of Corrosion Engineers, Houston (Texas), 1974, 141

Reichek, 1985 K. N. Reichek, K. J. Clark, J. E. Hillis, *Controlling the salt water corrosion performance of magnesium AZ91 alloy*, International Congress and Exposition, Society of Automotive Engineers, Detroit, 1985, n. 850417

Song, 1999 G. L. Song, A. Atrens, *Corrosion mechanisms of magnesium alloys*, Advanced Engineering Materials 1 (1999) 11-33

Song, 2007 G. Song, *Control of biodegradation of biocompatable magnesium alloys*, Corrosion Science 49 (2007) 1696-1701

Tawil, 1987 D. S. Tawil, Proceedings of Conference on Magnesium Technologies, Intitute of Metals, 1987, 66-74

Tunold, 1977 R. Tunold, H. Holtan, M. H. Berfe, A. Lasson, R. Steen-Hansen, *The corrosion of magnesium in aqueous solution containing chloride ions*, Corrosion Science 17 (1977) 353

Vozár, 1996 L. Vozár, *A computer-controlled apparatus for thermal conductivity measurement by the transient hot wire method*, Journal of Thermal Analysis 46 (1996) 495-505

Walter, 1986 G. W. Walter, *A review of impedance plot methods used for corrosion performance analysis of painted metals*, Corrosion Science 26 (1986) 681-703

Wen, 2001 C. E. Wen, M. Mabuchi, Y. Yamada, K. Shomojima, Y. Chino, T. Asahina, *Processing of biocompatible porous Ti and Mg*, Scripta Materialia 45 (2001) 1147-1153

Witte, 2015 F. Witte, *The history of biodegradable magnesium implants: A review*, Acta Biomaterialia 23 (2015) S28-S40

Xin, 2011 Y. Xin, T. Hub, P. K. Chu, *In vitro studies of biomedical magnesium alloys in a simulated physiological environment: A review*, Acta Biomaterialia 7 (2011) 1452-1459

Zreiqat, 2002 H. Zreiqat, C. R. Howlett, A. Zannettino, P. Evans, G. Schulze-Tanzil, C. Knabe, M. Shakibae, *Mechanisms of magnesium-stimulated adhesion of osteoblastic cells to commonly used orthopaedic implants*, Journal of Biomedical Materials Research 62 (2002) 175-184